The Dynamical Evolution of Young Stellar Regions

Daniel W. Griffiths

Department of Physics & Astronomy
The University of Sheffield

A dissertation submitted in candidature for the degree of Doctor of Philosophy at the University of Sheffield

September, 2018

Declaration

I declare that no part of this thesis has been accepted, or is currently being submitted, for any degree or diploma or certificate or any other qualification in this University or elsewhere. This thesis is the result of my own work unless otherwise stated.

Chapter 4 has been based on Griffiths et al. (2018).

Acknowledgements

I would like to thank my supervisor Simon Goodwin for his fantastic advice, support and encouragement over the past four years. I am deeply grateful for the tremendous amount of work and dedication he has shown to support me. His guidance and experience have been invaluable and I could not have asked for better supervision.

I would also like to thank Richard Parker for his help in getting me started with N-body simulations, and Paul Kerry for his invaluable computing support.

A big thank you goes to all past and present members of the University of Sheffield astronomy group for making these past four years an unforgettable experience. They say that you are the average of the people you surround yourself with. In that case, I consider myself lucky to be surrounded by such intelligent, supportive and entertaining co-workers.

A special thanks to my family, especially my mother for always being there for me.

Finally and most importantly, thank you to my wonderful fianceé Jennifer for always believing in me, for supporting me through all the ups and downs, the working weekends and the sleepless nights, and for making me want to be the best person I can be. I could not have done this without you and I cannot wait for us to begin our new chapter together.

Summary

Young stars are generally found in groups we call 'young stellar regions, which dynamically evolve. This thesis aims to provide insight on how these regions evolve, by focusing primarily on the dynamical formation and destruction of binary systems and the effect of stellar relaxation.

Observations of massive stars in Cyg OB2 show that they can reside in binary systems with separations of a few thousand AU, which we call massive wide binaries (MWBs). We perform N-body simulations to show that, due to the dynamical formation and destruction of binaries in dense regions, a bound cluster will typically produce an average of one MWB. Therefore, any region that contains many massive wide binaries (such as Cyg OB2) must have been composed of many individual subregions.

Observations of G-dwarfs in the Galactic field show that $\sim 5\%$ reside in binary systems with separations greater than 10000 AU, which we call very wide binaries (VWBs). One possible way of forming VWBs is via the 'soft capture mechanism during the dissolution of a stellar association. We perform N-body simulations to show that it is not likely that this mechanism accounts for the observed field VWB population on its own.

Gas expulsion is a common explanation for the destruction of young stellar regions, but gas expulsion depends on the regions effective star formation efficiency. We perform hybrid N-body/SPH simulations to show that relaxation between stars in a dense cluster causes dynamical gas depletion in the clusters core, decreasing the possibility that gas expulsion will unbind the cluster.

Contents

List of Figures

List of Tables

Chapter 1

Introduction

How stars form is one of the most fundamental questions in modern astrophysics. Stars are the fundamental building blocks of galaxies and determine their structure and evolution. Most of the light we observe through our telescopes originated in the core of a star, and stars are responsible for the synthesis of heavy elements, which drives the chemical evolution of galaxies. Planets also form around stars, implying that the formation and evolution of planets is inextricably linked to the formation and evolution of stars.

The regions in which we find young stars are incredibly varied. Some young stellar regions are dense clusters where dramatic, violent interactions between stars may occur, while other regions are relatively diffuse and quiescent and strong interactions between stars are rare. The physical properties of these regions also change over time. This dynamical evolution is complex, stochastic and impossible to observe in real time. By combining observations of the properties of young stellar regions with numerical techniques, we can model their dynamical evolution, make predictions and find observable diagnostics to help us better understand the potential evolutionary paths which young stellar regions may take.

While Chapters 2 and 3 focus on numerical methods, Chapters 4, 5 and 6 of this thesis will show how these numerical methods enable us to make predictions about how star forming regions evolve, how the presence of binary systems can be used as a diagnostic to track dynamical evolution, and how the presence of gas can have a dramatic effect on that evolution.

This chapter, split into three sections, provides the context in which Chapters 2 to 7 are to be understood. Section 1.1 outlines the different categories of young stars, their observational characteristics and the physics which determine their formation and early evolution. Section 1.2 introduces the formation of binary and multiple systems as one of

the main modes of star formation, and the mechanisms by which binaries and multiples are dynamically processed. Finally, section 1.3 introduces the different types of young stellar regions, their properties and the different ways they can dynamically evolve.

1.1 Young Stars

When we look at the Milky Way, we can observe stars in the process of forming. Observations by Herschel (Motte et al., 2010), Spitzer (Evans et al., 2009), ALMA (Murillo et al., 2013) and the Hubble Space Telescope (Burrows et al., 1996) all identify young, star-like objects from their infrared emission which are understood to be in one of the various stages of star formation.

A 'Young Stellar Object' (YSO) is the terminology for several overlapping categories of young, star-like objects. When these categories are combined, they correspond to a series of stages, which track the evolution of the YSO from the collapse of a pre-stellar core, to the start of hydrogen burning in the star's core and the beginning of its life on the Main Sequence. To better explain these evolutionary stages, it is useful to track a star's formation from the beginning. In this section, I first describe molecular clouds as being the environment from which stars form. The densest part of the molecular cloud, the 'pre-stellar core', is then introduced as the fundamental unit of star formation. The observational classes of young stellar object are then outlined, before the physical processes underlying low-mass star formation are explained. Finally, the specific challenges of studying the formation of high-mass stars are described.

1.1.1 Molecular Clouds

In the interstellar medium, huge clouds of molecular gas and dust are observed. These clouds have a wide range of masses and sizes. The smallest, known as Bok globules after their discoverer (Bok & Reilly, 1947), have masses of the order 10 $M_\odot$ and span a distance the order of a parsec. There are intermediate-mass molecular clouds which have masses of 10^3 to 10^4 $M_\odot$, and sizes between 2 and 15 pc (Cambresy, 1999). However, most of the molecular gas mass is situated within giant molecular clouds (GMCs for short) which can have masses as high as 10^7 $M_\odot$, and span $\sim$ 200 pc across (Blitz, 1993; Murray, 2011).

Molecular clouds are cold, typically with temperatures of between 10 to 20 K (Bergin & Tafalla, 2007). Their high visual extinctions, caused by the high column density of dust particles, prevents heating by starlight, while any heating due to cosmic rays is far

outweighed by cooling via atomic and molecular lines and dust emission. These high extinctions have the consequence that molecular clouds are difficult to observe at optical wavelengths. Although molecular hydrogen (H_2) was first detected by Carruthers (1970) using UV absorption from stellar radiation and constitute the majority of the mass in a molecular cloud, H_2 is a homonuclear molecule, with no allowed rotational energy levels and a first allowed transition at UV wavelengths. Therefore H_2 is not excited at temperatures as low as 10 K, which means that it is difficult to observe at infrared wavelengths (although rotational and rovibrational emission lines from molecular hydrogen have been observed in regions experiencing shocks - see Evans 1999). For this reason, observations of molecular cloud structure generally use another molecule, predominantly CO (Wilson et al. (1970) first detected CO at 2.6 mm wavelengths), as a tracer of the distribution of H_2 in a region. Therefore structure and kinematics of molecular clouds is mostly observed by using the $J = 1 - 0$ emission line of ^{12}CO, with a conversion 'X' factor to account for differences in the CO and H_2 abundances.

These observations of the kinematics of molecular clouds show that they are driven by supersonic turbulence. For gas at temperatures between 10 and 20 K, the speed of sound is ~ 0.2 km s^{-1}. But molecular line studies find velocities greater than 0.2 km s^{-1}, which show that the gas is supersonic. Kolmogorov's theory for turbulence describes how energy can cascade down from large-scale, macroscopic gas motions to small-scale 'eddies' (Kolmogorov, 1941). One prediction derived from Kolmogorov's theory is that the velocity dispersion σ of turbulent gas in a molecular cloud will scale with the cube root of the cloud's linear size L:

$$\sigma \propto L^{1/3} \tag{1.1}$$

Larson (1981) used observations of L and σ (measured primarily from the width of ^{12}CO and ^{13}CO emission lines, as well as the width of emission lines of a number of other molecules) to derive an empirical law relating the two:

$$\sigma(\text{km s}^{-1}) = 1.10 L(\text{pc})^{\beta} \tag{1.2}$$

where $\beta = 0.38$. More recent studies by Heyer & Brunt (2004) give a value for β as 0.5. The resemblance of Larson's empirical law to Kolmogorov's theoretical is explained if molecular clouds are turbulent. A complete review of turbulence (which is out of the scope of this thesis) can be found in Ballesteros-Paredes et al. (2007)

Observations of molecular clouds also show that they have a hierarchical density structure, which is typically divided into three levels - 'clouds', 'clumps' and 'cores'

(Bergin & Tafalla, 2007). Most of the mass of a molecular cloud has a density which is too low to form stars. The typical mean particle number density of a molecular cloud is between 50 and 500 cm^{-3}. Clumps tend to be around 20 times less massive than their parent clouds, with masses of 50 to 500 $M_\odot$, sizes on the order of a parsec and mean number densities of 10^3 to 10^4 cm^{-3}. Cores have typical masses of 0.5 to 5 $M_\odot$, sizes of 0.03 to 0.2 pc and densities of 10^4 to 10^5 cm^{-3}. Cores are the site of star formation and are covered in the next subsection. Molecular clouds are also highly filamentary, with these filaments containing ~ 70 % of pre-stellar cores (e.g. André et al. 2014 and references therein).

1.1.2 Pre-stellar Cores

Molecular cores are the densest parts of a molecular cloud and are the sites of star formation. However, not all cores will form stars. This thesis defines the molecular cores which will collapse under gravity to form stars as 'pre-stellar cores'. The criterion which determines whether a core will collapse under gravity is called the Jeans criterion (Jeans, 1902), and the mass threshold at which collapse will occur is the Jeans mass M_J, given by:

$$M_\mathrm{J} = \frac{\pi}{6}\frac{c_\mathrm{s}^3}{G^{3/2}\rho^{1/2}} \tag{1.3}$$

where c_s is the speed of sound of the gas in the pre-stellar core and ρ is the mass density. A derivation of the Jeans mass is found in Binney & Tremaine, but it can be understood in terms of the virial theorem. A gas cloud is in virial equilibrium if:

$$2T + \Omega = 0 \tag{1.4}$$

where T is the cloud's thermal energy and Ω is its gravitational potential energy. If $\Omega > 2T$, then the gravitational potential energy is strong enough to overcome the outward thermal pressure and the cloud will collapse. This occurs when the cloud has a mass $m_\mathrm{c} = M_\mathrm{J}$. Therefore, if $m_\mathrm{c} > M_\mathrm{J}$, then the core will collapse under gravity to form stars. If $m_\mathrm{c} < M_\mathrm{J}$, then the core will not form stars.

This picture is complicated by the presence of both turbulence and magnetic fields. As mentioned above, molecular clouds are driven by supersonic turbulence. This causes shocks within the molecular cloud which results in the over-densities which allow the mass in a region to be greater than the Jeans mass (Padoan & Nordlund, 2002). While turbulence therefore helps to drive star formation, the presence of magnetic fields within the molecular cloud act to keep the core stable against collapse (Crutcher, 1999; Hen-

nebelle & Chabrier, 2008). One way of taking into account the effect of turbulence and magnetic fields on the Jeans mass is to replace c_s with an effective speed $c_{\rm eff}$ as:

$$c_{\rm eff} = c_s + c_A + \frac{\langle c_t^2 \rangle}{3} \tag{1.5}$$

where c_A is the Alfvén speed and $\langle c_t^2 \rangle$ is the rms velocity dispersion of the gas due to turbulence (Lou 1996, Mac Low & Klessen 2004).

Pre-stellar cores are observed to have a range of masses. This mass distribution, also known as the 'core mass function' (CMF), resembles a Salpeter power law (Salpeter, 1955) with a peak at $\sim$ 1 $M_\odot$ (Alves et al., 2007; Nutter & Ward-Thompson, 2007). The lack of pre-stellar cores with masses less than 1 $M_\odot$ can be explained by the Jeans mass. As $M_{\rm J} \propto \rho^{-1/2}$, a greater density is required for a lower-mass star, and although turbulent flows can easily compress enough gas for a 1 $M_\odot$ core, a 0.1 $M_\odot$ core requires a density 100 times greater. The lack of cores with significantly higher mass than 1 $M_\odot$ is because these more massive cores tend to undergo fragmentation.

Before outlining the physical theory behind the evolutionary stages from the collapse of a pre-stellar core to the eventual formation of a star, it is useful to look at the different observed categories of YSO which make up those evolutionary stages. This is the focus of the next subsection.

1.1.3 Observational Classes of YSO

There are several observational categories, or classes of YSO, which are also thought to make up a evolutionary sequence. The primary observational property which distinguishes these different categories is the slope α of their spectral energy distribution (SED), primarily at infrared wavelengths, given by: (Lada, 1987; Adams et al., 1987; André et al., 1993, 2000; Evans et al., 2009):

$$\alpha = \frac{d \log \lambda F_\lambda}{d \log \lambda} \tag{1.6}$$

where F_λ is the flux density measured at wavelength λ. Idealised SEDs for the Classes 0, I, II and III YSOs are shown in Figure 1.1.

Class 0 YSOs are thought to be in the first stages of star formation, when a pre-stellar core first begins to collapse. Class 0 YSOs consist of an infrared source embedded in an extended envelope of molecular gas. Their SED resembles that of a black body with an excess of emission at sub-millimetre wavelengths (André et al., 1993). Observations of

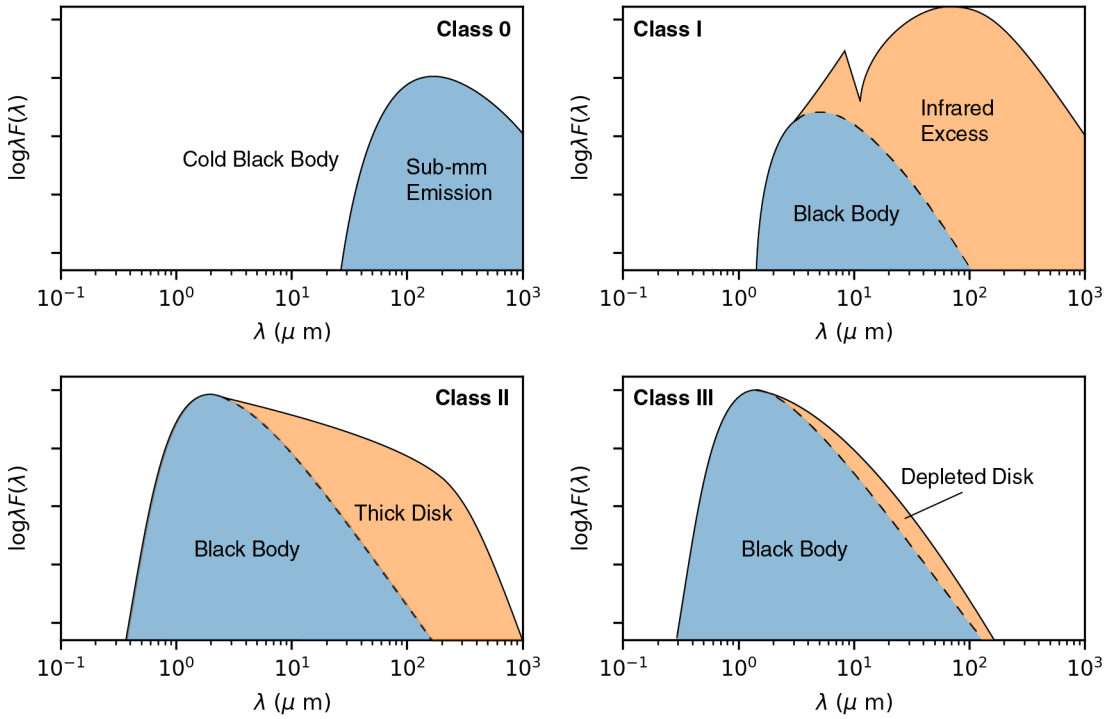

Figure 1.1: Idealised spectral energy distributions (SEDs) for the four main observational categories of young stellar object - Class 0 (top-left), Class I (top-right), Class II (bottom-left) and Class III (bottom-right). Based on a figure from Persson (2014).

the kinematics of Class 0 YSOs imply that the gas is falling inwards towards the centre (Mardones et al., 1997), supporting the notion that what is being observed is a collapsing pre-stellar core. Class 0 objects have been observed to have powerful collimated jets with velocities of order 10^2 to 10^3 km s^{-1} (Frank et al., 2014). Driven by accretion and strong magnetic fields, these jets in turn drive large-scale outflows of molecular gas.

The observationally-derived lifetime of Class 0 YSOs is approximately 1.5×10^5 yr (Dunham et al., 2014), after which it becomes a Class I object. Chen et al. (1995) found from observations of YSOs that none of their YSOs observed with a Class 0 SED had a bolometric temperature greater than 70 K. Therefore 70 K is the established temperature threshold for distinguishing between Class 0 and Class I objects. Class I objects are still embedded in an infalling envelope so cannot be observed at optical wavelengths. From Figure 1.1, it is evident that the SED of a Class I YSO has an excess of IR radiation, caused primarily by radiation from the object being recycled by the extended envelope.

Class 0 and Class I objects both come under the umbrella term 'protostar', which has a lifetime of approximately 0.5 Myr before it evolves into a pre-main sequence (PMS) star, which covers both Class II and Class III objects.

Class II YSOs are no longer embedded in their natal envelope and are therefore visible at optical wavelengths. Also called classical T Tauri stars (CTTs), after their archetype star T Tauri (Joy, 1945), they consist of a dense central object surrounded by a massive accretion disk, which gives its SED an infrared excess and is responsible for Hα and X-ray radiation as it accretes onto the star. This accretion also produces powerful jets.

While T-Tauri stars have an upper mass of ~ 2 M$_\odot$, they have a high-mass analogue known as Herbig Ae/Be stars with masses up to ~ 8 M$_\odot$ (stars with masses above this evolve immediately onto the main sequence).

Class III YSOs (also known as weak-lined T Tauri stars) are distinguished from CTTs by their weak IR excess, indicating the depletion of their accretion disk.

The observed classes of YSO show an evolutionary sequence starting from a collapsing molecular cloud and ending with a Class III pre-main sequence star with a depleted circumstellar disk. The physics of how a YSO evolves from the former class to the latter is described in Section 1.1.4 below.

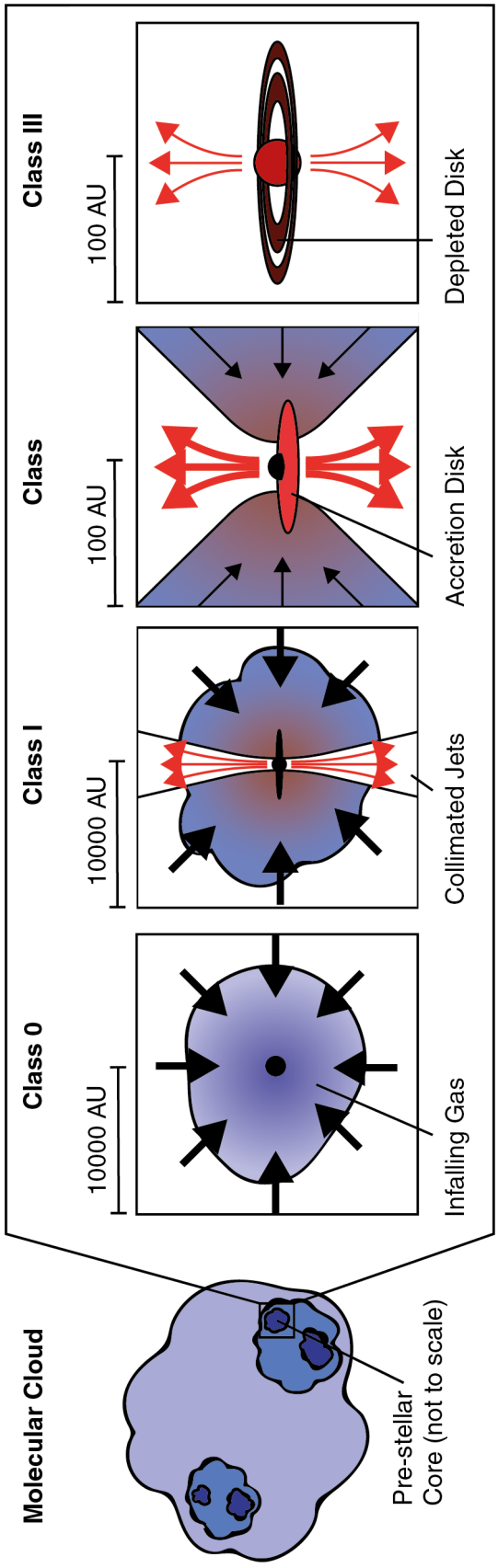

Figure 1.2: Showing the different stages of star formation, from molecular cloud to Class III pre-main sequence star.

1.1.4 Formation of Low-Mass Stars

While the classes above give the observational properties of YSOs, the evolution of a YSO is just as likely to be described in terms of its physical stages which, while broadly analogous to the observational classes above, do not match exactly.

Furthermore, there are differences with how low-mass ($M < 8$ M$_\odot$) stars and high-mass ($M > 8$ M$_\odot$) stars form. Here I outline the general formation of low-mass stars, while the specific challenges of high-mass star formation is tackled in Section 1.1.5 below. The physics of the gravitational collapse of a 1 M$_\odot$ pre-stellar core with an initial temperature and density of 10 K and 10^{-20} g cm^{-3} respectively is outlined in detail by Masunaga & Inutsuka (2000b,a).

The formation of a low-mass star begins with the collapse of the pre-stellar core. The molecular gas which makes up the pre-stellar core is initially optically thin to the sub-mm radiation emitted by the dust grains in the core, therefore it is efficient at radiating away the gravitational potential energy released by the collapse. Because of this, the collapse is initially isothermal and occurs on a free-fall timescale, defined as (Masunaga & Inutsuka, 2000b):

$$t_{ff} \equiv \left(\frac{3\pi}{32G\rho_0}\right)^{\frac{1}{2}} \tag{1.7}$$

For a 1 M$_\odot$ core with a radius of 10000 AU, the timescale for this isothermal collapse is $\sim 10^5$ yr.

The isothermal collapse phase ends when the core's optical depth is of the order of unity, corresponding to a density of $\sim 10^{-13}$ g cm^{-3}. This increase in density allows a protostar (usually several) to form near the centre. The increased density also makes it optically thick and so unable to efficiently radiate energy, which causes it to increase in temperature.

The increasing thermal pressure changes the collapse from isothermal to adiabatic. The object is now known as the first hydrostatic core and collapses on a much longer timescale as the outward thermal pressure of the object counteracts its gravitational collapse (this timescale is called the Kelvin-Helmholtz timescale). Before the transition from isothermal collapse to adiabatic collapse, it becomes more likely that the YSO will fragment into multiple protostars. The Jeans mass, given by Equation 1.3, is the lower mass limit necessary for fragmentation to occur, and is inversely proportional to the density of the gas. During the initial isothermal collapse, the gas increases in density, leading to a decrease in the Jeans mass. However, the Jeans mass is also proportional to the sound speed c_s which is proportional to the thermal energy of the gas - when

the temperature starts to increase c_s, and hence the Jeans mass, increases with it. As the Jeans mass *decreases* during the isothermal phase, the likelihood of fragmentation *increases*. As the Jeans mass *increases* during the adiabatic phase, the likelihood of fragmentation *decreases* again. There therefore exists a minimum value for the Jeans mass during collapse. This minimum Jeans mass is called the opacity limit for fragmentation and has the value $M_J \sim 0.007$ $M_\odot$ (Low & Lynden-Bell, 1976).

The first adiabatic collapse ends when the temperature rises to $\sim$ 2000 K. At this temperature molecular hydrogen is dissociated. The thermal energy holding up the core against collapse goes into dissociating the H_2 and a second quasi-isothermal collapse occurs until the object reaches stellar densities, at which point it has become a pre-main sequence star. The PMS star contracts slowly over the timescale of a few Myr, before hydrogen ignition occurs in the star's core and it joins the Main Sequence.

1.1.5 High-Mass Stars

Like their low-mass counterparts, high-mass stars form from the collapse of a cloud of molecular gas. We observe what is thought to be the earliest stage of formation of massive stars in infrared dark clouds (IRDCs) (Rathborne et al., 2010). However, because high-mass stars are able to begin core hydrogen burning while they are still embedded within their natal envelope, their journey from molecular cloud to Main Sequence star is difficult to observe directly.

Moreover, the formation of high-mass stars requires a much larger amount of gas than the formation of low-mass stars. A young, high-mass star is highly luminous and releases a huge amount of energy in the form of radiation and powerful stellar winds. This stellar feedback dissociates the surrounding gas, creating a HII region and acting as a brake on further mass gain. Therefore, one challenge of high-mas star formation is how very massive (such as observed 100 $M_\odot$) stars can form. The initial gas reservoir must be massive enough not just to form the star itself, but to counteract the effect of stellar feedback.

1.1.6 Core Accretion and Competitive Accretion

There are two proposed mechanisms for allowing a massive enough gas reservoir to form massive stars. The first, known as 'monolithic collapse' (Zinnecker & Yorke, 2007) or 'core accretion' (Krumholz et al., 2005, 2007, 2009; Tan et al., 2014) proposes that the initial conditions for the formation of a high-mass star is a sufficiently massive and

dense molecular clump or core. This core collapses quickly, while accreting mass onto the central massive protostar via an accretion disk, which mitigates the problem of feedback by providing an optically-thick barrier which shields the material in the outer disk against the radiative force of the stellar winds.

One challenge for this theory to address is how to prevent a clump or core with ~ 100 Jeans masses of material from fragmenting into lower-mass cores. It is possible that the effect of feedback and the contribution from magnetic fields may hinder fragmentation.

The second proposed mechanism is 'competitive accretion' (Bonnell et al., 2001, 2004; Bonnell & Bate, 2006). In the competitive accretion scenario, protostars which reside in the denser regions of a molecular clump are more likely to become massive. As they gain mass, their gravitational sphere of influence expands and they are able to accrete yet more of the gas from their surroundings, which causes their mass to increase further. This results in a positive feedback loop with the star using its greater mass to more effectively accumulate more mass. In this scenario, the gas necessary to form a massive star comes partly from the star's initial position in the densest part of a cluster, and partly from the massive star's ability to 'hoover-up' mass from its surroundings.

To some extent, the distinction between 'isolated' and 'competitive' models is if massive stars form in 'clustered' environments or 'associations'. Here we use 'cluster' to refer to dense, bound groups of stars, and 'associations' as unbound groups of stars (see Section 1.3.1). In a clustered environment stars are expected to encounter one another and 'know' that other stars are present, which is not necessarily true in an association.

Distinguishing between these models of massive star formation is difficult. A common prediction of competitive models is that massive stars require a gas- and star-rich dynamical environment to form, and so massive stars will form in 'clusters', but in isolated models massive stars can form in regions with few other stars with no 'knowledge' of other star formation.

This has motivated searches for 'isolated' massive stars which are not associated with 'clusters' (e.g. Lamb et al. 2010; Oey et al. 2013; Bressert et al. 2012). However, it is known that some/many isolated massive stars have been ejected from dense clusters (Fujii & Portegies Zwart, 2011; Oh et al., 2015) and so a definitive identification as a massive star as having *formed* in relative isolation is difficult.

Core accretion and competitive accretion make further predictions of the initial mass function and primordial mass segregation which are explained in Section 1.3 below.

This section has mainly dealt with isolated star formation, from the fragmentation and collapse of molecular cloud, to the observational categories of young stellar objects,

to the physics of low and high-mass star formation. However, the possibility of core fragmentation introduced in part 1.1.4 shows that a pre-stellar core can produce not just one star in isolation, but a system of several stars. The details of how multiple systems form and their importance to the dynamical evolution of young stellar regions is the focus of the next section.

1.2 Young Multiples

Section 1.1 above mainly focused on the formation of a single star in isolation. However, most stars form in binary or multiple systems. The notion that multiple star formation may be the dominant mode of star formation was first proposed by Larson (1972) when drawing conclusions from simulations of the collapse of a rotating pre-stellar core.

Observations of YSOs show that most reside in binary or multiple systems. It is useful to first define two quantitative terms which are used to describe the numbers of multiple systems in a region - the multiplicity frequency MF and the companion fraction CF (Reipurth & Zinnecker, 1993).

The multiplicity frequency MF of a region is defined as the ratio of the total number of multiple systems in that region, divided by the total number of systems (including single stars), ie.:

$$MF = \frac{B + T + Q + ...}{S + B + T + Q + ...} \tag{1.8}$$

where B, T, Q etc. are the total numbers of binary systems, triples, quadruples and so on. The companion fraction CF is defined as the average number of companions that each star in a region has, and is given by:

$$CF = \frac{B + 2T + 3Q + ...}{S + B + T + Q + ...} \tag{1.9}$$

Because Class 0 YSOs are embedded in their natal envelopes, observations of Class 0 multiples are performed at sub-mm or longer wavelengths. For example, Chen et al. (2013) observed 33 Class 0 YSOs within 500 pc of the Sun with the Submillimeter Array and measured a multiplicity frequency $MF = 0.64 \pm 0.08$, with a companion fraction $CF = 0.91 \pm 0.05$. Tobin et al. (2016) found a multiplicity frequency for Class 0 objects in the Perseus molecular cloud with separations up to 10000 AU as $MF = 0.57 \pm 0.09$ with a companion fraction $CF = 1.2 \pm 0.2$.

One the other hand, observations of Class I YSOs give lower CF values, from 0.18 ± 0.04 (Haisch, Jr. et al., 2004) to 0.27 ± 0.06 (Duchêne et al., 2004) to 0.47 ± 0.08

(Duchêne et al., 2007). In addition, it appears that most stars on the Main Sequence are single (Lada, 2006) - Raghavan et al. (2010) found that $\sim 56\%$ of solar-type stars in the solar neighbourhood are single stars. Therefore there appears to be a discrepancy between the number of very young YSOs found in multiples, compared to the number of Main Sequence stars, implying that there are physical processes which destroy multiple systems over time.

There are other reasons why multiple star formation is important to study. The observed multiplicity is different in different regions. King et al. (2012) collated the multiplicity fractions of a several different young stellar regions and showed that it can vary significantly from region to region (e.g. $MF = 0.42 \pm 0.08$ for binaries with separation $a > 1000$ AU for Taurus, but only 0.085 ± 0.01 for the ONC) and from the field (e.g. Duchêne et al. 2018).

However, it is difficult to use the *observed* multiplicity of a region as a proxy for the fraction of multiples which initially form via core fragmentation, because multiple systems are heavily dynamically processed as this section will explain. This dynamical processing may itself give a useful insight into the dynamical past of a region however. This notion forms the basis of the investigations in Chapters 4 and 5.

Therefore this section begins by describing how multiple systems can form primordially, before going on to its main focus which is the dynamics of multiple systems. This section describes how binary systems can form dynamically through three-body encounters and through the 'soft capture' mechanism which is further explored in Chapter 5. This section then addresses the dynamical destruction of binary and multiple systems via unstable decay, encounters with other stars and the tidal effect of the galactic field.

1.2.1 Primordial Formation of Binaries and Multiples

It is widely understood that binary and multiples form primordially, via the fragmentation of a collapsing pre-stellar core (Larson, 1972; Low & Lynden-Bell, 1976; Boss & Bodenheimer, 1979). If a pre-stellar core has angular momentum due to rotation or turbulence (see review by Goodwin et al. 2007), this can occur at several possible stages. The initial fragmentation occurs when a molecular cloud fragments into pre-stellar cores. These pre-stellar cores may then form stars which have a separation of 10^3 – 10^4 AU, close enough to be a gravitationally-bound multiple system. Fragmentation can occur during the first isothermal collapse to give separations of 10^2 – 10^3 AU, or during the first adiabatic phase to give separations of the order of 10^0 – 10^2 AU, or during the second collapse to give separations of 10^{-2} – 10^{-1} AU (Machida et al., 2005, 2008; Kauffmann

et al., 2008). Multiple systems may also form via the fragmentation of a circumstellar disk which has been perturbed either by a neighbouring star or by turbulence (Goodwin et al., 2007; Offner et al., 2010).

Simulations show that the formation of multiples is a primary mode of star formation. Bate (2009) showed that large-scale simulations of collapsing turbulent molecular clouds could match observed multiplicity frequencies and properties of multiple systems. Offner et al. (2009) found that radiative feedback can dampen the rate of star and multiple formation, but Bate (2012) showed that simulations incorporating radiative feedback can still match observations, and Lomax et al. (2015) showed that stellar feedback which is episodic (rather than continuous) can match the observed multiplicity of stellar regions. Magnetic fields are also another way of reducing the rate of multiple formation (Price & Monaghan, 2007; Myers et al., 2013; Federrath & Klessen, 2012), while still producing many multiple systems (Federrath, 2016).

1.2.2 Dynamical Formation of Binaries and Multiples

It is also possible, given the right conditions, for a binary system to form via dynamical encounters. The rate at which an encounter between any two stars (defined as an event in which two stars pass by each other close enough that the change in their potential energy is greater than their total kinetic energy) in a region will occur is given by (Binney & Tremaine, 1987):

$$\tau_{\rm enc} \simeq 3.3 \times 10^7 \,{\rm yr} \left(\frac{100\,{\rm pc}^{-3}}{n}\right) \left(\frac{v_{\rm inf}}{1\,{\rm km/s}}\right) \left(\frac{10^3\,{\rm AU}}{r_{\rm min}}\right) \left(\frac{{\rm M}_\odot}{M_{\rm bin}}\right) \tag{1.10}$$

where n is the stellar number density of the region, $v_{\rm inf}$ is the mean relative speed at infinity of the objects in the cluster, $r_{\rm min}$ is the minimum encounter distance and $M_{\rm bin}$ is the total mass of the two stars. Equation 1.10 can be written in terms of the cluster mass M, cluster half-mass radius $R_{1/2}$ and average stellar mass $\bar{m}$ (Malmberg et al., 2007) as:

$$\tau_{\rm enc} \simeq 5 \times 10^7 \,{\rm yr} \left(\frac{\bar{m}}{{\rm M}_\odot}\right) \left(\frac{R_{1/2}}{1\,{\rm pc}}\right)^{\frac{5}{2}} \left(\frac{100\,{\rm M}_\odot}{M}\right)^{\frac{1}{2}} \left(\frac{10^3\,{\rm AU}}{r_{\rm min}}\right) \left(\frac{{\rm M}_\odot}{M_{\rm bin}}\right) \tag{1.11}$$

For a typical star forming region ($M = 500$ M$_\odot$, $R_{1/2} = 0.5$ pc, $M_{\rm bin} = 1$ M$_\odot$, $\bar{m} = 0.6$ M$_\odot$ and $r_{\rm min} = 1000$ AU), $\tau_{\rm enc} \sim 2.4$ Myr. The dependence on the masses of the two stars involved in the encounter shows the importance of gravitational focusing.

However, if two stars experience a close encounter with one another, conservation

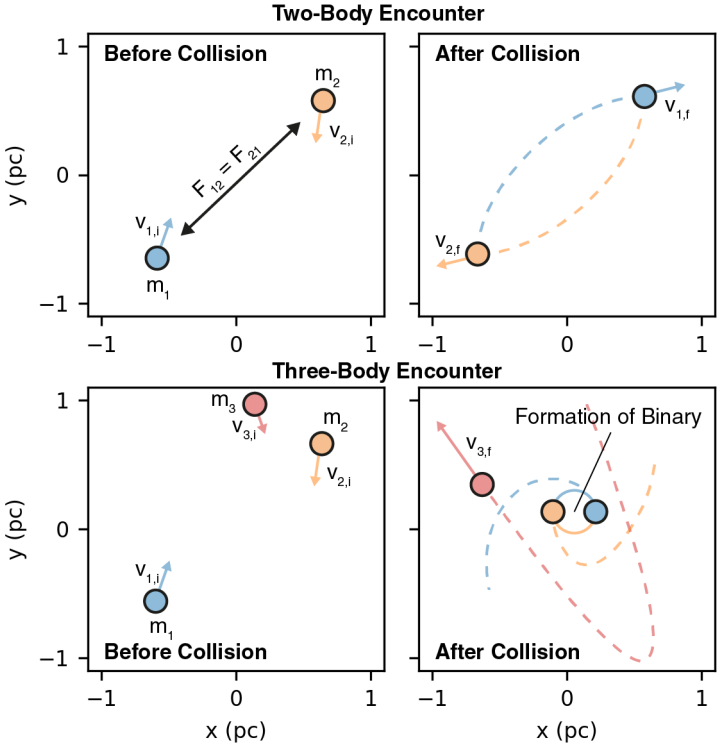

Figure 1.3: Showing the effect of a two-body collision (top) and that of a three-body collision (bottom) in forming a binary system. In a two-body collision Star 1 (blue) and Star 2 (orange) exchange energy but the total energy of the system remains conserved, which means no binary can form. In a three-body collision Star 3 (red) gains energy and escapes the vicinity. This loss of energy allows Stars 1 and 2 to form a binary.

of energy dictates that they will not form a binary, unless there is a way to remove energy from the interacting star-star system. Therefore, in order to dynamically form a binary, a two-body encounter is not sufficient, and a three-body encounter is necessary (Goodman & Hut, 1993). Gravitational interactions can transfer enough energy to one of the three stars, so that the other two stars are able to become gravitationally bound. Having gained a significant amount of energy, the third star can escape at high velocity (see Figure 1.3).

The rate of binary formation via three-body encounters per unit volume $\dot{N}_{\rm bin}$ is a function of the individual star masses m, the region's number density n and the velocity dispersion σ:

$$\dot{N}_{\rm bin} = 0.75 \frac{G^5 m^5 n^3}{\sigma^9} \tag{1.12}$$

The Galactic field typically has $n \sim 0.03$ pc^{-3} and $\sigma \sim 50$ km s^{-1}, which gives a value for $\dot{N}_{\rm bin}$ of the order 10^{-21} pc^{-3} Gyr^{-1}, which means the chance of binaries forming dynamically in the Galactic field is negligible. However, a dense star forming region such as the Orion Nebula Cluster (ONC) has $n \sim 5000$ pc^{-3} and $\sigma \sim 2$ km s^{-1}, which gives a value for $\dot{N}_{\rm bin}$ of the order 1 pc^{-3} Myr^{-1}, which means that the dynamical formation of binaries can be a feasible mode of binary formation in young star forming regions.

Allison & Goodwin (2011) showed how simulated massive stars in dense clusters dynamically form binary systems with other massive stars. These massive binary systems may sometimes form higher-order Trapezium-like, named after the Trapezium cluster at the centre of the the Orion Nebula Cluster. This dynamical formation of a massive binary can have dramatic consequences for the region in which it forms. The binding energy of a binary is given by:

$$E_{\rm bind} = -\frac{GM_1M_2}{2a} \tag{1.13}$$

where M_1 and M_2 are the masses of the two stars and a is the separation between them. A massive binary can have a binding energy which is as large as the total energy of the rest of the cluster. When this binary forms, it therefore acts as an energy sink - the magnitude of the energy of the rest of the cluster decreases and the cluster responds by expanding. This effect can be powerful enough to gravitationally unbind a cluster, causing it to disperse into the field. This mechanism is briefly described in Allison & Goodwin 2011 and is explored further in Chapter 6.

A further way of forming VWBs is via the 'soft capture' mechanism during the dissolution of a star cluster (Kouwenhoven et al., 2010; Moeckel & Bate, 2010). This

occurs because the aggregate gravitational influence of the stars in an expanding cluster becomes less powerful over time, relative to the influence of two stars which remain in close proximity to one another during the expansion. As this mechanism is important for the investigations in Chapter 5, it is explained in more detail there.

1.2.3 Destruction of Binaries and Multiples

Binaries and multiples are changed and destroyed dynamically, both from within and from without. A cloud core fragments to form a multiple system, but most multiple systems are unstable - only $\sim 10\%$ of triple systems are dynamically stable enough to survive long-term (Reipurth et al., 2010). Interactions between the stars tend to kick one star into a wider orbit while simultaneously contacting the separation between the other two stars. In some cases, the third star may be ejected completely. Observationally, a triple system with a third star on a very wide orbit with two very close inner stars may resemble a very wide binary. Other, higher-order multiples may also be unstable and decay.

Binaries and multiples may also have their properties altered, or be destroyed outright, by encounters with other stars. The rate of encounter between a binary with a collision cross section Σ and a third star in a region with a stellar number density n and a velocity dispersion σ is approximated as (Binney & Tremaine, 1987):

$$t_{enc} \simeq \frac{1}{n\Sigma\sigma} \tag{1.14}$$

Heggie (1975) and Hills (1975) first studied the dynamical destruction of binaries and showed that binaries can be categorised based on the likelihood that they will be destroyed in an encounter with a third, perturbing star (sometimes called the perturber for short).

They categorised a binary as 'hard' if the binding energy of the binary $E_{\rm bind}$ (given by Equation 1.13) is much greater than the typical energy in an encounter $E_{\rm enc}$. Hard binaries are unlikely to be destroyed in an encounter. In fact, any encounter with a third star is likely to cause the binary to lose energy and become more tightly bound, i.e. harder.

A binary is categorised as 'soft' if its binding energy is much less than the typical energy in an encounter. Soft binaries can be destroyed in an encounter, particularly if the perturber is a massive star. Moreover, any encounters which do not destroy a soft binary tend to make the binary softer still, so that it becomes easier to destroy over

time.

As well as 'hard' and 'soft' binaries, it is useful to define 'intermediate' binaries as binaries whose binding energy is of the order of the typical encounter energy. An intermediate binary may be destroyed in an encounter or it may survive, depending on its encounter history (Parker & Goodwin, 2012).

As shown by Hills (1990) it is often better to consider the velocity of a perturber, rather than simply the energy. During an encounter of a binary system with primary and secondary masses $m_{\rm p}$ and $m_{\rm s}$ and semi-major axis a, with a perturbing star with mass $m_{\rm pert}$, the critical velocity $v_{\rm c}$ is defined as the velocity at which the total energy of the three bodies involved in the encounter is zero, given by:

$$\left(v_{\rm c} = \frac{G m_{\rm p} m_{\rm s} (m_{\rm p} + m_{\rm s} + m_{\rm pert})}{m_{\rm pert} (m_{\rm p} + m_{\rm s})\, a} \right)^{\frac{1}{2}} \tag{1.15}$$

If the perturber velocity $v_{\rm pert} << v_{\rm c}$, then the binary will not be destroyed. However the properties of the binary may be altered by an energy exchange, and it is possible to have an exchange of members (typically if the perturber is of higher mass than the secondary).

Whether a binary will survive or be disrupted depends not only on the energy/velocity of an encounter, but the rate of encounters close enough to disrupt the binary. The encounter rate, $t_{\rm enc}$, is inversely proportional to both the number density and velocity dispersion, $\propto 1/(n\sigma)$ (see e.g. Binney & Tremaine, 1987). In a virialised cluster of radius R, the encounter rate will therefore depend on the crossing (dynamical) timescale, $t_{\rm cross} = R/\sigma$, of the cluster as $t_{\rm enc} \propto t_{\rm cross}^3/R$. In addition, the velocity of encounters has a dependency $\sigma \propto n^{1/2} R$ which complicates any estimates of encounter rates.

In this section, the importance of binary and multiples, their formations and destruction due to dynamical effects were discussed. This discussion implies that these multiple systems reside in regions in which many other stars are in close enough proximity that dynamical encounters can occur. In fact, young stars are typically found not just in binary and multiple systems, but in large extended groups. These groups are the focus of the next section.

1.3 Young Stellar Regions

Most young stars are observed to be in 'clustered' environments. Lada & Lada (2003) used a survey of YSOs within ~ 2 kpc of the sun to conclude that the fraction of YSOs

situated within 'embedded clusters' is between 70% and 90%. The definition used for 'cluster' includes any group of stars with a total stellar number $N > 35$, with a total stellar mass $M_\star > 1\ M_\odot\ pc^{-3}$. Lada & Lada (2003) decide on these criteria by setting a lower limit of the evaporation timescale t_{ev} (given approximately by $t_{ev} \simeq 100\ t_{cr}$ where t_{cr} is the crossing time) at 100 Myr, the average lifetime of an open cluster (Adams & Myers, 2001), with a density large enough to survive encounters with passing molecular clouds (Spitzer, 1958).

The definition from Lada & Lada (2003) covers anything with a star formation surface density greater than ~ 3 YSO pc^{-2}. But it is broad enough to encompass a large spread of observed sizes and densities, from dense, centrally-concentrated clusters like the Orion Nebula Cluster (up to 10^3 pc^{-2}) to diffuse, unbound associations such as Cygnus OB2 (average of around 10 pc^{-2}). There are other definitions which primarily aim to distinguish further between dense 'clusters' (which are generally thought to either be gravitationally bound to to have been bound when it formed) and 'associations' which are deemed as looser agglomerations of stars which are not gravitationally bound, yet appear to have formed from the same clump of molecular gas.

Gieles & Portegies Zwart (2011) distinguish between clusters and associations by using the ratio of the age of the stars $A_\star$ over the crossing time t_{cr}, where $t_{cr} \propto R/\sigma$ and R and σ are the radius and velocity dispersion of the region respectively. They refer to this ratio as the dynamical age Π:

$$\Pi = \frac{A_\star}{t_{cr}} \tag{1.16}$$

For a cluster which is gravitationally bound and therefore not expanding, R and therefore t_{cr} are approximately constant over time, so Π increases linearly with respect to A. For an unbound association, t_{cr} increases approximately linearly as R increases over time (as σ also increases over time), meaning that Π stays approximately constant. In this way, the evolution of Π over time can distinguish between 'clusters' and 'associations', and the crossing time t_{cr} gives a clue as to how different clustered environments may dynamically evolve.

Although clusters and associations appear to be important with regards to finding young stars and learning more about the environments in which stars form, YSOs are found at all densities. Bressert et al. (2010) measured the YSO surface density Σ_{YSO} in a number of star forming regions within 500 pc. They found that the distribution of Σ_{YSO} is smooth and continuous from 10^{-2} to 10^3 YSOs pc^{-2}, with a peak at ~ 22 YSOs pc^{-2}. This is used as evidence against discrete modes of star formation and that stars can form at any densities, although the YSOs observed by Bressert et al. (2010) are class

II and class III objects, which means that they are already a few Myr old which leaves time for dynamical processing to have occurred.

It is evident that the regions in which we observe young stars have widely varied physical properties. This thesis broadly uses the definitions of Gieles & Portegies Zwart (2011) - A 'cluster' is gravitationally bound while an 'association' is unbound (although an association may itself contain dense subregions which are themselves bound). For the purpose of this thesis, both 'clusters' and 'associations' come under the umbrella term 'young stellar region', which broadly follows the Lada & Lada (2003) definition of 'cluster'. The investigations in Chapters 4 - 6 aim to shed light on how young stellar regions dynamically evolve and whether it is possible to use observations of the properties of young stellar regions to probe their dynamical past. This section proves context by describing some notable properties of young stellar regions, before describing the dynamical processes which drive their evolution.

Young stellar regions have a range of physical properties based on their populations of stars and gas, and these properties help to determine the different ways in which these regions can dynamically evolve. This section outlines the main properties of young stellar regions, before tackling some of the main topics for the dynamical evolution of young stellar regions.

1.3.1 The Initial Mass Function

The stars which populate a young stellar region have a range of masses. When talking about the mass spectrum of a region, it is standard to refer to the initial mass function (IMF), which is the distribution of masses of a group of stars *at birth* (stars undergo mass loss from e.g. stellar winds so masses of stars on the Main Sequence change over time, and stars can be ejected from the region, changing the overall distribution).

There have been several different formulations of initial mass functions, beginning with Salpeter (1955) who formulated an IMF between 0.4 and 10 $M_\odot$ as:

$$N(M)dM \propto M^{-2.35}dM \tag{1.17}$$

Two other popular formulations of initial mass functions are Kroupa (2001) and Chabrier (2003). Kroupa (2001) introduced a parameterised the IMF into three sections which are each described by a power law $N(M) \propto M^{-\alpha}$, with different values for α. For a stellar mass $M < 0.08$ $M_\odot$, $\alpha = 0.3$, for stellar mass between $0.08 < M < 0.5$ $M_\odot$ $\alpha = 0.5$ and for $M > 0.5$ $M_\odot$ $\alpha = 2.3$, similar to the Salpeter IMF.

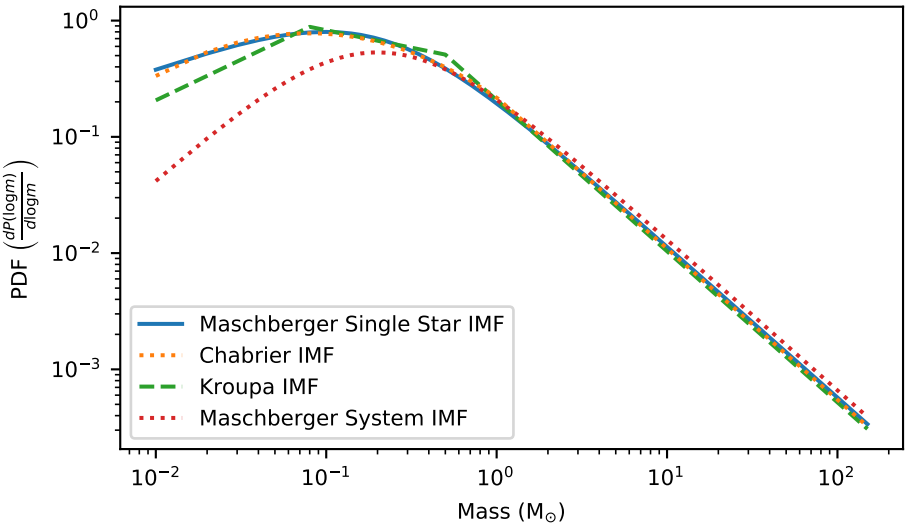

Figure 1.4: The different formulations for the initial mass function (IMF) of a stellar region, using the IMFs and method from Kroupa (2001); Chabrier (2003); Romano et al. (2005); Maschberger (2013).

Chabrier (2003) also introduced a parameterised IMF with two sections. For $M > 1$ $M_\odot$ the IMF is a power law with $\alpha = 2.3$ similar to the Kroupa and Salpeter IMFs. For $M < 1$ $M_\odot$ the IMF is given by a log-normal function:

$$N(M)dM = 0.158(1/(\ln(10)m))\exp[-(\log(m) - log(0.08))^2/(2 \times 0.69^2)] \quad (1.18)$$

Maschberger (2013) provides a generalised form of an IMF which matches the Chabrier IMF with with both log-normal and power law sections, whilst minimising the number of parameters necessary to describe said function, which makes it useful for dynamical simulations of stellar populations and is therefore used in Chapters 4 - 6.

Figure 1.4 shows the different formulations for the IMF of a region. For all formulations, the IMF declines rapidly at high-M, as high-mass ($M > 8$ $M_\odot$) stars are very rare. For $M < 0.08$ $M_\odot$ objects, their mass is not high enough to ignite hydrogen fusion in their core. These objects make up the Galactic brown dwarf population, which we ignore as they are dynamically unimportant due to their low mass. Figure 1.4 also shows that the IMF is affected by unresolved multiple systems Kroupa (2001); Chabrier (2003), which requires knowledge of the multiplicity statistics of a region to correct.

Even though young stellar regions can have very different properties, observations of stellar populations in a wide variety of stellar regions support the notion that the IMF is universal, i.e. it is the same regardless of the specific conditions present in each star

forming region. (Bastian et al., 2010) reviewed observations of stellar populations in clusters and in the Galactic field and found no evidence of a variable IMF.

The reason for the apparent universality of the IMF is not obvious. The main parameter which governs the collapse of a pre-stellar core is the Jeans mass $M_{\rm J}$, which relies on both the density and the thermal properties of a region (see Equation 1.3). But different regions of the Galaxy have very different densities and thermal properties, which makes it surprising that these differences do not affect the stellar mass distribution.

One possible explanation for the origin of the IMF is the core mass function (CMF) introduced in Section 1.1.2. 1.1.2. The shape of the CMF is observed to have the same shape as the IMF, but with the peak shifted from ~ 0.2 M$_\odot$ to ~ 1 M$_\odot$, implying that the stellar IMF is determined by the CMF which preceded it. However, the fact that the cores fragment into smaller cores means that the shape of the CMF is not sufficient on its own to explain the IMF.

The 'competitive accretion' scenario introduced in Section 1.1.6 also aims to explain the origin of the IMF (Bonnell & Bate, 2006) In competitive accretion, the IMF does not rely on the CMF, as the gas which is accreted onto a massive protostar initially inhabits a large area rather than a single pre-stellar core. Simulations have shown that the competitive accretion scenario can replicate the low-mass IMF (Bate, 2009, 2012).

1.3.2 Virial Theorem and Dynamical Timescales

The virial theorem, given by Equation 1.19, relates the total kinetic energy T to the total gravitational potential energy U for a stable, self-gravitating stellar region. A star forming region which is gravitationally bound will tend towards the equilibrium given by Equation 1.19 and a gravitationally bound star forming region which is very unstable will rapidly change its properties in order to regain that equilibrium. For instance, as we will see later, the rapid loss of mass from a region will cause it to expand in order to regain its virial equilibrium.

$$2\langle T\rangle + \langle U\rangle = 0 \tag{1.19}$$

Three other parameters which are derived from the virial theorem are the virial radius $R_{\rm vir}$, the virial velocity $V_{\rm vir}$ and the virial ratio $Q_{\rm vir}$. The virial radius and the virial velocity are the radius of the region and the mean velocity of the stars in a region for which virial equilibrium holds, and are given by Equations 1.20 and 1.21 respectively,

where M is the region's mass and $E = T + U$ is its total energy.

$$R_{\rm vir} = \frac{GM^2}{2|E|} \tag{1.20}$$

$$V_{\rm vir} = \sqrt{\frac{2|E|}{M}} \tag{1.21}$$

The virial ratio $Q_{\rm vir}$ is defined as:

$$Q_{\rm vir} = \frac{T}{-U} \tag{1.22}$$

When $Q_{\rm vir} = 0.5$, then Equation 1.19 holds and the gravitationally bound stellar region is close to virial equilibrium. If $Q_{\rm vir} < 0.5$, then the gravitational component dominates the kinetic component and the region will contract due to gravity. If $0.5 < Q_{\rm vir} < 1.0$, then the kinetic component dominates and the region will expand. Regions with $Q_{\rm vir} > 1.0$ are gravitationally unbound and expanding and therefore will never achieve virial equilibrium.

The useful time scales necessary to describe the dynamical evolution of a group of stars are the *crossing time* and the *relaxation time*. The crossing time $t_{\rm cr}$, is an estimate of the time it takes for a typical star to cross the cluster, and also the time it takes for a self-gravitating system to reach dynamical equilibrium. It is defined in terms of $R_{\rm vir}$ and $V_{\rm vir}$ given by equations 1.20 and 1.21 above:

$$t_{\rm cr} = \frac{R_{\rm vir}}{V_{\rm vir}} = G\left(\frac{M^5}{8|E|^3}\right)^{\frac{1}{2}} \tag{1.23}$$

If the cluster is approximately in virial equilibrium, then $V_{\rm vir} = \sqrt{GM/R_{\rm vir}}$ and equation 1.23 becomes (Spitzer, 1987):

$$t_{\rm cr} = \left(\frac{R_{\rm vir}^3}{GM}\right)^{\frac{1}{2}} \simeq 2 \times 10^4\,{\rm yr}\left(\frac{M}{10^6\,{\rm M}_\odot}\right)^{-\frac{1}{2}}\left(\frac{R_{\rm vir}}{1\,{\rm pc}}\right)^{\frac{3}{2}} \tag{1.24}$$

The crossing time for many stellar clusters is of the order of 1 Myr. However, a dense, massive region such as the Arches cluster ($M \sim 2 \times 10^4$ M$_\odot$; $R_{\rm vir} \sim 0.68$ pc, Figer et al., 1999) can have a crossing time 100 times smaller, and more extended regions may have a crossing time of tens of Myr, showing that dense, massive regions can dynamically change much more quickly than more extended regions.

The relaxation time of a cluster is the time it takes for the cluster to reach thermal

equilibrium, and is typically much larger than its dynamical time. It is estimated as the time it takes for a star to change its energy by an amount equal to the mean stellar energy. If m is the local mean stellar mass and ρ is the local density, then the relaxation time $t_{\rm r}$ is given by:

$$t_{\rm r} = \frac{\langle v^2 \rangle^{3/2}}{15.4 G^2 m \rho \ln \Lambda} \tag{1.25}$$

The parameter Λ is proportional to the number of stars N and depends on the mass and velocity distributions of the stars in the cluster, ranging from $0.4N$ for equal-mass stars whose velocity distribution is isotropic (Spitzer, 1987).

If the cluster is in virial equilibrium, then Equation 1.25 can be approximately related to $t_{\rm cr}$ using Equation 1.24 to give:

$$t_{\rm r} \simeq \frac{N}{8 \ln N} t_{\rm cr} \tag{1.26}$$

1.3.3 Structure, Kinematics and the Removal of Substructure

Observations show that, similar to the molecular clouds in which they are formed, stellar clusters and associations exhibit large amounts of substructure (Goodwin & Whitworth, 2004). The Q-parameter (Cartwright & Whitworth, 2004, 2009; Parker, 2014) is used as a way to measure substructure in stellar regions. What follows is a brief explanation of the Q-parameter.

In the context of graph theory, a tree is a graph in which the points are connected by a path with no closed loops. If an edge is defined as a segment of the tree which directly connects two points, then the length of a tree is found by summing the lengths of all edges in the tree. There are a multitude of possible trees for any set of points. A minimum spanning tree (MST) for a set of points is the tree whose length m is less than the length of all other possible trees. Figure 1.5 shows the MST between a group of points distributed in space.

If a random subset of stars within a group of stars of number N has an MST of length m, then a mean MST length $\bar{m}$ can be found by taking a large number of MSTs of random subsets of stars and dividing by that number. The Q-parameter for that group of stars is then then ratio of the mean MST length $\bar{m}$ over the mean separation between all stars in the group $\bar{s}$:

$$Q = \frac{\bar{m}}{\bar{s}} \tag{1.27}$$

If $Q < 0.8$ then the spatial distribution of the group of stars appears fractal, whereas if $Q > 0.8$ then the spatial distribution appears centrally condensed. Observations of

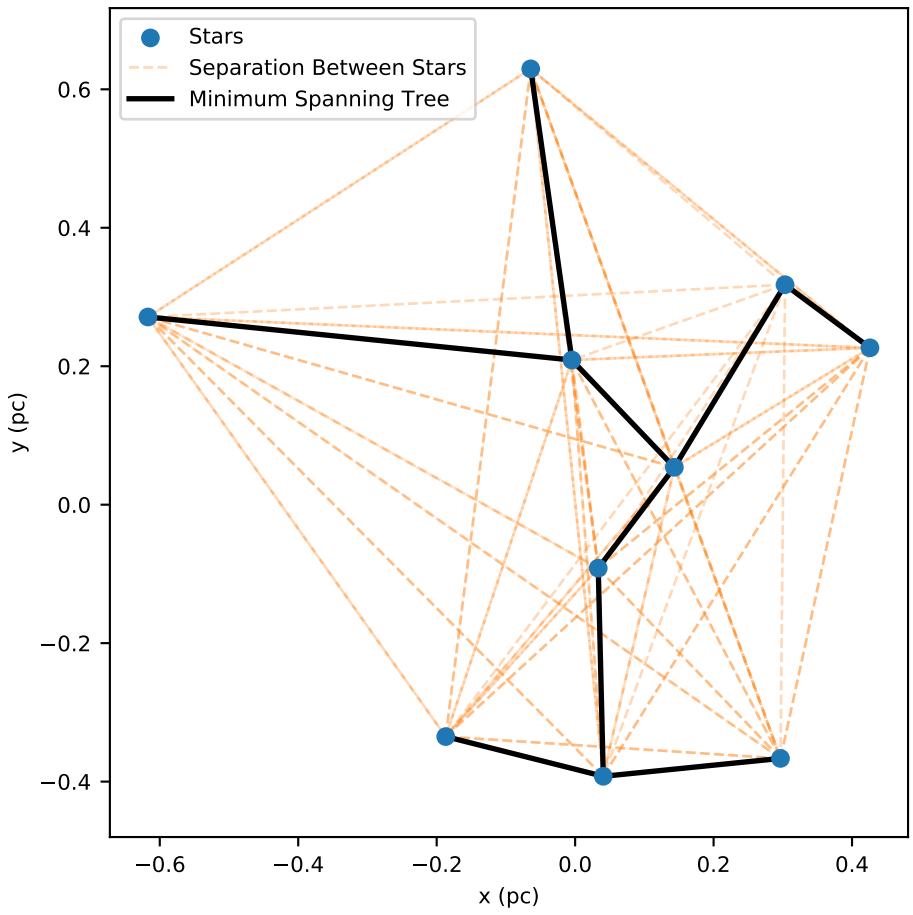

Figure 1.5: Showing the minimum spanning tree (MST, in black) for a distribution of stars and the separations between each pair of stars (orange). The MST connects all the points, with no closed loops, by the shortest possible total length.

nearby clusters and associations show that many show signs of density substructure using the Q-parameter (Cartwright & Whitworth, 2004, 2009; Wright et al., 2014).

As with molecular clouds, kinematic substructure is also present in star forming regions. For example, Da Rio et al. (2014) and Da Rio et al. (2017) show that stars in the ONC exhibit kinematic substructure which mirrors the kinematic substructure of the the molecular gas. Observations of the proper motions of the association Cygnus OB2 (Wright et al., 2016) also show that it contains significant kinematic substructure.

Both the density and kinematic substructure of star forming regions can be dynamically erased. Aarseth & Hills (1972) showed that substructure in low-N regions would disappear within a free-fall timescale, while Goodwin & Whitworth (2004) found that substructure survived longer in regions for which $Q_{\rm vir} > 0.5$. The erasure of substructure, as measured by the Q-parameter, could be used as a diagnostic to give insight into the dynamical past of a region (Parker & Goodwin, 2012).

Parker (2014) showed that, due to dynamical processing, the Q-parameter for gravitationally-bound dense regions only ever increases, meaning that low-Q regions must have always had a low Q value and therefore could not have evolved from a high-Q region. Wright et al. (2014) used this result to show that the existence of substructure in the association Cygnus OB2 means that it cannot have formed as a dense, centrally-condensed cluster, but must instead have been formed much as it is now - clumpy and extended.

1.3.4 Primordial and Dynamical Mass Segregation

Some observed star forming regions exhibit mass segregation, in which the high-mass stars are found in close proximity compared to the average separation between all of the stars in the region. For example, the Trapezium system in the centre of the Orion Nebula Cluster (ONC) shows evidence of mass segregation (Hillenbrand & Hartmann, 1998; Allison et al., 2009a). As with measurements of substructure, one of the methods used to measure mass segregation involves the use of the minimum spanning tree (MST). The mean MST length $\bar{m}$ is again found by taking a large number of MSTs of random subsets of stars and dividing by that number. The $\Lambda_{\rm MST}$-parameter is then the ratio of the mean MST length $\bar{m}$ over the length of the minimum spanning tree which joins all of the stars above a chosen mass threshold:

$$\Lambda_{\rm MST} = \frac{\bar{m}}{m_{\rm massive}} \tag{1.28}$$

If $\Lambda_{\rm MST}$ is equal to unity then there is no mass segregation in the region. The higher $\Lambda_{\rm MST}$ is above unity, the more evidence for mass segregation. For example, Allison et al. (2009a) find $\Lambda_{\rm MST} = 8.0 \pm 3.5$ for the innermost 4 stars of the ONC, with evidence of mass segregation ($\Lambda_{\rm MST} = 2.0 \pm 0.5$) for the nine stars in the ONC with $M > 5$ M$_\odot$.

Simulations show that mass segregation can be primordial. The competitive accretion scenario (Bonnell et al., 1997), explained in Section 1.1.6, proposes that the molecular cores which are destined to form high-mass stars are situated in the denser, gas-rich parts of molecular clumps. Hence, the high-mass stars of a region should be situated close together relative to the average separation of stars in the region.

However, some young stellar regions do not show signs of mass segregation (Wright et al., 2014; Gennaro et al., 2017), implying that primordial mass segregation is not an intrinsic par of the star formation process. However, this in itself is not enough to discount competitive accretion, as simulations of warm (expanding) young stellar regions show competitive accretion with no mass segregation (Parker & Dale, 2017).

Mass segregation also occurs dynamically, as a consequence of two-body interactions between stars. Allison et al. (2009b) showed that dynamical mass segregation can occur rapidly, i.e. in less than 1 Myr, but Allison et al. (2010) and Parker (2014) showed that, once mass segregation has occurred, it does not necessarily remain, as high-mass hierarchical systems can decay rapidly, ejecting high-mass stars out of the region.

1.3.5 Evaporation

Evaporation occurs when a star in a region has a velocity $v_\star$ which is greater than the escape velocity of the region. For an isolated, self-gravitating cluster, the escape velocity $v_{\rm esc}$ is given by (Spitzer, 1987):

$$v_{\rm esc} = 2 \left\langle v^2 \right\rangle^{\frac{1}{2}} \tag{1.29}$$

For a group of stars with a Maxwellian velocity distribution, there will be a fraction (~ 0.74 %) of stars for which $v_\star > v_{\rm esc}$ and these stars will escape in roughly a relaxation timescale. This gives a rough estimate for the evaporation timescale - the time it would take for a cluster to dissolve due to evaporation - as $t_{\rm ev} \simeq 137 t_{\rm r}$. For even a relatively dense young stellar region such as the Orion Nebula Cluster, $r_{\rm rel} \sim 1.4$ Myr, Portegies Zwart et al., 2010), the time it would take for the cluster to disperse via evaporation is ~ 190 Myr. This however is complicated by the fact that stellar regions are rarely isolated, and tidal effects and the star's trajectory on which it escapes have an impact on the evaporation time.

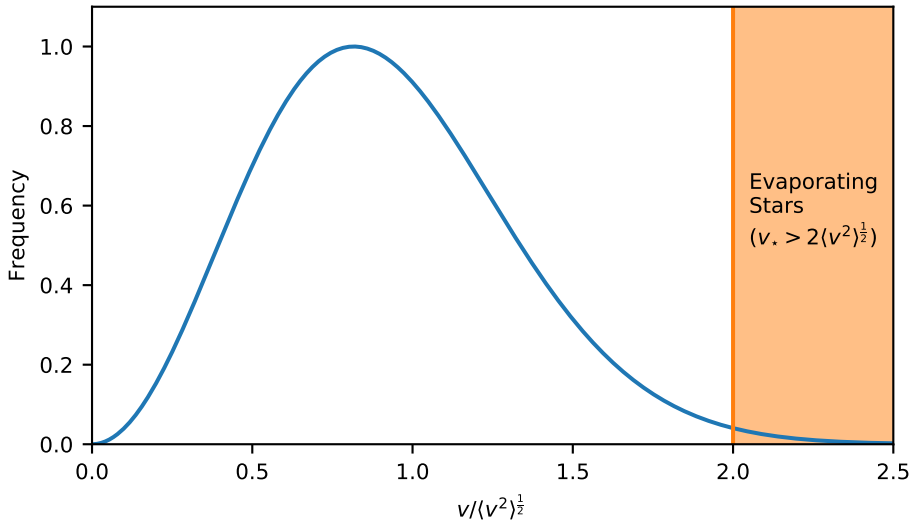

Figure 1.6: Showing the escape velocity for a system of stars with a velocity distribution. The tail of evaporating stars with $v > v_{\rm esc}$ is highlighted.

1.3.6 Core Collapse and Violent Relaxation

The effects of both two-body relaxation and evaporation cause energy to be transferred between stars and therefore cause changes in the energy distribution of the stellar region. Specifically, energy is transferred from the core of the region to the periphery. The virial theorem given by Equation 1.19 shows that, for a self-gravitating stellar system, a decrease in the total energy of the system should cause that system to contract. Therefore, as energy is transferred from the core of the region to the periphery, the core undergoes a collapse and the periphery expands (Spitzer, 1987).

This core collapse is a fundamental dynamical effect of a self-gravitating system of massive particles, and applies as much to a galaxy as it does to a star cluster. For a Plummer sphere (see Section 2.7.4) in which all stars are of equal mass, the time it would take for a core to collapse to infinite density is $\sim 15 t_{\rm r}$.

For a stellar region with a mass distribution, another consequence of core collapse is dynamical mass segregation. As the cluster approaches energy equipartition, more massive stars subsequently have lower velocities than less massive stars, causing the more massive stars to congregate in the centre of the cluster. For a Plummer distribution, this mass segregation occurs approximately within the relaxation timescale (Bonnell & Davies, 1998). However, for a sub-virial, substructured region, dynamical mass segregation due to core collapse can occur much more rapidly (Allison et al., 2009b)

Dynamical evolution of a stellar region on two-body relaxation timescales is applicable

to a fixed gravitational potential. However, a star cluster with a varying potential can change much more rapidly. Lynden-Bell (1967) shows that, if the potential of a star cluster is changing on a timescale equal to approximately the dynamical timescale, then the stars in that cluster can change their energy on a timescale approximately equal to the crossing time of the cluster. This so-called 'violent relaxation' was first used to show why galaxies and massive globular clusters appear to be relatively close to dynamical equilibrium despite their relaxation timescales being longer than the lifetime of the observable universe, but it is also useful to show how any star cluster can quickly dynamically evolve if its potential changes.

1.3.7 Gas Expulsion and Infant Mortality

Because stars form from clouds of molecular gas, young stellar regions are observed to contain enough gas to make up a significant fraction of their total mass. The star formation efficiency (SFE) of a region ϵ_{sf} is given by (Lada & Lada, 2003):

$$\epsilon_{\rm sf} = \frac{M_\star}{M_\star + M_g} \tag{1.30}$$

where $M_\star$ is the stellar component of the total mass of the region and M_g is the gas component.

Lada & Lada (2003) give the typical value for $\epsilon_{\rm sf}$ as between 10 – 30%, meaning that the gas component has a profound effect on the region's dynamical evolution.

The most dramatic consequence of the presence of interstellar gas is the potential destruction of the cluster due to gas expulsion. Massive stars have powerful stellar winds and short lifetimes, at the end of which they release huge amounts of energy in the form of supernovae. These feedback mechanisms have the effect of expelling the gas from a cluster. If the change in the total cluster mass due to gas expulsion is large enough, then the cluster becomes supervirial and rapidly disperses, a process called 'infant mortality' (Lada & Lada, 2003; Goodwin & Bastian, 2006; Baumgardt & Kroupa, 2007). Only ~ 10 % of clusters survive the first few millions of years.

The likelihood that gas expulsion will destroy a cluster is thought to partly depend on its value of $\epsilon_{\rm sf}$. Hills (1980) posited that instantaneous gas loss in a cluster with $\epsilon_{\rm sf} < 50$ % would cause it to disperse. This value has since been revised down to ~ 33 % (Goodwin, 1997). If the gas is expelled on adiabatic timescales, then the threshold value of $\epsilon_{\rm sf}$ drops to ~ 20 %.

However, the likelihood of infant mortality also depends on the dynamical state of the

cluster before gas expulsion occurs. The *effective* star formation efficiency $\epsilon_{\rm esf}$ (Goodwin & Bastian, 2006; Goodwin, 2009) is given by:

$$\epsilon_{\rm esf} = \frac{1}{2Q_\star} \tag{1.31}$$

where $Q_\star$ is the virial ratio of the cluster (see Equation 1.22) *immediately after gas expulsion*. This value therefore depends on the dynamical state of the stars - if they are dynamically 'hot' (i.e. $Q_\star > 1$) then dispersal after gas expulsion is more likely than if they are 'cold'. Smith et al. (2011) argue that the useful parameters to determine the survival of gas expulsion by a cluster is the initial stellar distribution and velocity dispersion, that $\epsilon_{\rm sf}$ is not an effective measure for predicting the survival of a cluster and that stochasticity plays a large role.

1.4 The Scope of This Thesis

The aim of this thesis is to introduce original research which provides new insights into how young stellar regions evolve, by performing numerical simulations of the dynamical interactions between stars and stars and gas. Three outstanding questions in star formation to which this research aims to propose answers are outlined below.

1.4.1 How do young stellar regions evolve (and die)?

There are many potential ways that a young stellar region may form, evolve and eventually die. For example, the theory of 'clustered' star formation proposes that most (or even all) stars form in dense clusters approximately 1 pc across containing thousands of stars (Kroupa, 2011). These dense clusters disperse over time due to gas expulsion (See section 1.3.7) to become the more diffuse associations we observe. In this view, dense star clusters are a necessary step in the birth and early evolution of young stellar regions (and hence also a necessary step in the birth and early evolution of stars and planets).

Conversely, 'hierarchical' star formation uses the observations of young stars at a wide range of densities (Bressert et al., 2010) to propose that star formation does not occur just within dense clusters, but instead occurs at a wide range of densities (Wright et al., 2014). In this view, dense clusters are not a necessary step in the evolution of young stellar regions but are instead merely an extreme case.

Whether dense star clusters are important or unimportant has further consequences for theories of star formation including the theories of massive star formation introduced

in Section 1.1.6. The 'competitive accretion' scenario favours a clustered environment in which stars 'compete' for a shared gas reservoir, while 'monolithic collapse' proposes that massive stars can form in isolation.

The reality of the formation of young stellar regions is likely to be a mixture of both 'clustered' and 'hierarchical' mechanisms, with the composition of that mixture depending on the environment in which the young stellar region resides. The investigations in Chapters 4, 5 and 6 further our understanding of the importance of these two mechanisms.

Similarly, there are open questions around how young stellar regions die. Even taking a cluster with a relatively short relaxation time (the Orion Nebula Cluster, $r_{\rm rel} \sim 1.4$ Myr, Portegies Zwart et al., 2010), the time it would take for the cluster to disperse via evaporation alone would be ~ 190 Myr, yet only 10% of young stellar regions survive longer than 10 Myr (so-called 'infant mortality').

The accepted wisdom is that a cluster whose total mass is dominated by its gas component may become gravitationally unbound if that gas is rapidly removed due to stellar feedback (i.e. stellar winds and supernovae - see Section 1.3.7 and Baumgardt & Kroupa, 2007). However, the chance of gas expulsion causing the death of a cluster depends on the dynamical state of the cluster immediately before gas expulsion (Goodwin & Bastian, 2006; Goodwin, 2009), and also depends on the gas in the centre of the cluster not being depleted in other ways. Chapter 6 shows that the mechanisms which give rise to infant mortality may be more complicated than previously understood.

1.4.2 What diagnostics can we use to determine the past of a young stellar region?

The dynamics of a region have an effect on how the properties of that region change over time. In the same vein, the properties of a region may provide insights into how the properties of that region may have changed.

One example of this is the erasure of substructure from a young stellar region. Parker (2014) showed that substructure is erased in dense regions but not in more diffuse regions and proposed several measures of substructure to give an indication of the past properties of a young stellar region.

Another example is multiplicity. Binary systems are not just formed primordially; they also evolve dynamically through their interactions with each other and their interactions with other stars that they may encounter. As binary systems can form and be changed and even destroyed dynamically through encounters with other stars, then it

follows that the number and properties of binaries may change depending on the properties of their surrounding environment. The numbers and properties of binary systems may be different if it has resided in a region which was previously dense (with a high chance of dynamical encounters) compared to a region which has never been dense (a low chance of dynamical encounters). Therefore, it may be possible to use the numbers and properties of binary systems as a diagnostic to determine how a young stellar region may have evolved. This idea is further developed in Chapter 4.

1.4.3 If most stars form in clusters, how does this affect the properties of the Galactic field stellar population?

Most young stars are found in regions which are much denser than the average density of the Galactic field (Lada & Lada, 2003). As only 10% of young stellar regions survive longer than 10 million years, the other 90% must disperse into the Galactic field. Therefore, there is a link between the properties stars and systems in young stellar regions and the properties of stars and systems in the field.

However, the origin of the properties of the Galactic field stellar population is not immediately clear. For example, in the Galactic field there resides a number of wide binary systems with separations greater than 10000 AU (5% of Galactic-field G-dwarf stars are members of one of these binary systems Duquennoy & Mayor, 1991). However, these systems are too weakly gravitationally bound to survive at the density of the average young stellar region. The origin of thee Galactic field very wide binaries is therefore currently unknown, and is a question which is explored further in Chapter 5.

1.5 The Structure of This Thesis

This chapter is divided into four sections, each of which outline the context of how stars form and the regions in which we observed young stars. Section 1.1 introduced the broad strokes of how a star forms from the collapse of a molecular cloud, including what see see when we observe these as young stellar objects, the physics of the collapse and the specific challenges of high-mass stars. Section 1.2 introduced multiple systems, their formation and dynamical destruction. Section 1.3 introduces young stellar regions as the main locations we observe young stars, the properties of these regions and how dynamical interactions between stars and gas can significantly affect the evolution of the region as a whole. Finally, Section 1.4 gives the context for Chapters 4, 5 and 6 in the form of three unanswered questions in the field of star formation.

In the next two chapters, the numerical methods for modelling how young stellar regions evolve are described. These numerical methods are also the methods which are used for the investigations in Chapters 4, 5 and 6. Chapter 2 introduces N-body simulations which are used to model the dynamical evolution of stars. Chapter 3 then introduces smoothed particle hydrodynamics, which are used to model the dynamical evolution of gas.

Chapter 4 uses the dynamical processing of binary systems outlined in Section 1.2 to show how the presence of massive wide binary systems in a region can help us to gain insight into the dynamical past of that region. Chapter 5 shows how the presence of a population of binary systems with very wide separations may be explained by the dynamical processes outlined in Sections 1.2 and 1.3. Chapter 6 revisits the concept of star formation efficiency and gas expulsion explained in Section 1.3 and shows that perhaps gas expulsion is not as important as thought in the dispersal of young stellar regions. Finally, in light of the results of Chapters 4, 5 and 6, the questions above are revisited in the conclusion (Chapter 7).

Chapter 2

N-body Methods

2.1 Introduction

Stars interact with one another via the force of gravity. The result of the gravitational force acting on a star by its neighbours is to change that star's dynamical properties, i.e. its position, velocity and acceleration. The aggregate effect of the changing of the dynamical properties of stars in a region due to gravitational interactions is to change the dynamical properties of the region as a whole (see Section 1.3 for examples of this). One way of predicting how a group of stars will dynamically evolve is by using numerical simulations, such as the N-body simulations which are the topic of this chapter.

The 'N-body problem' is the name given to the problem of predicting the future dynamical properties of a group of N stars whose initial properties are known. Given a closed system consisting solely of two stars, the N-body problem can be solved analytically to predict the dynamical properties of those two stars at any given time. However, with the exception of a few specific scenarios, the $N \geq 3$ N-body problem cannot be solved analytically, but is instead solved using numerical methods. 'N-body simulation' is the catch-all term for the numerical methods which seek to solve the N-body problem and track the dynamical evolution of groups of stars.

In this chapter, I begin in Section 2.2 by introducing the simple first principles which are necessary for all N-body methods. I then describe several N-body methods, beginning in Section 2.3 with one of the simplest, Eulers method. The more sophisticated predictor-corrector methods are then introduced in Section 2.4, before the introduction in Section 2.5 of the fourth-order Hermite scheme, which is one of the most commonly used N-body schemes and is the scheme which is most relevant for the rest of this thesis. The formulation of the crucial individual timestep scheme is then explained in Section

2.6. Finally, the methods behind the generation of useful initial conditions are outlined in Section 2.7.

2.2 First Steps

Stars interact according to Newton's law of gravity, which states that the gravitational force $\mathbf{F}_i$ acting on a body i within a group of N bodies is:

$$\mathbf{F}_i = -Gm_i \sum_{j=1;\, j\neq i}^{N} \frac{m_j(\mathbf{r}_i - \mathbf{r}_j)}{|\mathbf{r}_i - \mathbf{r}_j|^3} \tag{2.1}$$

where m_i, m_j and $\mathbf{r_i}$, $\mathbf{r_j}$ are the masses and positions of bodies i and j respectively.

For N-body schemes, the masses, positions and velocities of the stars are typically scaled so that the gravitational constant G is equal to unity (see Section 2.7.2). The equation of motion of a body i can then be written as:

$$\mathbf{a}_i = -\frac{d^2\mathbf{r}_i}{dt^2} = \sum_{j=1;\, j\neq i}^{N} \frac{m_j(\mathbf{r}_i - \mathbf{r}_j)}{|\mathbf{r}_i - \mathbf{r}_j|^3} \tag{2.2}$$

Given the position $\mathbf{r}_i(t_0)$ and velocity $\mathbf{r}_i(t_0)$ of a body i at time t_0, in addition to the positions and masses of all other particles j, integrating Equation 2.2 finds $\mathbf{r}(t)$ and $\mathbf{v}(t)$ at any future time t. However, Equation 2.2 can only be integrated analytically for $N = 2$, necessitating the use of numerical integration to find approximate solutions for $N > 2$.

The basic approach to the numerical integration of an ordinary differential equation is to first rewrite it as a set of n first-order differential equations with the general form:

$$\frac{dy_i(x)}{dx} = f_i(x, y_1, ..., y_n); \quad i = 1, ..., n \tag{2.3}$$

For example, the equation of motion $\mathbf{a} = \frac{d^2\mathbf{r}}{dt^2}$ can be written as:

$$\mathbf{a} = \frac{d\mathbf{v}}{dt}; \quad \mathbf{v} = \frac{d\mathbf{r}}{dt} \tag{2.4}$$

These two first-order differential equations are then solved numerically. The simplest method for doing so is called Euler's method and is the topic of the next section.

2.3 Euler's Method

Let the equation to be integrated be a first-order differential equation $\frac{dy}{dt} = f(t, y)$, with a starting point at $y(t_0) = y_0$. An approximate solution at a point $y(t_1) = y_1$ can be found by first finding the equation of the tangent line at t_0:

$$y = y_0 + f(t_0, y_0)(t - t_0) \tag{2.5}$$

If the interval between t_1 and t_0 is sufficiently small, then:

$$y_1 \simeq y_0 + f(t_0, y_0)(t_1 - t_0) \tag{2.6}$$

This can be generalised to find the approximate solution at any point y_{n+1}, using the previous point y_n and the interval $t_{n+1} - t_n = \Delta t$:

$$y_{n+1} \simeq y_n + f(t_n, y_n)\Delta t \tag{2.7}$$

The time interval (or 'timestep') Δt is of central importance to N-body methods. Reducing the size of Δt typically decreases the difference between the approximate solution and the actual solution, thereby increasing the accuracy of the simulation. However, reducing Δt also increases the total number of calculations within a simulation, thus increasing its run-time and computational cost.

The application of Euler's method to the first-order differential equations in Equation 2.4 gives approximate solutions for the position $\mathbf{r}_{n+1}$ and velocity $\mathbf{v}_{n+1}$ of a star at time t_{n+1} as:

$$\begin{aligned} \mathbf{r}_{n+1} &= \mathbf{r}_n + \mathbf{v}_n \Delta t \\ \mathbf{v}_{n+1} &= \mathbf{v}_n + \mathbf{a}_n \Delta t \end{aligned} \tag{2.8}$$

By calculating the acceleration $\mathbf{a}_n$ for each star using Equation 2.2, its approximate future position and velocity can then be predicted.

The standard way of measuring accuracy in N-body simulations is to use the conservation of total energy $E = T + \Omega$, where:

$$T = \frac{1}{2} \sum_{j=0}^{N} m_j \left|\mathbf{v}_j\right|^2 \tag{2.9}$$

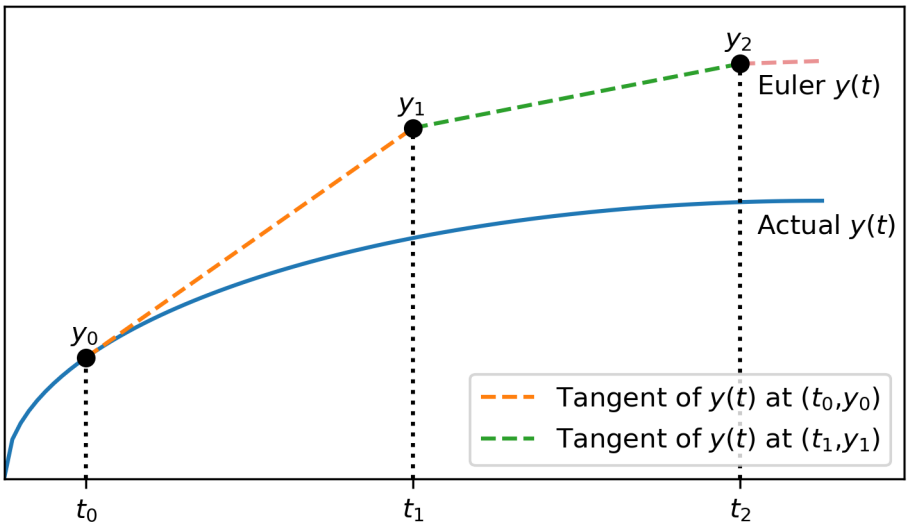

Figure 2.1: Euler's method of integrating an ordinary differential equation. The tangent of $y(t)$ at each point $(t_n,\ y_n)$ is used to approximate the value of y at the next point $(t_{n+1},\ y_{n+1})$. While Euler's method is simple to implement, it produces an error $\mathcal{O}(\Delta t)$, which makes it too inaccurate for use in numerical simulations of groups of stars.

and:

$$\Omega = -Gm_i \sum_{j=0, j\neq i}^{N} \frac{mj}{|\mathbf{r}_{ij}|} \tag{2.10}$$

For an ideal simulation with 100% accuracy, the calculated total energy will stay constant from the beginning to the end of the simulation, i.e. $\Delta E = E_{\text{final}} - E_{\text{initial}} = 0$. In reality, no numerical attempt at an approximate solution will be 100% accurate, but instead the error ΔE will be proportional to the size of the timestep Δt. For this reason, the choice of an appropriate value for Δt is vital and is dependent on the region being simulated (further discussion of the choice of timestep is found in Section 2.6 below).

Euler's method is a first-order approximation, meaning that the error of the solution is of the order of the timestep Δt (or, written another way, the error is $\mathcal{O}(\Delta t)$ - if the size of the timestep is decreased by 10, the corresponding error in calculation decreases by approximately by 10. Predicting the motion of a group of stars to the necessary accuracy would require an impracticably small timestep and an impracticably large computation time. Therefore more efficient, higher-order methods are used in practice. For the simulation of groups of stars, a fourth-order method is typically deemed sufficient and the fourth-order Hermite scheme is a widely used scheme for this reason. The Hermite scheme, which is used used for the N-body and hybrid simulations in Chapters 4, 5 and

6, is an example of a 'predictor-corrector' method, which is explained in the next section.

2.4 Predictor-Corrector Methods

A predictor-corrector method is a way of improving on the accuracy of Euler's method by splitting the numerical integration into two steps:

1. The 'prediction' step, which uses y_n to calculate an approximate predicted value y^{p}_{n+1}, typically using an explicit method (such as Euler's method in Section 2.3).

2. The 'correction' step, which uses y_n and y^{p}_{n+1} to refine the initial prediction using an implicit method to get a corrected value y^{c}_{n+1}.

The most basic predictor-corrector method is a modification of Euler's method. It predicts the value y^{p}_{n+1} using equation 2.7 and then refines the solution by calculating the mean of the gradient of the tangent at $f(t_{n+1}, y^{\mathrm{p}}_{n+1})$ and $f(t_n, y_n)$:

$$y^{\mathrm{c}}_{n+1} \approx y_n + \frac{\Delta t}{2}[f(t_{n+1}, y^{\mathrm{p}}_{n+1}) + f(t_n, y_n)] \tag{2.11}$$

The corrector step can be applied more than once, at the cost of computational speed, to iteratively increase the accuracy of the solution.

The modified Euler method applied to the first-order differential equations in Equation 2.4 yields the prediction step:

$$\begin{aligned} \mathbf{r}^{\mathrm{p}}_{n+1} &= \mathbf{r}_n + \mathbf{v}_n \Delta t \\ \mathbf{v}^{\mathrm{p}}_{n+1} &= \mathbf{v}_n + \mathbf{a}_n \Delta t \end{aligned} \tag{2.12}$$

The correction step is then:

$$\begin{aligned} \mathbf{r}_{n+1} &= \mathbf{r}_n + \frac{\Delta t}{2}(\mathbf{v}_n + \mathbf{v}^{\mathrm{p}}_{n+1}) \\ \mathbf{v}_{n+1} &= \mathbf{v}_n + \frac{\Delta t}{2}(\mathbf{a}_n + \mathbf{a}^{\mathrm{p}}_{n+1}) \end{aligned} \tag{2.13}$$

where $\mathbf{a}^{\mathrm{p}}_{n+1}$ is the acceleration calculated at the point ($\mathbf{r}^{\mathrm{p}}_{n+1}$,$\mathbf{v}^{\mathrm{p}}_{n+1}$). Applying the predictor-corrector approach the Euler's method modifies the numerical error to $\mathcal{O}(\Delta t^2)$, which means that this modified Euler approach is a second-order predictor-corrector scheme. Although this is an improvement on the simple Euler method, N-body simulations of stars in young stellar regions generally require at least fourth-order accuracy.

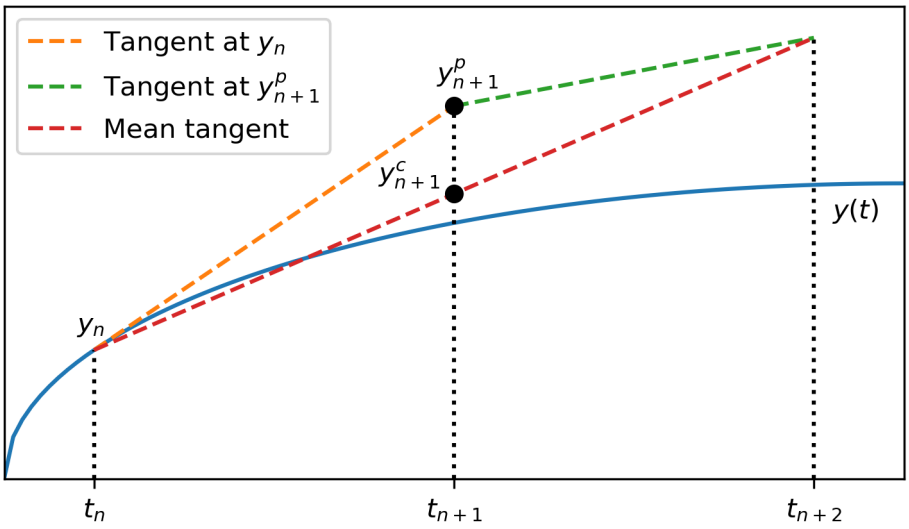

Figure 2.2: The modified Euler method of integrating an ordinary differential equation. A predicted value y^{p}_{n+1} is calculated using the tangent of $y(t)$ at the point (t_n, y_n). Then a corrected value y^{c}_{n+1} is found by taking the mean of the tangents of $y(t)$ at the points (t_n, y_n) and $(t_{n+1}, y^{\mathrm{p}}_{n+1})$, leading to a refined solution with an error $\mathcal{O}(\Delta t^2)$.

The rest of this chapter focuses on a widely used predictor-corrector scheme - the fourth-order Hermite scheme.

2.5 The Fourth-Order Hermite Method

The N-body integrator used for the investigations described within Chapters 4 and 5 is the time-symmetric fourth-order Hermite integrator KIRA, part of the Starlab package developed by Portegies Zwart et al. (2001). The N-body part of the hybrid N-body/SPH code GANDALF (Hubber et al., 2013) used for Chapter 6 is also a time-symmetric fourth-order Hermite scheme. Although the Hermite method was first described in Makino (1991), the time-symmetric version is introduced by Kokubo et al. (1998).

As with the modified Euler method, the fourth-order Hermite scheme is a predictor-corrector method. The equations for the predicted position $\mathbf{r}^{\rm p}_{i,n+1}$ and velocity $\mathbf{v}^{\rm p}_{i,n+1}$ of a particle i at time t_{n+1} are found by taking the Taylor series of the acceleration $\mathbf{a}_{i,n}$ and its first derivative $\dot{\mathbf{a}}_{i,n}$ given by Aarseth (2003)):

$$\dot{\mathbf{a}}_{i,n} = \sum_{j=1;\, j\neq i}^{N} m_j \left[\frac{\mathbf{v}_{ji}}{r_{ji}^3} - 3\frac{(\mathbf{r}_{ji}\cdot\mathbf{v}_{ji})\mathbf{r}_{ji}}{r_{ji}^5} \right] \tag{2.14}$$

The values of $\mathbf{r}^{\rm p}_{i,n+1}$ and $\mathbf{v}^{\rm p}_{i,n+1}$ are then given by:

$$\begin{aligned} \mathbf{r}^{\rm p}_{i,n+1} &= \mathbf{r}_{i,n} + \mathbf{v}_{i,n}(\Delta t) + \frac{\mathbf{a}_{i,n}}{2}(\Delta t^2) + \frac{\dot{\mathbf{a}}_{i,n}}{6}(\Delta t^3) \\ \mathbf{v}^{\rm p}_{i,n+1} &= \mathbf{v}_{i,n} + \mathbf{a}_{i,n}(\Delta t) + \frac{\dot{\mathbf{a}}_{i,n}}{2}(\Delta t^2) \end{aligned} \tag{2.15}$$

These predicted $\mathbf{r}^{\rm p}_{i,n+1}$ and $\mathbf{v}^{\rm p}_{i,n+1}$ can then be used to calculate a predicted $\mathbf{a}^{\rm p}_{i,n+1}$ and $\dot{\mathbf{a}}^{\rm p}_{i,n+1}$ at time t_{n+1}. The 'corrector' terms are found using Hermite interpolation of the acceleration and first derivative at t_n and the predicted acceleration and first derivative at t_{n+1}:

$$\begin{aligned} \mathbf{r}^{\rm c}_{i,n+1} &= \mathbf{r}^{\rm p}_{i,n+1} + \frac{\mathbf{a}^{(2)}_{i,n}}{24}(\Delta t^4) + \frac{\mathbf{a}^{(3)}_{i,n}}{120}(\Delta t^5) \\ \mathbf{v}^{\rm c}_{i,n+1} &= \mathbf{v}^{\rm p}_{i,n+1} + \frac{\mathbf{a}^{(2)}_{i,n}}{6}(\Delta t^3) + \frac{\mathbf{a}^{(3)}_{i,n}}{24}(\Delta t^4) \end{aligned} \tag{2.16}$$

where:

$$\begin{aligned} \mathbf{a}^{(2)}_{i,n} &= \frac{-6(\mathbf{a}_{i,n} - \mathbf{a}^{\rm p}_{i,n+1}) - \Delta t(4\dot{\mathbf{a}}_{i,n} + 2\dot{\mathbf{a}}^{\rm p}_{i,n+1})}{\Delta t^2} \\ \mathbf{a}^{(3)}_{i,n} &= \frac{12(\mathbf{a}_{i,n} - \mathbf{a}^{\rm p}_{i,n+1}) - 6\Delta t(\dot{\mathbf{a}}_{i,n} + \dot{\mathbf{a}}^{\rm p}_{i,n+1})}{\Delta t^3} \end{aligned} \tag{2.17}$$

The predictor and corrector steps together determine the positions and velocities for each particle i at the new time $t = t_{n+1}$. The correction step can be applied more than once for increased accuracy, which is why the Hermite scheme is also called a P(EC)^n

scheme, for 'Predict (Evaluate and Correct)^n' - the 'evaluate and correct' step is applied n times for every 'predict' step. However, in practice, the improvement in accuracy for each iteration of the 'evaluate and correct' step faces diminishing returns and n is typically set to no greater than 2.

Time symmetry in a N-body algorithm means that, if Equation 2.2 is solved, first forward in time and then backward in time, then the initial conditions can be recovered. Kokubo et al. (1998) were the first to show that the fourth-order Hermite scheme could be shown as time-symmetric when they formulated Equations 2.15–2.17 as:

$$\begin{aligned}
\mathbf{r}_{i,n+1} &= \mathbf{r}_{i,n} + \frac{1}{2}(\mathbf{v}_{i,n+1} + \mathbf{v}_{i,n})(\Delta t) - \frac{1}{10}(\mathbf{a}_{i,n+1} - \mathbf{a}_{i,n})(\Delta t^2) + \frac{1}{120}(\dot{\mathbf{a}}_{i,n+1} + \dot{\mathbf{a}}_{i,n})(\Delta t^3) \\
\mathbf{v}_{i,n+1} &= \mathbf{v}_{i,n} + \frac{1}{2}(\mathbf{a}_{i,n+1} + \mathbf{a}_{i,n})(\Delta t) - \frac{1}{10}(\dot{\mathbf{a}}_{i,n+1} + \dot{\mathbf{a}}_{i,n})(\Delta t^2)
\end{aligned} \tag{2.18}$$

In Equation 2.18 it is apparent that first solving forwards in time, before changing $\Delta t \rightarrow -\Delta t$ and $\mathbf{x}_{n+1} \rightarrow \mathbf{x}_{n-1}$ and solving again will recover the initial conditions.

In order to optimise the efficiency of the algorithm and to maintain the time-symmetric nature of Equation 2.18 individual, discretised timesteps Δt_i are used for each body in the simulation. The calculation of such timesteps is the topic of the next section.

2.6 Calculating the Timestep

Within a stellar region, there can be a wide range of densities, which correspond to a wide range of significant time scales. For example, the acceleration (and its derivatives) of a star in a gravitationally-bound triple system may change significantly over a period of a few hundred years, while the same parameters for an isolated star on the edge of a diffuse association may not undergo significant changes within a few Myr.

To preserve the accuracy of the numerical integration, the time interval Δt must be small enough to allow for the smallest significant time scales within a simulation. However, setting a global time interval with respect to the minimum significant timescale results in a large number of unnecessary computations of the negligible motion of the stars which have much larger significant timescales.

2.6.1 Individual Timesteps

One solution to this problem is to allocate an individual timestep Δt_i to each star i in the simulation. The size of each Δt_i will depend on the magnitude of the forces imposed on the respective particle, i - the faster particle i is accelerating, the smaller the time frame in which significant changes occur, so a smaller timestep Δt_i is necessary. Therefore, the allocation of individual timesteps preserves accuracy when predicting the motion of fast stars in dense regions, while decreasing computation time spent integrating the motion of slow objects in less dense environments.

The standard equation used for calculating the individual timestep Δt_i for each particle i is known as the Aarseth criterion (Aarseth, 1985):

$$\Delta t_i = \left(\frac{\eta |\mathbf{a}_i||\mathbf{a}_i^{(2)}| + |\dot{\mathbf{a}}_i|^2}{|\dot{\mathbf{a}}_i||\mathbf{a}_i^{(3)}| + |\mathbf{a}_i^{(2)}|^2} \right)^{\frac{1}{2}} \tag{2.19}$$

where η is a dimensionless accuracy parameter and $\dot{\mathbf{a}}_i$, $\mathbf{a}_i^{(2)}$ and $\mathbf{a}_i^{(3)}$ are the first, second and third derivatives of acceleration respectively (also called the 'jerk', 'snap', 'crackle'). When calculating the initial timestep at the beginning of a simulation, the following approximation is commonly used:

$$\Delta t_i = \frac{\eta |\mathbf{a}_i|}{|\dot{\mathbf{a}}_i|} \tag{2.20}$$

While the individual timestep scheme allows for the optimisation of the number of computations with respect to each body's individual significant time scale, it causes the algorithm to lose the ability to be time-reversed. Between a single, global timestep and individual continuous timesteps, there is an intermediate scheme which conserves time symmetry and allows for more than one body to be evolved simultaneously, which is the focus of the next section.

2.6.2 Block Timesteps

While the individual timestep scheme decreases the computation time of the integration without losing accuracy, in practise it is simpler to discretise the time steps using powers of 2, so that the motion of particles with similar dynamical properties are integrated at the same time.

Defining the maximum permitted time step of a body i as $\Delta t_{i,1}$, the smaller discretised

time steps are calculated as:

$$\Delta t_{i,\alpha} = \frac{\Delta t_{i,1}}{2^{\alpha-1}} \tag{2.21}$$

where α is an integer value ($\alpha \geq 1$) which defines the hierarchical level of the time step - as α increases by 1, $\Delta t_{i,\alpha}$ decreases by 1/2.

When calculating a new time step Δt_i for a particle i, Equation 2.19 is first used, then rounded to the nearest value found from Equation 2.21. Whether this value for Δt_i is accepted as the new time step depends on a comparison between it and the previous time step $\Delta t_{i,\text{prev}}$. As Equation 2.22 shows, if Δt_i is less than $\Delta t_{i,\text{prev}}$, then the new time step is half $\Delta t_{i,\text{prev}}$. However, if the Δt_i is greater than $\Delta t_{i,\text{prev}}$, then the new time step will only be double $\Delta t_{i,\text{prev}}$ if the particle time t_i is in sync with the new larger level.

$$\Delta t_{i,new} = \begin{cases} \Delta t_{i,\text{prev}}/2, & \text{if } \Delta t_i < \Delta t_{i,\text{prev}} \\ 2\Delta t_{i,\text{prev}}, & \text{if } \Delta t_i > \Delta t_{i,\text{prev}} \quad \text{and } t_i \bmod 2\Delta t_i = 0 \\ \Delta t_{i,\text{prev}}, & \text{otherwise} \end{cases} \tag{2.22}$$

.

For example, Figure 2.3 shows the three largest timestep levels $\alpha = 1, 2, 3$, which correspond to $\Delta t = \Delta t_1, \frac{1}{2}\Delta t_1, \frac{1}{4}\Delta t_1$. A particle timestep which corresponds to with $\alpha = 2$ can change become larger only at time t_4, when the $\alpha = 2$ level is synchronised with the $\alpha = 1$ level. Conversely, it can become smaller, changing to the $\alpha = 3$ level, on any of its steps as it is always synchronised (i.e. mod $2\Delta t_i = 0$). By the same token, a particle timestep which corresponds to with $\alpha = 3$ cannot become larger and transition to the $\alpha = 3$ at times t_1 or t_3 when the levels are not synchronised (mod $2\Delta t_i \neq 0$).

2.6.3 The Hermite Algorithm

The algorithm for performing fourth-order Hermite integration is as follows:

1. Set up the simulation:
   (a) Generate initial positions $\mathbf{r}$, velocities $\mathbf{v}$ and masses m for each particle in the simulation. This is explained in detail in Section 2.7 below.
   (b) Calculate the initial acceleration $\mathbf{a}$ and its first derivative $\dot{\mathbf{a}}$ for each particle.
   (c) Use $\mathbf{a}$ and $\dot{\mathbf{a}}$ with Equation 2.20 to calculate the initial timesteps Δt_i for each particle i, before discretising them using Equation 2.21.
2. Run the simulation:

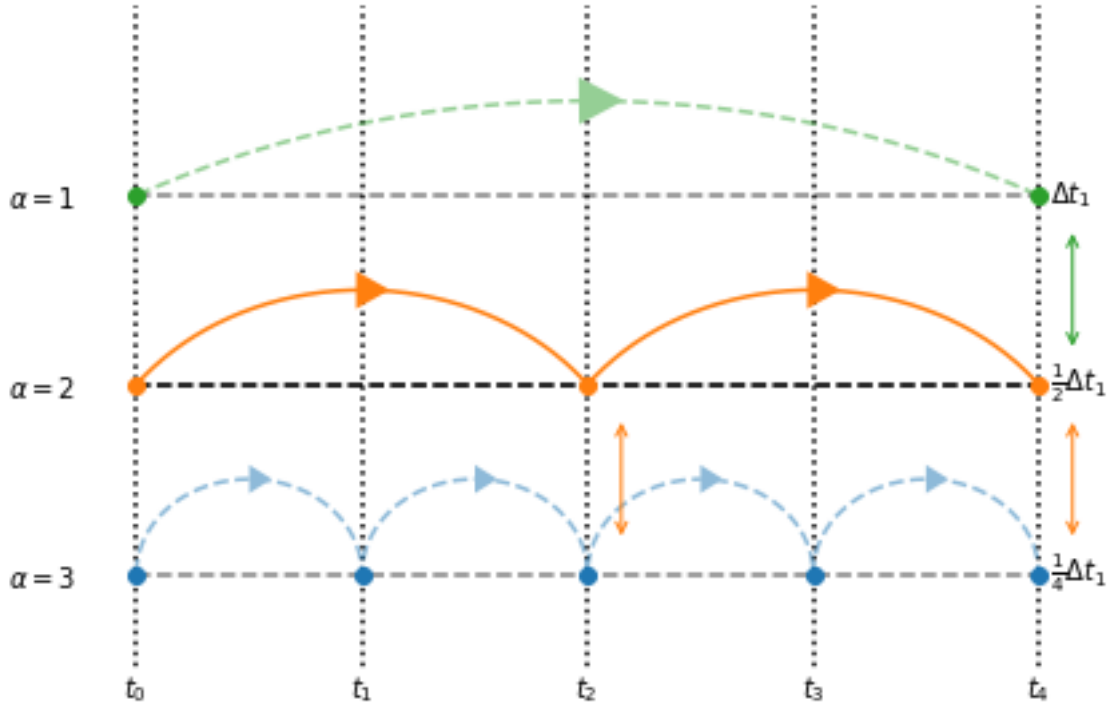

Figure 2.3: An illustration of how timesteps which are discretised can change levels according to Equation 2.22. At time t_2, A particle timestep corresponding to $\alpha = 2$ may drop to level $\alpha = 3$ but may not rise to level $\alpha = 1$, as levels $\alpha = 2$ and $\alpha = 1$ are not synchronised.

(a) Calculate $t_i + \Delta t_i$ for each particle and find the minimum value $t_{\rm min}$.

(b) Use Equation 2.15 with $\mathbf{r}_n$, $\mathbf{v}_n$, $\mathbf{a}_n$ and $\dot{\mathbf{a}}_n$ to predict $\mathbf{r}_{n+1}$ and $\mathbf{v}_{n+1}$ for all particles at $t = t_{\rm min}$.

(c) Select particle i for which $t_i + \Delta t_i = t_{\rm min}$:

i. Calculate $\mathbf{a}_{i,n+1}$ and $\dot{\mathbf{a}}_{i,n+1}$ for particle i using $\mathbf{r}_{i,n+1}$ and $\mathbf{v}_{i,n+1}$.

ii. Calculate $\mathbf{a}^{(2)}_{i,n}$ and $\mathbf{a}^{(3)}_{i,n}$ using Equation 2.17.

iii. Use $\mathbf{a}^{(2)}_{i,n}$ and $\mathbf{a}^{(3)}_{i,n}$ to correct $\mathbf{r}_{i,n+1}$ and $\mathbf{v}_{i,n+1}$. Steps i. to iii. can be repeated n times for a P(EC)^n scheme.

iv. Calculate a new discretised timestep Δt_i for particle i using Equation 2.19.

v. Repeat steps i. to iv. for a new particle i for which $t_i + \Delta t_i = t_{\rm min}$.

Before the fourth-order Hermite scheme can be implemented, initial conditions are needed to give Hermite scheme something to integrate. The next section focuses on the generation of initial conditions which can be used to model real stellar systems.

2.7 Generating Initial Conditions

N-body simulations are a tool for predicting the future properties of a group of stars from their initial properties. A simulation's predictive power relies on good initial conditions. If the initial properties which are used as input to a simulation are too unrealistic, then the output of the simulation may not contain any useful predictions about the behaviour of the real world (On the other hand, completely realistic initial conditions are not possible, highlighting the importance of interpreting the results of simulations in the context of the assumptions made in their initial conditions).

On the other hand, one of the strengths of N-body schemes is the ability to take generalised, simplified models of observed stellar groups and run hundreds of simulations with randomised initial stellar masses, positions and velocities, allowing us to ask specific questions about the general evolution of stellar region while including the effect of stochasticity. This section deals with some of the methods for generating initial conditions which are used extensively in the investigations in Chapters 4, 5 and 6.

2.7.1 Virial Ratio

As shown in Section 1.3.2, the virial ratio $Q_{\rm vir}$ of a region is crucial to determining its dynamical state. As $Q_{\rm vir} \propto \sigma$ where σ is the velocity dispersion of stars in the region, it is

possible to use a chosen value of Q_{vir} to scale the velocities of stars in a simulated region. In this way, we can choose whether a group of stars is initially collapsing ($Q_{\text{vir}} < 0.5$), is expanding ($Q_{\text{vir}} > 0.5$) or is in a quasi-stable state ($Q_{\text{vir}} = 0.5$).

For example, if a simulation required that a spherically-symmetric group of stars (such as a Plummer distribution - see Section 2.7.4) was neither expanding nor contracting and hence had a global virial ratio $Q_{\text{vir}} = 0.5$, then the individual velocities of the stars in the distribution are found by first following the algorithm in section 2.7.4, then setting the virial ratio as equal to 0.5 and finally using the virial ratio to appropriately scale the individual stellar velocities.

2.7.2 N-body Units

Astrophysics deals with large numbers, which are unwieldy to use in numerical simulations. In order to simplify the calculations in N-body simulations, N-body units are used. First introduced by Henon (1971), the units are scaled so that $G = M = R_{\text{V}} = 1$, where M is the total mass of the region and R_{V} is the virial radius. The stellar masses and positions can then be scaled with respect to M and R_{V}. The scalars for the velocities and timesteps of the individual stars are calculated using the equation for the virial velocity (Equation 1.21) and the crossing time (Equation 1.24) respectively.

2.7.3 Mass Distribution

As explained in 1.3.1, the mass distribution of a group of stars is described by the initial mass function (IMF). As the IMF is assumed to be universal and has a shape given by the theoretical models shown in Figure 1.4, allocating the mass of the stars in an N-body simulation is done using one of the theoretical models.

Maschberger (2013) provides a simple and straightforward method of allocating stellar masses according to the Maschberger IMF, via random sampling of the probability density function. This gives rise to the function:

$$m(X) = \left([X(G(m_u) - G(m_l)) + G(m_l)]^{\frac{1}{1-\beta}} \right)^{\frac{1}{1-\alpha}} \tag{2.23}$$

where m_u and m_l are the upper and lower mass limits of the distribution, X is a random number generated from a uniform distribution between 0 and 1, and $G(m)$ is given by:

$$G(m) = \left(1 + \left(\frac{m}{0.2} \right)^{1-\alpha} \right)^{1-\beta} \tag{2.24}$$

This mass function is used in Chapters 4, 5 and 6 to give realistic initial masses to the stars in the simulated regions.

2.7.4 The Plummer Distribution

The distribution of positions of stars in stellar region in the Galaxy varies widely, between centrally-concentrated, spherically-symmetric regions to widely-dispersed, filamentary structures. Therefore, the challenge becomes to create a variety of numerical models which can be taken as useful depictions of these varied stellar regions.

Plummer (1911) created a density law to approximate the distribution of stars in globular clusters, and which is now used to generate initial positions and velocities of N-body particles in a centrally-concentrated spherical region. The Plummer density ρ of such a region with total mass M as a function of the distance from the centre r is given by:

$$\rho(r) = \left(\frac{3M}{4\pi a^3}\right)\left(1 + \frac{r^2}{a^2}\right)^{-5/2} \tag{2.25}$$

where a is the Plummer radius and $a \approx 1.3R_{0.5}$ where $R_{0.5}$ is the half-mass radius.

The recipe for the generation of initial position and velocity distributions of a group of stars with total mass M and radius R is outlined in Aarseth et al. (1974). Seven random numbers are generated by random sampling of a uniform distribution between 0 and 1. We label these X_1 to X_7. For simplicity we proceed in N-body units ($G = 1$; $M = 1$; $R = 1$):

1. For a group of stars with equal mass, the total mass within a sphere with radius r is:
$$M(r) = r^3(1 + r^2)^{-\frac{3}{2}} \tag{2.26}$$

2. The first random number X_1 is equated to $M(r)$, so that rearranging 2.26 gives:
$$r = (X_1^{-\frac{2}{3}} - 1)^{-\frac{1}{2}} \tag{2.27}$$

3. The radial distance from the centre given by Equation 2.27 is converted into a Cartesian position using random numbers X_2 and X_3:
$$\begin{aligned} z &= (1 - 2X_2)r \\ x &= (r^2 - z^2)^{\frac{1}{2}} \cos 2\pi X_3 \\ y &= (r^2 - z^2)^{\frac{1}{2}} \sin 2\pi X_3 \end{aligned} \tag{2.28}$$

4. With the random stellar position generated, the velocity is next. The escape velocity of the distribution is given by:

$$v_{\rm esc} = 2^{\frac{1}{2}}(1+r^2)^{-\frac{1}{4}} \tag{2.29}$$

Taking $q = v/v_{\rm esc}$ as the velocity as a fraction of the escape velocity means that the probability distribution of q can be written as:

$$g(q) = q^2(1-q^2)^{\frac{7}{2}} \tag{2.30}$$

As q is random between 0 and 1 and $g(q)$ will always be less than $0.1q$, we can use rejection sampling to find allowed values of q and $g(q)$. This is achieved with the normalised random numbers X_4 and X_5 and the inequality:

$$X_4^2(1-X_4^2)^{\frac{7}{2}} > 0.1X_5 \tag{2.31}$$

If the values of X_4 and X_5 do not satisfy this inequality then they are rejected and new values are generated until they do. Once the values of X_4 and X_5 satisfy Equation 2.31, the magnitude of the velocity is given by $v_r = X_4 v_{\rm esc}$.

5. The Cartesian components of velocity are then generated in the same way as the position components i.e.:

$$\begin{aligned} v_z &= (1-2X_6)v_r \\ v_x &= (v_r^2 - v_z^2)^{\frac{1}{2}} \cos 2\pi X_7 \\ v_y &= (v_r^2 - v_z^2)^{\frac{1}{2}} \sin 2\pi X_7 \end{aligned} \tag{2.32}$$

2.7.5 Fractal Distributions

The Plummer model is useful for simulations in which a stellar environment can be approximated as spherically symmetric with a smooth radial density profile. In reality, many observed young stellar regions are aspherical and contain clumpy structures (see Section 1.3). The fractal method introduced by Goodwin & Whitworth (2004) allows the generation of stellar positions and velocities which can be used as approximate models of observed, substructure stellar regions. The algorithm for doing so is as follows:

1. The (initially empty) stellar region is modelled as a cube, which is then divided into 8 equally-sized cubic subregions. The subregions are denoted the 'children' to

the region's 'parent'.

2. For each of the 8 children, the probability that it will become a parent is:

$$P(\text{parent}) = 2^{D-3} \tag{2.33}$$

where D is the fractal dimension and $D \leq 3$.

3. The parent is discarded and the children which *do not* become parents are also discarded. The positions of children which *do* become parents have noise added to break up any regularity. These children are then divided in turn into 8 subregion, which then become new children.

4. Steps 2 and 3 are repeated recursively, until the cubic region is heavily populated. To remove the cubic structure, children outside a radius r from the centre are discarded. Remaining children are then randomly discarded until N children are left, at which point the N stars to be simulated are placed at the centre of each remaining child.

5. The stellar velocities are generated in one of two ways. For an 'incoherent' velocity structure, the velocities are generated via random sampling of a Gaussian distribution, before being scaled according to the chosen virial ratio of the system. For a 'coherent' velocity structure, each child is first given the velocity of its parent to which an additional random velocity is added. This is done recursively down to the final children and finally to the stars to be simulated. This method gives a 'coherent' velocity structure because it means that stars which are close to each other have similar velocities compared to stars which are on opposite side of a region.

2.8 Summary

In this chapter, the fundamentals of N-body simulations and predictor-corrector methods were discussed, before the algorithm used for the investigations in Chapters 4 and 5, fourth-order Hermite scheme, is introduced. The practical considerations of choosing a timestep and generating useful initial conditions, which allow practical use of the Hermite algorithm for simulating the dynamics of a stellar region, are then discussed.

However, while the fourth-order Hermite scheme is widely used for simulating the dynamics of stellar regions, further methods are necessary to deal with the dynamics

of interstellar gas within a region. Numerical simulations which take into account the behaviour of gas in a region are the focus of the next chapter.

Chapter 3

Smoothed-Particle Hydrodynamics

3.1 Introduction

Smoothed particle hydrodynamics (SPH) is a computational method for modelling the dynamical evolution of fluids. Originally formulated for use in astrophysics by Lucy (1977) and separately by Gingold & Monaghan (1977), it is now widely used in computational physics, from models of star and planet formation to models of hydroelectric power.

As gas can make up the majority of the mass of young stellar regions, (see Section 1.3.7), its presence and properties can have a profound effect on how the region will dynamically evolve. Therefore, the ability to accurately model the behaviour of the gas in these regions is crucial to understanding the evolutionary paths of young stellar regions in the Galaxy.

Hydrodynamics is the physics of how fluids (which can have a variety of initial dynamical properties) move within their environments, but SPH is not the only computational method for modelling fluids. Fluid dynamics models typically fit into one of two categories - Eulerian methods and Lagrangian methods. Eulerian methods model the dynamics of a fluid relative to a mesh of fixed points. The properties of the fluid are measured at these points, analogous to measuring the changing temperature of water flowing through a pipe by installing a thermometer at a fixed position in the pipe.

On the other hand, Lagrangian methods are mesh-free. Instead, they describe the dynamics of a fluid via the properties of freely-moving fluid 'particles', for which the equations of motion are derived. SPH is an example of a Lagrangian method as it uses the motion of SPH particles distributed throughout the fluid to model fluid flow.

The use of SPH has several advantages. It is Galilean invariant (meaning that the

laws of motion are the same in all inertial frames), easily conserves momentum and energy and couples intuitively with self-gravity, making it very useful in astrophysical situations where gravitational effects are significant and making it easy to combine SPH and N-body methods such as those used in Chapter 6.

In this chapter, the standard formalism of SPH is introduced, with the introduction of the smoothing kernel and the derivation of the equation of motion and the energy equation. Then, the widely-used variational *grad-h* method is described. The next section introduces the rest of the necessary components for SPH - self-gravity, artificial viscosity and the equation of state. Finally, I describe how SPH is implemented, via time integration, choice of timestep, the tree algorithm and how these fit into the hybrid SPH/N-body code GANDALF.

The aim of SPH is to numerically solve the equations of fluid dynamics which describe the conservation of linear momentum, energy and mass, respectively known as the momentum equation, the energy equation and the continuity equation. The Lagrangian form of the momentum equation is:

$$\frac{\mathrm{d}\mathbf{v}}{\mathrm{d}t} = -\frac{\nabla P}{\rho} + \mathbf{F}, \tag{3.1}$$

where $\mathbf{v}$ is the velocity, P is the pressure, ρ is the density and $\mathbf{F}$ is non-pressure forces such as gravity, which is necessary for SPH in young stellar regions (see Section 3.3.3). The energy equation is given by:

$$\frac{\mathrm{d}u}{\mathrm{d}t} = -\left(\frac{P}{\rho}\right)\nabla \cdot \mathbf{v} \tag{3.2}$$

and the continuity equation is given by:

$$\nabla \cdot \mathbf{v} = \frac{1}{\rho}\frac{\mathrm{d}\rho}{\mathrm{d}t}. \tag{3.3}$$

Finally, an equation of state is needed to link P and ρ to the gas temperature T. If the gas is assumed to be ideal, then:

$$P = \frac{k_{\mathrm{B}}\rho T}{\bar{m}} \tag{3.4}$$

where $\bar{m}$ is the mean gas particle mass.

3.2 First Steps in SPH

As SPH is a Lagrangian method, it models the gas in a stellar region using SPH particles which are distributed throughout the volume of the gas. Similar to N-body particles, each SPH particle i has a mass m_i, position $\mathbf{r}_i$ and velocity $\mathbf{v}_i$. Unlike N-body particles, each SPH particle i also carries properties of the fluid it is a part of such as density ρ_i, pressure P_i and internal energy u_i. The properties of these SPH particles (hereafter just called particles unless there is a possibility of getting them confused with N-body particles) are then used to sample the properties of the fluid they are tracing.

The standard formalism of SPH was introduced by Lucy (1977) and Gingold & Monaghan (1977) and further developed by Gingold & Monaghan (1982) and Monaghan (1985). It is also comprehensively explained in review articles Monaghan (1992), Monaghan (2005) and Springel (2010).

SPH takes any fluid property (density ρ, for example) as a function of position $A(\mathbf{r})$ given in three dimensions as:

$$A(\mathbf{r}) = \int A(\mathbf{r}')W(\mathbf{r}-\mathbf{r}',h)d\mathbf{r}'^3 \tag{3.5}$$

where $W(\mathbf{r}-\mathbf{r}',h)$ is the 'smoothing kernel' and stipulates how the properties of an SPH particle dissipate as a function of the position $\mathbf{r}$ and the so-called 'smoothing length' h. While Equation 3.5 is accurate for a continuum where the number of SPH particles $N \to \infty$, the discretised version is used as an approximation in order to model a finite number of SPH particles with positions $\mathbf{r}_i$, mass m_i and density ρ_i:

$$A(\mathbf{r}) \simeq \sum_{i=1}^{N} \left(\frac{m_i}{\rho_i}\right) A(\mathbf{r}_i)W(\mathbf{r}-\mathbf{r}_i,h) \tag{3.6}$$

The higher the value of N, the closer the result of Equation 3.6 will match the result of Equation 3.5.

If we take A_i to be the value of $A(\mathbf{r})$ at the position of SPH particle i and A_j to be the value of $A(\mathbf{r})$ at the position of particle j, then the function for finding a fluid property at the position of particle i is :

$$A_i \simeq \sum_{j=1}^{N} \frac{m_j}{\rho_j} A_j W_{ij} \tag{3.7}$$

where $W_{ij} = W(\mathbf{r}_i-\mathbf{r}_j,h)$. As a simple example, measuring the density ρ_i at the position

of particle i yields:

$$\rho_i \simeq \sum_{j=1}^{N} m_j W_{ij} \tag{3.8}$$

3.2.1 The Smoothing Kernel

The smoothing kernel $W(\mathbf{r}-\mathbf{r}', h)$ allows the influence of each SPH particle at a certain position $\mathbf{r}$ to dissipate as the particle gets further away from that position. Gingold & Monaghan (1977) first introduced the following Gaussian to use as the smoothing kernel (in three dimensions):

$$W(\mathbf{r}-\mathbf{r}', h) = \frac{1}{\pi^{3/2}h^3} \exp\left[-\frac{(\mathbf{r}-\mathbf{r}')^2}{h}\right]. \tag{3.9}$$

This formulation of the smoothing kernel has several properties which are required for any smoothing kernel (stipulated in Gingold & Monaghan (1977) and Gingold & Monaghan (1982)):

- The smoothing function is normalisable over all space, i.e.:

$$\int_0^\infty W(\mathbf{r}-\mathbf{r}', h) d\mathbf{r}' = 1 \tag{3.10}$$

- The smoothing function is an even function, i.e.:

$$W(\mathbf{r}-\mathbf{r}', h) = W(|\mathbf{r}-\mathbf{r}'|, h) \tag{3.11}$$

- As the smoothing length h gets smaller, the smoothing function more and more resembles a delta function, i.e.:

$$\lim_{h\to 0} W(\mathbf{r}-\mathbf{r}', h) = \delta(\mathbf{r}-\mathbf{r}') \tag{3.12}$$

- It is smooth to at least the second derivative in order to prevent large fluctuations in the force felt by an individual SPH particle.

However, the fact that Equation 3.9 requires contributions from even the most distant SPH particles (whose influence may be insignificant) has driven the widespread preference of other formulations in which the smoothing kernel is set to 0 for distances beyond a set threshold.

One such formulation, which is also the formulation used for the investigations in Chapter 6, is the M4 cubic spline (Monaghan & Lattanzio, 1985) which sets $W(\mathbf{r}-\mathbf{r}', h)$ to zero when $|\mathbf{r}-\mathbf{r}'| > 2h$ with a marginal error from doing so, and has a continuous second derivative. It is given by:

$$W(r,h) = \frac{1}{\pi h^3} \begin{cases} 1 - \frac{3}{2}\left(\frac{r}{h}\right)^2 + \frac{3}{4}\left(\frac{r}{h}\right)^3 & \text{for } 0 \leq \frac{r}{h} < 1 \\ \frac{1}{4}\left(2 - \frac{r}{h}\right)^3 & \text{for } 1 \leq \frac{r}{h} < 2\,, \\ 0 & \text{for } \frac{r}{h} \geq 2 \end{cases} \tag{3.13}$$

where $r = |\mathbf{r}-\mathbf{r}'|$. For the derivations of the equation of motion and the energy equation, the spatial derivative ∇W and the derivative with respect to smoothing length $\frac{\partial W(r,h)}{\partial h}$ is needed. The former is given by:

$$\nabla W(r,h) = -\frac{\hat{\mathbf{r}}}{\pi h^4} \begin{cases} 3\left(\frac{r}{h}\right) + \frac{9}{4}\left(\frac{r}{h}\right)^2 & \text{for } 0 \leq \frac{r}{h} < 1 \\ \frac{3}{4}\left(2 - \frac{r}{h}\right)^2 & \text{for } 1 \leq \frac{r}{h} < 2\,, \\ 0 & \text{for } \frac{r}{h} \geq 2 \end{cases} \tag{3.14}$$

and the latter is given by:

$$\frac{\partial W(r,h)}{\partial h} = \frac{\hat{\mathbf{r}}}{\pi h^4} \begin{cases} -3 + \frac{15}{2}\left(\frac{r}{h}\right)^2 - \frac{27}{4}\left(\frac{r}{h}\right)^3 & \text{for } 0 \leq \frac{r}{h} < 1 \\ -6 + 12\frac{r}{h} - \frac{15}{2}\left(\frac{r}{h}\right)^2 - \frac{27}{4}\left(\frac{r}{h}\right)^3 & \text{for } 1 \leq \frac{r}{h} < 2\,, \\ 0 & \text{for } \frac{r}{h} \geq 2 \end{cases} \tag{3.15}$$

3.2.2 The Momentum Equation

In order to use SPH for astrophysics simulations, it is necessary to know the force acting on each SPH particle and the change of energy on each particle. The former is found by deriving the equation of motion for an SPH particle.

The conservation of linear momentum, given by Equation 3.1 is, for a particle i with velocity $\mathbf{v}_i$:

$$\frac{d\mathbf{v}_i}{dt} = -\frac{\nabla P_i}{\rho_i}, \tag{3.16}$$

where the effect of gravitational force is set to zero - self-gravity will be added later for the full, variational form of the equation of motion.

The pressure term $\frac{\nabla P}{\rho}$ can be rewritten (via application of the vector calculus version

of the quotient rule) as:

$$\frac{\nabla P}{\rho} = \nabla\left(\frac{P}{\rho}\right) + \frac{P}{\rho^2}\nabla\rho \tag{3.17}$$

Substituting Equation 3.17 into Equation 3.7 gives the pressure component of the momentum equation for a particle i as:

$$\frac{\nabla P_i}{\rho_i} = \sum_{j=1}^{N} m_j \left(\frac{P_i}{\rho_i^2} + \frac{P_j}{{\rho_j}^2}\right)\nabla W_{ij} \tag{3.18}$$

Therefore the equation of motion for a particle i is given by:

$$\frac{d\mathbf{v}_i}{dt} = -\sum_{j=1}^{N} m_j \left(\frac{P_i}{\rho_i^2} + \frac{P_j}{{\rho_j}^2}\right)\nabla W_{ij} \tag{3.19}$$

where ∇W_{ij} is given by Equation 3.14.

3.2.3 The Thermal Energy Equation

In order to determine how the thermal energy u of an SPH particle will change over time, the fluid dynamics law for conservation of energy (Equation 3.2) is used. Its right-hand side can be rewritten (via use of the vector product rule and rearranging) as:

$$-\left(\frac{P}{\rho}\right)\nabla\cdot\mathbf{v} = \left(\frac{P}{\rho^2}\right)\left[\mathbf{v}\cdot\nabla\rho - \nabla\cdot(\rho\mathbf{v})\right] \tag{3.20}$$

Using expressions for the gradient and the divergence of Equation 3.7 finds the expression (for particle i) as:

$$\begin{aligned} -\left(\frac{P_i}{\rho_i}\right)\nabla\cdot\mathbf{v}_i &= \left(\frac{P_i}{\rho_i^2}\right)\left[\sum_{j=1}^{N} m_j\mathbf{v}_i\cdot\nabla_i W_{ij} - \sum_{j=1}^{N} m_j\mathbf{v}_j\cdot\nabla_i W_{ij}\right] \\ &= \sum_{j=1}^{N}\left(\frac{P_i}{\rho_i^2}\right)(\mathbf{v}_i - \mathbf{v}_j)\cdot\nabla_i W_{ij} \end{aligned} \tag{3.21}$$

However, the right-hand side of Equation 3.2 can be rewritten in a second way as:

$$-\left(\frac{P}{\rho}\right)\nabla\cdot\mathbf{v} = \mathbf{v}\cdot\nabla\left(\frac{P}{\rho}\right) - \nabla\cdot\left(\frac{P\mathbf{v}}{\rho}\right) \tag{3.22}$$

Again, using expressions for the gradient and the divergence of Equation 3.7 finds the expression (for particle i) as:

$$\begin{aligned} -\left(\frac{P_i}{\rho_i}\right)\nabla\cdot\mathbf{v}_i &= \left(\frac{P_j}{\rho_j^2}\right)\left[\sum_{j=1}^{N} m_j\mathbf{v}_i\cdot\nabla_i W_{ij} - \sum_{j=1}^{N} m_j\mathbf{v}_j\cdot\nabla_i W_{ij}\right] \\ &= \sum_{j=1}^{N}\left(\frac{P_j}{\rho_j^2}\right)(\mathbf{v}_i-\mathbf{v}_j)\cdot\nabla_i W_{ij} \end{aligned} \tag{3.23}$$

The energy equation that is typically used is the average of Equation 3.21 and Equation 3.23:

$$\frac{du_i}{dt} = \frac{1}{2}\sum_{j=1}^{N}\left(\frac{P_i}{\rho_i^2}+\frac{P_j}{\rho_j^2}\right)(\mathbf{v}_i-\mathbf{v}_j)\cdot\nabla_i W_{ij} \tag{3.24}$$

With equations for the time derivatives of position and energy of an SPH particle, it is possible to use time integration to predict the particle's future position and energy (similar to how time integration was performed for the N-body particles in Chapter 2). However, SPH schemes used to tackle a wide range of astrophysical scenarios are more sophisticated than the simple model outlined above. The most popular scheme is described in the next section.

3.3 Variational (*grad-h*) SPH

In the formulation of SPH described in Section 3.2 above, the smoothing length h is invariant with position and time. Although this may be adequate for simulated regions in which the density does not change significantly, problems arise when the density of the region varies over time and space. For areas of low density, the lack of proximity between neighbouring SPH particles means that a fixed value of h will cause inaccuracies in calculations. Conversely, for areas of very high density, a fixed value of h means much higher computation times than necessary, increasing the total simulation time. Similar to how a variable timestep alleviates similar issues in N-body simulations (see Section 2.6), a variable smoothing length, which takes into account the distribution of SPH particles as a function of position, helps to overcome these problems.

One way of implementing a variable smoothing length is by giving each SPH particle i an individual smoothing length h_i determined by half the distance between it and its 50th nearest neighbour - $h_i = |\mathbf{r}_i - \mathbf{r}_{50}|/2$. The problem with doing so, however, is that such a scheme does not conserve momentum when particles with different smoothing

lengths ($h_i \neq h_j$) interact. Attempts to overcome these problems include using a value which is the mean of the smoothing lengths h_i and h_j (Benz, 1990) or taking the mean of the two smoothing kernels $W_{ij}(h_i)$ and $W_{ij}(h_j)$ (Hernquist & Katz, 1989), but such attempts have not succeeded in conserving both momentum and energy (Hernquist, 1993). The *grad-h* scheme first formulated by Springel & Hernquist (2002), solves these problems.

In the *grad-h* formulation of SPH, the variable, individual particle smoothing length h_i is given in terms of its density mass m_i and density ρ_i as:

$$h_i = \eta \left(\frac{m_i}{\rho_i} \right)^{1/3}, \tag{3.25}$$

where η is an accuracy parameter. The density is given by:

$$\rho_i = \sum_{j=1}^{N} m_j W(r_{ij}, h_i) \tag{3.26}$$

As h_i is a function of ρ_i, and ρ_i is a function of h_i, the value of h_i can only be found via iteration.

Eckart (1960) showed that the Euler equations for an ideal gas come from the Lagrangian:

$$\mathcal{L} = \int \rho \left(\frac{\mathbf{v}^2}{2} - u \right) dV, \tag{3.27}$$

where ρ is the density, $\mathbf{v}$ is velocity, V is the volume of the gas and u is the specific internal energy. Discretising the Lagrangian for use in SPH yields:

$$\mathcal{L} = \sum_{j=1}^{N} \left(m_j \frac{\mathbf{v}_j^2}{2} - m_j u_j \right) \tag{3.28}$$

The specific internal energy of a particle u_j is defined in terms of the density ρ_j, the adiabatic index γ and the function for its specific entropy A_j as:

$$u_j(\rho_j) = A_j \frac{\rho_j^{\gamma-1}}{\gamma - 1} \tag{3.29}$$

Using these equations to solve the Euler-Lagrange equation, we can then find the full, variational equations of motion and of thermal energy.

3.3.1 Equation of Motion

The derivation of the *grad-h* form of the equation of motion for SPH particles begins with the Euler-Lagrange equation:

$$\frac{d}{dt}\left(\frac{\partial \mathcal{L}}{\partial \mathbf{v}_i}\right) - \frac{\partial \mathcal{L}}{\partial \mathbf{r}_i} = 0, \tag{3.30}$$

where $\mathcal{L}$ is given by Equation 3.28. The first term of Equation 3.30 is therefore:

$$\begin{aligned}\frac{d}{dt}\left(\frac{\partial \mathcal{L}}{\partial \mathbf{v}_i}\right) &= \frac{d}{dt}\left[\frac{\partial}{\partial \mathbf{v}_i}\sum_{j=1}^{N} m_j\left(\frac{\mathbf{v}_j^2}{2} - u_j\right)\right] \\ &= \frac{d}{dt}\left(m_i \frac{\partial}{\partial \mathbf{v}_i}\left(\frac{\mathbf{v}_i^2}{2}\right)\right) \\ &= m_i \frac{d\mathbf{v}_i}{dt}\end{aligned} \tag{3.31}$$

Putting this result back into Equation 3.30 yields:

$$\begin{aligned}m_i \frac{d\mathbf{v}_i}{dt} &= \frac{\partial \mathcal{L}}{\partial \mathbf{r}_i} \\ &= \frac{\partial}{\partial \mathbf{r}_i}\left[\sum_{j=1}^{N} m_j\left(\frac{\mathbf{v}_j^2}{2} - u_j\right)\right] \\ &= -\sum_{j=1}^{N} m_j \frac{\partial u_j}{\partial \mathbf{r}_i} \\ &= -\sum_{j=1}^{N} m_j \frac{\partial u_j}{\partial \rho_j}\frac{\partial \rho_j}{\partial \mathbf{r}_i}\end{aligned} \tag{3.32}$$

The variation of u_j with respect to ρ_j in Equation 3.32 is found by invoking the derivative of the first law of thermodynamics when the total entropy S is constant (i.e. $dS = 0$):

$$dU = -PdV = \frac{mP}{\rho^2}d\rho, \tag{3.33}$$

where $\rho = \frac{m}{V}$ and U is the total energy. The change in energy per unit mass u_j as a function of density ρ_j is therefore:

$$\frac{\partial u_j}{\partial \rho_j} = \frac{P_j}{\rho_j^2}. \tag{3.34}$$

The change of ρ_j with respect to the position $\mathbf{r}_i$ in Equation 3.32 can be found for an arbitrary particle k as follows. Using Equation 3.26 (with indices j and k rather than i and j), $\frac{\partial \rho_j}{\partial \mathbf{r}_i}$ can be rewritten as:

$$\frac{\partial \rho_j}{\partial \mathbf{r}_i} = \frac{\partial}{\partial \mathbf{r}_i} \sum_{k=1}^{N} m_k W_{jk}(h_j) \tag{3.35}$$

From now on, the notation ∇_i is used to mean the partial derivative $\frac{\partial}{\partial \mathbf{r}_i}$ when the smoothing length h is kept constant. With this notation, Equation 3.35 becomes:

$$\frac{\partial \rho_j}{\partial \mathbf{r}_i} = \sum_{k=1}^{N} m_k \nabla_i W_{jk}(h_j) + \sum_{k=1}^{N} m_k \frac{\partial W_{jk}(h_j)}{\partial h_j} \frac{\partial h_j}{\partial \rho_j} \frac{\partial \rho_j}{\partial \mathbf{r}_i} \tag{3.36}$$

Rearranging gives:

$$\begin{aligned} \frac{\partial \rho_j}{\partial \mathbf{r}_i} &= \left[1 - \sum_{k=1}^{N} m_k \frac{\partial W_{jk}(h_j)}{\partial h_j} \frac{\partial h_j}{\partial \rho_j} \right]^{-1} \sum_{k=1}^{N} m_k \nabla_i W_{jk}(h_j) \\ &= \Omega_j^{-1} \sum_{k=1}^{N} m_k \nabla_i W_{jk}(h_j), \end{aligned} \tag{3.37}$$

where:

$$\Omega_j = 1 - \sum_{k=1}^{N} m_k \frac{\partial W_{jk}(h_j)}{\partial h_j} \frac{\partial h_j}{\partial \rho_j} \tag{3.38}$$

Here we can use the relation $\nabla_i W_{jk} = \nabla_j W_{jk}(\delta_{ji} - \delta_{ki})$ where δ is the Kronecker delta. Hence Equation 3.37 becomes:

$$\frac{\partial \rho_j}{\partial \mathbf{r}_i} = \Omega_j^{-1} \sum_{k=1}^{N} m_k \nabla_j W_{jk}(h_j)(\delta_{ji} - \delta_{ki}). \tag{3.39}$$

Putting Equations 3.34 and 3.39 back into Equation 3.32 yields:

$$\begin{aligned} m_i \frac{d\mathbf{v}_i}{dt} &= -\sum_{j=1}^{N} m_j \frac{P_j}{\rho_j^2} \Omega_j^{-1} \sum_{k=1}^{N} m_k \nabla_j W_{jk}(h_j)(\delta_{ji} - \delta_{ki}) \\ &= -m_i \frac{P_i}{\rho_i^2} \Omega_i^{-1} \sum_{k=1}^{N} m_k \nabla_i W_{ik}(h_i) + \sum_{j=1}^{N} m_j \frac{P_j}{\rho_j^2} \Omega_j^{-1} m_i \nabla_j W_{ji}(h_j) \\ &= -m_i \frac{P_i}{\rho_i^2} \Omega_i^{-1} \sum_{j=1}^{N} m_j \nabla_i W_{ij}(h_i) - \sum_{j=1}^{N} m_j \frac{P_j}{\rho_j^2} \Omega_j^{-1} m_i \nabla_i W_{ij}(h_j) \end{aligned} \tag{3.40}$$

In the last step, the index k has been replaced by the index j as they are summed over the same range. The equation of motion is then given by:

$$\frac{d\mathbf{v}_i}{dt} = -\sum_{j=1}^{N} m_j \left[\frac{P_i}{\Omega_i \rho_i^2} \nabla_i W_{ij}(h_i) + \frac{P_j}{\Omega_j \rho_j^2} \nabla_j W_{ij}(h_j) \right] \tag{3.41}$$

3.3.2 The Energy Equation

The derivation of variational version of the equation of energy is straightforward and begins with the continuity equation, given by Equation 3.3. Using this equation with the equation for the conservation of thermal energy (Equation 3.2) yields:

$$\frac{du_i}{dt} = -\frac{P_i}{\rho_i^2} \frac{d\rho_i}{dt} \tag{3.42}$$

Finding the variation of ρ_i with respect for time proceeds in an analogous way to the derivation of its variation with respect to position, from Equation 3.35 to Equation 3.38. It gives the variational form of the energy equation as:

$$\frac{du_i}{dt} = \frac{P_i}{\Omega_i \rho_i^2} \sum_{j=1}^{N} m_j \mathbf{v}_{ij} \cdot \nabla_i W_{ij}(h_i) \tag{3.43}$$

3.3.3 Self-Gravity

As explained in Chapter 1, the contribution of the gas in a young stellar region to the region's total mass can be significant. The dynamics of the gas will also be a result of its gravitational interactions with nearby stars and of gravitational interactions with itself. Therefore it is necessary to add a gravitational term to the equation of motion derived above in order to accurately describe gravitational interactions. One advantage of SPH

is that it is more friendly to implementations of gravity than mesh-based schemes - in mesh-based schemes, it is harder to add gravity and still maintain conservation of energy, whereas it is straightforward to do it accurately in SPH.

Price & Monaghan (2007) first introduced a gravitational term $\Phi(\mathbf{r})$ which describes the gravitational field at the position of particle j ($\mathbf{r}_j$) due to SPH particles k as:

$$\begin{aligned}\Phi(\mathbf{r}_j) &= G\sum_{k=1}^{N} m_k \phi(\mathbf{r}_j - \mathbf{r}_k, h_j) \\ &= G\sum_{k=1}^{N} m_k \phi_{jk}(h_j),\end{aligned} \tag{3.44}$$

where $\phi_{jk}(h_j)$ is the *gravitational* smoothing kernel. The total gravitational potential energy of the system of SPH particles is defined as:

$$\begin{aligned}E_{\text{grav}} &= \frac{1}{2}\sum_{j=1}^{N} m_j \Phi(\mathbf{r}_j) \\ &= \frac{G}{2}\sum_{j=1}^{N} m_j \sum_{k=1}^{N} m_k \phi_{jk}(h_j)\end{aligned} \tag{3.45}$$

Adding this term into Equation 3.28, the full discretised Lagrangian with gravity added becomes:

$$\begin{aligned}\mathcal{L}_{\text{SPH}} &= \sum_{j=1}^{N}\left(m_j\frac{\mathbf{v}_j^2}{2} - m_j u_j\right) - \frac{G}{2}\sum_{j=1}^{N} m_j \sum_{k=1}^{N} m_k \phi_{jk}(h_j) \\ &= \mathcal{L}_{\text{pres}} + \mathcal{L}_{\text{grav}},\end{aligned} \tag{3.46}$$

where $\mathcal{L}_{\text{pres}}$ and $\mathcal{L}_{\text{grav}}$ refer to the pressure and gravity contributions to the Lagrangian respectively.

Putting Equation 3.46 into the Euler-Lagrange Equation (Equation 3.30) yields an additional term for the acceleration due to gravity:

$$\begin{aligned}m_i\left(\frac{d\mathbf{v}_i}{dt}\right)_{\text{grav}} &= -\frac{\partial}{\partial \mathbf{r}_i}\left[\frac{G}{2}\sum_{j=1}^{N} m_j \sum_{k=1}^{N} m_k \phi_{jk}(h_j)\right] \\ &= -\frac{G}{2}\sum_{j=1}^{N} m_j \sum_{k=1}^{N} m_k \frac{\partial \phi_{jk}(h_j)}{\partial h_j}\frac{\partial h_j}{\partial \mathbf{r}_i}\end{aligned} \tag{3.47}$$

Analogous to Equation 3.36, ∇_i is introduced as the partial derivative $\frac{\partial}{\partial \mathbf{r}_i}$ when the smoothing length h is kept constant. Hence:

$$\begin{aligned} m_i \left(\frac{d\mathbf{v}_i}{dt}\right)_{\text{grav}} = &- \frac{G}{2}\sum_{j=1}^{N}\sum_{k=1}^{N} m_j m_k \nabla_i \phi_{jk}(h_j) \\ &- \frac{G}{2}\sum_{j=1}^{N}\sum_{k=1}^{N} m_j m_k \frac{\partial \phi_{jk}(h_j)}{\partial h_j}\frac{\partial h_j}{\partial \rho_j}\frac{\partial \rho_j}{\partial \mathbf{r}_i} \end{aligned} \tag{3.48}$$

As with Equation 3.39, here we simplify the first term by using the relation $\nabla_i \phi_{jk} = \nabla_j \phi_{jk}(\delta_{ji} - \delta_{ki})$ where δ is the Kronecker delta to give:

$$\begin{aligned} -\frac{G}{2}\sum_{j=1}^{N}\sum_{k=1}^{N} m_j m_k \nabla_i \phi_{jk}(h_j) &= -\frac{G}{2}\sum_{j=1}^{N}\sum_{k=1}^{N} m_j m_k \nabla_j \phi_{jk}(h_j)(\delta_{ji} - \delta_{ki}) \\ &= -\frac{G m_i}{2}\left[\sum_{k=1}^{N} m_k \nabla_i \phi_{ik}(h_i) - \sum_{j=1}^{N} m_j \nabla_j \phi_{ji}(h_j)\right] \\ &= -\frac{G m_i}{2}\sum_{j=1}^{N} m_j \left(\nabla_i \phi_{ij}(h_i) + \nabla_i \phi_{ij}(h_j)\right) \end{aligned} \tag{3.49}$$

For the second term in Equation 3.48, the expression for $\frac{\partial \rho_j}{\partial \mathbf{r}_i}$ in Equation 3.39 (for an arbitrary particle l is used to give:

$$\begin{aligned} &- \frac{G}{2}\sum_{j=1}^{N}\sum_{k=1}^{N} m_j m_k \frac{\partial \phi_{jk}(h_j)}{\partial h_j}\frac{\partial h_j}{\partial \rho_j}\frac{\partial \rho_j}{\partial \mathbf{r}_i} \\ &= -\frac{G}{2}\sum_{j=1}^{N}\sum_{k=1}^{N} m_j m_k \frac{\partial \phi_{jk}(h_j)}{\partial h_j}\frac{\partial h_j}{\partial \rho_j}\Omega_j^{-1}\sum_{l=1}^{N} m_l \nabla_j W_{jl}(h_j)(\delta_{ji} - \delta_{li}) \\ &= -\frac{G}{2}\left[m_i \sum_{k=1}^{N} m_k \frac{\partial \phi_{ik}(h_i)}{\partial h_i}\frac{\partial h_i}{\partial \rho_i}\Omega_i^{-1}\sum_{l=1}^{N} m_l \nabla_i W_{il}(h_i)\right. \\ &\left. - \sum_{j=1}^{N}\sum_{k=1}^{N} m_j m_k \frac{\partial \phi_{jk}(h_j)}{\partial h_j}\frac{\partial h_j}{\partial \rho_j}\Omega_j^{-1} m_i \nabla_j W_{ji}(h_j)\right] \\ &= -\frac{G m_i}{2}\left[\frac{\xi i}{\Omega_i}\sum_{l=1}^{N} m_l \nabla_i W_{il}(h_i) - \frac{\xi j}{\Omega_j}\sum_{j=1}^{N} m_j \nabla_j W_{ji}(h_j)\right] \\ &= -\frac{G m_i}{2}\sum_{j=1}^{N} m_j \left[\frac{\xi i}{\Omega_i}\nabla_i W_{il}(h_i) - \frac{\xi j}{\Omega_j}\nabla_j W_{ji}(h_j)\right] \end{aligned} \tag{3.50}$$

where ξi is given by:

$$\xi_i = \sum_{k=1}^{N} m_k \frac{\partial \phi_{ik}(h_i)}{\partial h_i} \frac{\partial h_i}{\partial \rho_i} \tag{3.51}$$

and x_j is the same (replacing index i with index j).

The equation of motion for gravity is then found by putting back together Equations 3.49 and 3.50 to give:

$$\begin{aligned} \left(\frac{d\mathbf{v}_i}{dt}\right)_{\text{grav}} = &- \frac{G}{2} \sum_{j=1}^{N} m_j \left(\nabla_i \phi_{ij}(h_i) + \nabla_i \phi_{ij}(h_j)\right) \\ &- \frac{G}{2} \sum_{j=1}^{N} m_j \left(\frac{\xi i}{\Omega_i} \nabla_i W_{il}(h_i) - \frac{\xi j}{\Omega_j} \nabla_j W_{ji}(h_j)\right) \end{aligned} \tag{3.52}$$

Now that the full, variation equations of motion and thermal energy with self-gravity have been derived, an algorithm is needed to implement them. However, there is an additional concern which is necessary to address in order to implement SPH. This is explained in the next section.

3.3.4 Artificial Viscosity

Although SPH is generally a sufficiently accurate tool for modelling the dynamics of an ideal gas, there are specific circumstances in which interstellar gas cannot be modelled as ideal. During the collision of two supersonic gas flows, a shock front is formed which compresses the gas, causing it to heat up and preventing the two flows from freely passing through each other. Within this shock front, the specific entropy of the gas s increases, causing a problem for SPH simulations in which entropy is kept constant.

In order to correctly model the behaviour of a shock, variational SPH is modified through the addition of 'artificial viscosity'. In an SPH simulation of two colliding supersonic gas flows with no artificial viscosity, the SPH particles in each flow pass by each other with minimal interaction. Artificial viscosity adds a friction component to the particles' equations of motion and energy, which dampens their motion and converts that kinetic energy into heat.

If the mean of the speed of sound between SPH particles i and j is $\bar{c}_{ij}$ and the mean of the density of the two particles is $\bar{\rho}_{ij}$, then the artificial viscosity parameter between

those two particles Π_{ij} is given by:

$$\Pi_{ij} = \begin{cases} \frac{-\alpha \bar{c}_{ij} \mu_{ij} + \beta \mu_{ij}^2}{\bar{\rho}_{ij}} & \text{for } \mathbf{v}_{ij} \cdot \mathbf{r}_{ij} < 0 \\ 0 & \text{for } \mathbf{v}_{ij} \cdot \mathbf{r}_{ij} \geq 0 \end{cases} \tag{3.53}$$

where $\alpha \sim 1$ and $\beta = 2\alpha$ regulate the strength of the viscosity and μ_{ij} determines how its viscosity changes as the relative position and velocity changes:

$$\mu_{ij} = \frac{h_{ij} \mathbf{v}_{ij} \cdot \mathbf{r}_{ij}}{|\mathbf{r}_{ij}|^2 + \eta^2} \tag{3.54}$$

The constant η is added to prevent unphysical results when $|\mathbf{r}_{ij}|$ approaches zero.

If we define $\bar{W}_{ij}$ as the mean of $W_{ij}(h_i)$ and $W_{ij}(h_j)$, then the viscosity component to be added to the equation of motion is:

$$\left(\frac{d\mathbf{v}_i}{dt} \right)_{\text{visc}} = -\sum_{j=1}^{N} m_j \Pi_{ij} \nabla_i \bar{W}_{ij} \tag{3.55}$$

and the component to be added to the energy equation is:

$$\left(\frac{du}{dt} \right)_{\text{visc}} = \frac{1}{2} \sum_{j=1}^{N} m_j \Pi_{ij} \mathbf{v}_{ij} \cdot \nabla_i \bar{W}_{ij} \tag{3.56}$$

Although the addition of artificial viscosity helps to solve the problem of simulating shock fronts, it gives rise to a new problem with an over-abundance of viscosity in the simulation of shear flows. A correction introduced by Balsara (1995) decreases the strength of the viscosity for circumstances in which the shear is significant. This is achieved by estimating the ratio between the compression acting on each particle and the shear acting on each particle:

$$f_i = \frac{|\nabla_i \cdot \mathbf{v}_i|}{|\nabla_i \cdot \mathbf{v}_i| + |\nabla_i \times \mathbf{v}_i|} \tag{3.57}$$

Π_{ij} is scaled by the factor $\bar{f}_{ij} = (f_i + f_j)/2$.

The formulation of artificial viscosity used in the investigations in Chapter 6 was introduced by Monaghan (1997):

$$\Pi_{ij} = -\frac{\alpha}{2\rho_{ij}} \left(\left[c_i + c_j - \frac{3\mathbf{v}_{ij} \cdot \mathbf{r}_{ij}}{|\mathbf{r}_{ij}|} \right] \right) \tag{3.58}$$

With the addition of artificial viscosity the variational SPH contains all the necessary components for performing accurate simulations of gas dynamics, via time integration of the equation of motion and the energy equation. This time integration, plus other practical aspects of the SPH algorithm, is the focus of the next section.

3.4 Implementing SPH

3.4.1 Time Integration

Now that we have equations which describe the change of the position and energy of SPH particles over time, it is necessary to choose an appropriate algorithm to numerically integrate these equations to find the particles' properties as a function of time. For N-body simulations, the fourth-order Hermite scheme is used. However, the accuracy of the variational formulation of SPH is only second-order. This means that the use of a fourth-order integrator in SPH would add unnecessary computational time without that benefit of improved accuracy. The integration is instead performed by a less computationally demanding second-order leapfrog scheme.

A leapfrog scheme has two steps - a 'drift', in which the positions of the particles are advanced, and a 'kick', in which the velocities of the particle are advanced. The various types of leapfrog schemes are named after the sequence of their 'kick' and 'drift' steps. For example, a rudimentary 'kick-drift' leapfrog scheme advances the particles' velocities first, i.e.:

$$\mathbf{v}_{n+1} = \mathbf{v}_n + \mathbf{a}_n \Delta t \tag{3.59}$$

It then uses the newly calculated velocity to advance the position, i.e.:

$$\mathbf{r}_{n+1} = \mathbf{r}_n + \mathbf{v}_{n+1} \Delta t \tag{3.60}$$

In contrast, a 'drift-kick' leapfrog algorithm will advance the particles' positions first and calculate the gravitational acceleration at the new position, which is then use to advance the particles' velocities.

The investigations in Chapter 6 use the more sophisticated leapfrog 'kick-drift-kick' (KDK) algorithm, which increases the accuracy of the calculation to second order by

adding an extra step at $\Delta t/2$:

$$\begin{aligned}
\mathbf{v}_{n+\frac{1}{2}} &= \mathbf{v}_n + \frac{1}{2}\mathbf{a}_n \Delta t \\
\mathbf{r}_{n+1} &= \mathbf{r}_n + \mathbf{v}_{n+\frac{1}{2}} \Delta t \\
\mathbf{v}_{n+1} &= \mathbf{v}_{n+\frac{1}{2}} + \frac{1}{2}\mathbf{a}_{n+1} \Delta t
\end{aligned} \tag{3.61}$$

Where $\mathbf{a}_{n+1}$ is the acceleration due to gravity calculated at $\mathbf{r}_{n+1}$. A leapfrog 'drift-kick-drift' (DKD) algorithm is constructed in an analogous way, with the difference of having two position calculations rather than two velocity calculations. It performs just as well in hydrodynamical simulations as the KDK algorithm.

The the leapfrog KDK algorithm is used in this thesis because of its advantages in combining SPH simulations with N-body simulations, as is done with the GANDALF code which is introduced below.

3.4.2 Choice of Timestep

As with N-body particles, the choice of the size of the timestep Δt is crucial, as accurately simulating dense regions with large forces requires a relatively small timestep compared to diffuse isolated regions.

Individual timesteps are allocated to SPH particles depending on the environment around each particle. These individual timesteps Δt_i are calculated by finding the minimum between two criteria. The first is called a 'Courant-Friedrichs-Lewy' condition (Courant, Friedrichs & Lewy, 1928) and ensures that the integration remains stable (Hubber et al., 2013):

$$\Delta t_i^{\rm c} = \frac{\gamma^{\rm c} h_i}{(1+2\alpha)c_i + (1+1.2\beta)h_i \left|\nabla_i \cdot \mathbf{v}_i\right|} \tag{3.62}$$

where $\gamma^{\rm c}$ is a timestep multiplier. The second timestep is proportional to the acceleration due to the forces acting on the SPH particle:

$$\Delta t_i^{\rm a} = \sqrt{\frac{\gamma^{\rm a} h_i}{|\mathbf{a}_i| + \epsilon}} \tag{3.63}$$

where $\gamma^{\rm a}$ is another timestep multiplier and $\epsilon \ll 1$ prevents dividing by zero when $|\mathbf{a}_i|$ approaches zero.

The timestep Δt is calculated as the minimum of the values from Equation 3.62

and 3.63. The timesteps are then discretised using powers of 2, using the same method used for the N-body particles in Section 2.6.2 so that many particles can be advanced simultaneously.

3.4.3 The Barnes-Hut Tree

The larger the number of SPH particles, the closer the discretised Equation 3.6 is to Equation 3.5. In practical terms, SPH simulations work best if they have as many SPH particles as computationally possible. However, if the net gravitational force acting on a particle is calculated by summing the individual contributions of every other particle, then the number of calculations scales with the square of the number of particles N, and increasing N quickly becomes computationally expensive.

The use of an approximation can reduce the number of calculations from $\propto N^2$ to $\propto N \log N$ by treating subgroups of far away SPH particles as a single pseudo-particle whose mass and position are given by the total mass and centre of mass of the subgroup. The method used in Chapter 6 of this thesis is the Barnes-Hut tree algorithm (Barnes & Hut, 1986).

Application of a Barnes-Hut tree begins by dividing the entire simulated region into 8 equal-sized cubic subregions. Each of the subregions is then divided in turn into 8 sub-subregions. This continues recursively, with each new iteration producing another level of the tree and each new subregion representing a node in the tree (the top-most node of the tree is the entirety of the simulated region).

The recursion continues until, in the bottom-most level of the tree with the smallest nodes (subregions), each node contains either 1 or 0 SPH particles. The bottom-most nodes which contain a particle have a mass and position given by the mass and position of the particle it contains. The bottom-most nodes which don't contain a particle are given no mass. All other nodes are given a mass which is the total mass of its eight sub-nodes, and a position equal to the total centre of mass of its eight sub-nodes.

To calculate the gravitational force acting on a particle i, the algorithm begins at the top-most node. The separation d between particle i and the nodes centre of mass is calculated. If the ratio l/d (where l is the corner-to-corner size of the node) is greater than a threshold value θ, then the gravitational contribution of the particles within the node on particle i is calculated by treating the node as a single particle with a mass equal to the total mass of its sub-nodes and a position equal to the centre of mass of its sub-nodes. If the ratio l/d is less than the threshold value θ, then the algorithm repeats for each of the nodes eight sub-nodes. The algorithm continues recursively until

the contributions from all nodes have been calculated.

This approximation has the effect of decreasing the calculation speed significantly, from $\mathcal{O}(N^2)$ to $\mathcal{O}(N \log N)$. The size of the effect of the subsequent loss in accuracy depends on the choice of the accuracy parameter θ. The accuracy can be further improved by using higher-order multipoles to calculate the gravitational force acting on particle i due to a node containing particles j.

Taking l_i to be the distance between particle i and the nodes centre of mass, l_j is the distance between the nodes centre of mass and particle j (which is contained within the node), the first few terms of the multipole expansion for the gravitational force acting on particle i from the node containing particles j is given by:

$$\left(\frac{d\mathbf{v}}{dt}\right) \simeq \frac{G\sum_j m_j}{l_i^2} + \frac{G\sum_j m_j l_j}{l_i^3} + \frac{G\sum_j m_j l_j^2}{l_i^4} + \frac{G\sum_j m_j l_j^3}{l_i^5} + \tag{3.64}$$

The more terms used, the more accurate the force calculation at the expense of a larger computational cost.

Hubber et al. (2011) show that the highest cost benefit comes from using up to the l_i^4 term and discounting the l_i^3 term i.e.:

$$\left(\frac{d\mathbf{v}}{dt}\right) \simeq \frac{G\sum_j m_j}{l_i^2} + \frac{G\sum_j m_j l_j^2}{l_i^4} \tag{3.65}$$

This is the expression used for the investigations in Chapter 6. However, the multipole expansion can cause errors in calculation for certain initial conditions. To correct this, the multipole acceptance criteria (MAC) is used (Salmon & Warren, 1994):

$$\frac{G\sum_j m_j l_j^2}{l_i^4} < \alpha\,|\mathbf{a}| \tag{3.66}$$

Where $|\mathbf{a}|$ is the total acceleration on particle i due to gravity and α is a user-defined value between 0 and 1.

3.4.4 Initial Conditions

As with N-body simulations, SPH simulations require good initial conditions which will depend on the question that is being asked. The initial conditions of the gas should be similar enough to the gas structure observed in young stellar regions so that the answers that the simulations provide are useful for making predictions and finding observable diagnostics for the evolution of those young stellar regions. However, as with

N-body simulations, sometimes more simplified initial conditions are useful to provide a laboratory environment designed to answer a very specific question under very specific constraints. Chapter 6 focuses on simulations of model young stellar regions which are spherically symmetric.

In N-body simulations, a widely-used spherically-symmetric model is the Plummer model, which is described in detail in Section 2.7.4. An analogous spherically-symmetric model for the modelling of gas is the $n = 5$ polytrope. The Lane-Emden equation describes a spherically-symmetric fluid with a dimensionless radius ξ as:

$$\frac{1}{\xi^2}\frac{d}{d\xi}\left(\xi^2\frac{d\theta}{d\xi}\right) + \theta^n = 0 \tag{3.67}$$

Where $\theta^n = \rho/\rho_c$ and ρ_c is the central density and n is the polytropic index. The polytropes are the solutions to this equation give the following equation of state:

$$P = K\rho^{1+\frac{1}{n}} \tag{3.68}$$

A polytropic index equal to 5 provides the same density distribution for a fluid as the Plummer distribution does for a group of particles. This allows the positions of the SPH particles to be allocated using Equation 2.25. The initial velocities of the SPH particles are set to zero. Gravitational collapse of the gas is instead prevented by thermal pressure given by Equation 3.68 and specific internal energy given by:

$$u(r) = \frac{\sigma(r)^2}{\gamma 1} \tag{3.69}$$

Where the velocity dispersion σ is equated to the speed of sound $c_s = \sqrt{\gamma P/\rho}$ (Hubber et al., 2011).

3.4.5 The Hybrid *N*-body/SPH code GANDALF

The code used in Chapter 6 is the GANDALF hybrid N-body/SPH code developed by Hubber et al. (2013). It is a way of simulating the dynamical evolution of a young stellar region which is made up of both stars and gas, and in which the distribution of stars can affect the evolution of the gas, and the distribution of the gas can affect the evolution of the stellar distribution.

In order for the simulated stars and gas to interact gravitationally, the stars are treated as a special type of SPH particle with a fixed smoothing length. Using N_g as

the total number of gas particles, (i, j, k) as indices for summing gas particles, $N_\star$ as the total number of star particles and (a, b, c) as indices used to sum star particles, the full Lagrangian for a system of gas and stars can be written as (Hubber et al., 2011, 2013):

$$\mathcal{L}_{\rm SPH} = \sum_{j=1}^{N_g} \left(m_j \frac{\mathbf{v}_j^2}{2} - m_j u_j \right) + \sum_{b=1}^{N_\star} m_b \frac{\mathbf{v}_b^2}{2} + \mathcal{L}_{\rm grav} \tag{3.70}$$

where $\mathcal{L}_{\rm grav}$ is given by:

$$\mathcal{L}_{\rm grav} = -\frac{G}{2} \sum_{j=1}^{N_g} m_j \sum_{k=1}^{N_g} m_k \phi_{jk}(h_j) - \frac{G}{2} \sum_{b=1}^{N_\star} m_b \sum_{c=1}^{N_\star} m_c \phi_{bc}(h_b) - \frac{G}{2} \sum_{j=1}^{N_g} m_j \sum_{b=1}^{N_\star} m_b \phi_{jb}(h_j) \tag{3.71}$$

Using this to solve the Euler-Lagrange equation (Equation 3.30) givens the equation of motion for a star particle a as (a full derivation is found in Hubber et al. (2013)):

$$\mathbf{a}_a = -G \sum_{b, a \neq b}^{N_\star} m_b \phi_{ab}(h_a) \hat{\mathbf{r}}_a - G \sum_{j}^{N_g} m_j \phi_{aj}(h_a) \hat{\mathbf{r}}_a. \tag{3.72}$$

The motion of the star particles is integrated using the fourth-order Hermite scheme. For the integration of the gas particles, the second-order leapfrog KDK scheme is used. This gives decent accuracy and since the errors on the SPH scheme are of the order of $(\Delta t)^2$ anyway, there is no good reason to have a more computationally expensive integration scheme for the SPH particles. The fourth-order Hermite scheme and the leapfrog KDK scheme work well in parallel with each other as several steps in each scheme are done in sync at the same time.

3.5 Summary

With the N body and SPH tools described in Chapters 2 and 3, it is now possible to generate young stellar regions with initial conditions which will produce useful results, and plug those initial conditions into numerical simulations to track the dynamical evolution of a region with both stars and gas. Chapters 4, 5 and 6 focus on investigations using these numerical techniques, which aim to offer new insights into the study of the dynamical evolution of young stellar regions.

Chapter 4

Massive, Wide Binaries as Tracers of Massive Star Formation

4.1 Introduction

The tools and methods outlined in Chapters 2 and 3 are necessary for performing the N-body and SPH simulations which make up the foundations of the scientific investigations in Chapters 4, 5 and 6. In this chapter, we perform N-body simulations to study the origin of massive, wide binary systems in stellar associations, how they are formed, how they survive and how they are destroyed in young stellar regions with different properties. This work has been published as Griffiths et al. (2018).

In Section 1.1.6, two main 'theories' of star formation were introduced - 'competitive accretion' and 'core accretion'. One possible way to distinguish between these two theories is that core accretion predicts that high-mass stars will be more likely to reside in more isolated regions compared to competitive accretion (although competitive accretion does allow for runaway stars in isolated regions).

For example, Cyg OB2 has a mass of $\sim 10^5$ $M_\odot$ and a full IMF of massive stars up to 100 $M_\odot$ (Wright et al. 2015). With a size of ~ 20 pc, and a velocity dispersion of ~ 20 km s^{-1} (Wright et al. 2016) Cyg OB2 has a virial ratio of $Q_{\rm vir} \sim 10$ and is therefore a highly unbound association. However, all we can say is that Cyg OB2 is unbound at its *current* age of 2–10 Myr (it has a significant internal age spread), but it is unclear if the regions in which the massive stars formed were 'clustered' and have since expanded (although the structure of the association suggests not, Wright et al., 2014).

In this chapter we investigate massive wide binaries (MWBs) as a signature of how massive stars form. A MWB is two massive stars in a binary that is potentially wide

enough to be dynamically destroyed or altered. Because such binaries are susceptible to destruction in dense environments (see Section 1.2.3), they can carry information on the density history of their environment.

We define a MWB as a binary system in which both stars have masses greater than 5 $M_\odot$, and which have a separation, a, between $10^2 < a < 10^4$ AU. Later we discuss the observed MWBs in Cyg OB2, and in the observations of Caballero-Nieves et al. (in prep.; our choice of $\sim 5M_\odot$ is partly motivated by the detection limit of this survey, but this is not very important to our results).

There are three things that make such MWBs (>5 $M_\odot$) particularly interesting. Firstly, because the primaries and secondaries are both bright (O, B or A-stars) and well-separated they are relatively easy to find as visual binaries even at large distances.

Secondly, MWBs are the only type of binary system that can be easily produced by three-body encounters between stars. Equation 1.12 shows that the binary formation rate is heavily dependent on the stellar mass m, and therefore favours the formation of high-mass binaries over low-mass ones. Looking at Equation 1.12 for MWBs specifically, we expect MWB formation to depend on the (number) density of massive stars (the n^3 term), moderated by the velocity dispersion (σ^{-9}). So we would expect more MWBs to form at higher densities and in the presence of other massive stars. This is rather non-trivial as higher densities usually mean higher velocity dispersions, so in a virialised cluster with radius R we would expect $\sigma^9 \propto n^{9/2}R^9$, so $n^3/\sigma^9 \propto 1/(n^{3/2}R^9)$.

Thirdly, even at such wide separations they are normally intermediate, or even hard binaries in that *low-mass* stars do not carry enough energy to disrupt them, as 5 $M_\odot$ is significantly more massive than a 'typical' star (0.2–0.5$M_\odot$).

In Section 1.2.3, I explain how binaries can be defined as 'hard', 'intermediate' or 'soft' according to the difference between the binding energy of the binary $|E_{\rm bind}|$ and the typical energy in an encounter $E_{\rm enc}$, or by the critical velocity given by Equation 1.15. From this, we can see that for a MWB comprised of two 5 $M_\odot$ stars, in order to destroy the binary, the velocity of a 1 $M_\odot$ perturber would need to be over three times larger than that of a 50 $M_\odot$ perturber. Therefore MWBs are only susceptible to disruption by other 'massive' stars.

Whether a binary will survive or be disrupted depends not only on the energy/velocity of an encounter, but the rate of encounters close enough to disrupt the binary. The encounter rate, $t_{\rm enc}$, is inversely proportional to both the number density and velocity dispersion, $\propto 1/(n\sigma)$ (see Equation 1.14). In a virialised cluster of radius R, the encounter rate will therefore depend on the crossing timescale of the cluster, given by

Equation 1.23, as $t_{\rm enc} \propto t_{\rm cr}^3/R$. In addition, the velocity of encounters has a dependency $\sigma \propto n^{1/2}R$ which complicates any estimates of encounter rates.

For MWBs the encounter rate has another subtlety. The number density of interest is not the number density of all stars, but rather the number density of stars massive enough to potentially destroy the binary. Generally this will be significantly lower than the 'average' number density, but can be enhanced by (primordial or dynamical) mass segregation (which can then reduce the velocity dispersion of the massive stars so reducing their encounter energy).

There is yet another subtlety that needs to be borne in mind: encounters can harden a binary (i.e. decrease the binary separation), in particular if the encounter velocity is $<< v_{\rm c}$ (i.e. the Heggie-Hills Law (Heggie, 1975; Hills, 1975, 1990)). This can mean that a massive binary with an initial separation greater than the nominal 100 AU limit for 'wide' can be hardened below this limit and 'drop out' of a MWB sample (we see this effect later). This depends on the encounter rate in the same way as destructive encounters, but if hardening or softening encounters dominate depends on the each encounter energy relative to the particular MWB energy.

The above discussion shows that the rate at which MWBs are destroyed is rather complex and has no simple dependencies on time-scales such as the crossing time. The binary destruction rate will also be rather stochastic depending on if a MWB has an encounter with enough energy to destroy it (see e.g. Parker & Goodwin 2012), or if encounters harden a binary below a nominal limit. Ensembles of N-body simulations are required to investigate the interplay of the formation and destruction of binaries in order to determine how the initial properties of a cluster determines the number of MWBs which reside in that cluster as it evolves.

4.2 Method/Initial Conditions

The investigations in this chapter aim to use N-body simulations to determine whether the numbers of MWBs in a region are tied to the past density and dynamical history of that region, in particular the past history of the massive stars.

We perform ensembles of N-body simulations using the KIRA N-body integrator from the Starlab package (Portegies Zwart et al., 2001).

Throughout, we define a MWB as a binary system comprised of two stars each with masses greater than 5 $M_\odot$, with an instantaneous 3D separation between 10^2 and 10^4 AU. Note that the instantaneous 3D separation is not the same as the semi-major axis

of the orbit (it is likely to be somewhat larger, depending on the eccentricity of the orbit and the current phase), and it is not the same as the projected separation that would be observed. We pick the instantaneous 3D separation for simplicity due to the dependence of the projected separation on viewing angle (the instantaneous separation is therefore an upper limit on any projected separation).

Every simulation starts as a virialised Plummer sphere (Plummer, 1911) with a total mass of stars $M_T \simeq 600$ M$_\odot$ (~ 400 stars $> 0.1 M_\odot$). We pick $\sim 600 M_\odot$ as that is the mass at which we would expect one or two O-stars ($> 20 M_\odot$) if randomly sampling from a standard IMF.

The stars in each simulated region are allocated a position and velocity using the method described in Aarseth et al. (1974) and Section 2.7.4. The timescale of each simulation is 10 Myr, and no stellar evolution is included.

Whilst virialised Plummer spheres are very simple initial conditions, we expect *any* initial distribution to relax to something similar to a virialised Plummer-like distribution within a few initial crossing times as long as it is initially bound (see e.g. Allison et al. 2009b; Allison & Goodwin 2011).

We perform two sets of simulations: set 'N' that start with no MWBs, and set 'B' in which we place a 'primordial' MWB. Here 'primordial' is defined as present at the start of the simulation - it does not have to have formed primordially like the binaries in Section 1.2.1, but could have formed dynamically at an earlier time (Although we note that this MWB could have formed dynamically during an earlier relaxation phase of the region which we ignore).

For all of the primordial binary 'B' scenarios, the primordial MWB is composed of two stars, star α and star β. Star α is the primary star in the primordial binary, and has a mass of 20 M$_\odot$. The secondary, star β, mass is uniformly randomly sampled between 10 M$_\odot$ and 20 M$_\odot$, giving a binary mass ratio of $0.5 \leq q_{\alpha\beta} \leq 1.0$. The binary separation for these primordial binaries is chosen uniformly between 1000 and 5000 AU (within our working definition of a MWB), and the eccentricity is set to zero.

For all of the 'N' scenarios, stars α and β, which make up the primordial binaries in the 'B' scenarios, are still present. However, they are not part of a binary system but are instead single stars, randomly placed in the Plummer sphere.

We run ensembles of 100 simulations in which we vary only the random number seed used to set the initial conditions. Each ensemble is run with (B) and without (N) a primordial MWB in one of four scenarios (see below) with four different initial densities (see below) for a total of 3200 simulations.

Scenario	Mass Function	No. of Stars with $M > 30$ M$_\odot$	Primordial Binary?
N1	Flat 1 M$_\odot$	0	No
N2	Maschberger	0	No
N3	Maschberger	1	No
N4	Maschberger	5	No
B1	Flat 1 M$_\odot$	0	Yes
B2	Maschberger	0	Yes
B3	Maschberger	1	Yes
B4	Maschberger	5	Yes

Table 4.1: A summary of the differences in the initial conditions. In the first column, scenarios are numbered 1–4 with 'N' for no primordial MWBs, and 'B' for an primordial MWB (repeated in column 4 for clarity). The second column has the stellar mass function used (flat or 'normal'). The third column has the number of very massive stars ($> 30M_\odot$) in the cluster.

1. All other stars are low-mass. In ensembles N1 and B1 all stars other than α and β (be they part of a binary or two single stars) have a mass of 1 M$_\odot$.

2. All other stars are lower-mass with a normal IMF. In ensembles N2 and B2, all of the stars which make up the cluster, except for stars α and β, have masses randomly sampled from the standard single star Maschberger IMF (Maschberger, 2013). A lower limit of $0.1M_\odot$ prevents the inclusion of brown dwarfs and other objects with masses far too low to affect the binary, the upper limit of $10M_\odot$ means that the stars α and β are the most massive stars in the cluster. (We force the masses of the two most massive stars to be 10–20 and $20M_\odot$, but as mentioned above this would be expected for this total cluster mass.)

3. The cluster includes one more massive star. Ensembles N3 and B3 are the same as N2 and B2 but with the addition of a single new higher-mass star, with a mass between 30-35 M$_\odot$, to the cluster.

4. The cluster contains three more (single) massive stars. The last ensembles, N4 and B4, add 3 more massive stars to the cluster, each with masses between 30 and 50 M$_\odot$.

Note that a higher mass limit on the background cluster stars of 10 M$_\odot$ allows for the existence of more stars with masses greater than 5 M$_\odot$, from which a MWB could form. In total, there are up to ~ 20 stars with masses greater than 5 M$_\odot$ in each of the ensembles N2-N4 and B2-B4. In principle, any of these could form a MWB in our definition of a MWB.

In each of the eight ensembles above, the clusters are given four different initial

densities: half-mass radii, $R_{0.5}$, of 0.25, 0.5, 1 and 1.5 pc. For a cluster with a half-mass radius between $0.25 \leq R_{0.5} \leq 1.5$ pc, the half-mass density (in $M_\odot$ pc^{-3}) is $1.25 \leq \log \rho_{1/2} \leq 3.58$, the upper limit of this is of a similar density to the Arches cluster, while the lower limit is similar to RSGC03 (Portegies Zwart et al., 2010) (both clusters contain several massive stars).

For reference, the crossing times of the clusters (given by Equation 1.23) are roughly 0.08, 0.25, 0.66 and 1.2 Myr for $R_{0.5} = 0.25$, 0.5, 1.0 and 1.5 pc respectively. Note that while it is possible to calculate a relaxation time for these clusters, that number is rather difficult to interpret or give any meaning to as N is so low.

Table 4.1 gives a summary of the different initial conditions in each of the eight scenarios, N1-N4 and B1-B4, based on the mass distribution of stars in the cluster, and whether stars α and β begin in a primordial massive wide binary or whether they begin as single stars.

4.3 Results

We will first consider the formation of MWBs in ensembles that start with no binaries (N1-N4), and then both the formation *and* destruction of MWBs in ensembles with primordial MWBs (B1-B4). The method used for identifying a binary system is that of Parker et al. (2009).

4.3.1 The formation of MWBs

All simulations N1-N4 initially contain no binary systems. Table 4.2 shows the number (out of 100) of simulations in which a MWB is found to be present after 10 Myr for each scenario (N1-N4) at each density ($R_{0.5} = 0.25, 0.5, 1, 1.5$ pc), also presented in Figure 4.1. All MWBs found at 10 Myr in the N simulations *must* have formed dynamically.

What is most obvious is that the efficiency of MWB formation strongly depends on the density. This should be of no surprise as the formation rate depends on n^3.

Each of the scenarios are very similar, with 60–90 per cent of dense simulations ($R_{0.5} = 0.25$ and 0.5 pc) forming MWBs, but only 0–20 per cent of low-density ($R_{0.5} = 1$ and 1.5 pc) simulations forming MWBs (almost none at $R_{0.5} = 1.5$ pc).

In Scenario N1 (blue solid line in Figure 4.1), in which there are only two 'massive' stars (all other stars are $1 M_\odot$) a MWB forms in the majority (70–80 out-of-100) of simulations at low $R_{0.5}$. One of the reasons that the formation rate is so high when

Scenario	Number of Simulations Containing a Massive, Wide Binary at $t = 10$ Myr			
	$R_{0.5} = 0.25$ pc	0.50 pc	1.00 pc	1.50 pc
N1	81	73	3	0
N2	63	74	16	5
N3	92	89	16	2
N4	87	82	22	1

Table 4.2: Number of MWBs which formed in clusters with different initial half-mass radii $R_{0.5}$, for each of the no primordial MWB Scenarios N1-N4.

there are only two stars that could form a MWB is that these stars dynamically mass segregate, bringing them close together (increasing n^3, and also increasing $1/\sigma^9$).

Scenario N2 (green dashed line in Figure 4.1) has two stars with masses greater than 10 $M_\odot$, and a range of low- and intermediate-mass neighbours. Only two thirds of the simulation contain a massive wide binary at 10 Myr (less than in scenario N1). This is not because MWBs have not formed, but due to the fact that once formed, a reasonable fraction have been hardened by interactions with other stars, so that their binary separation is less than 100 AU. There therefore exists in some of these simulations a population of massive, 'tight' binaries with separations < 100 AU which we do not classify as MWBs (although these are *nowhere* near as tight as the few-day period massive star binaries commonly found in spectroscopic surveys).

In Scenario N3 (red dot-dashed line in Figure 4.1), there are three stars with masses greater than 10 $M_\odot$, and a range of lower-to-intermediate-mass stars. The number of simulations which form a massive wide binary at small $R_{0.5}$ is slightly higher than in Scenario N1 (although note that the $\sqrt{N}$ 'noise' on these numbers are about ± 10). In this case the third massive star carries enough energy to disrupt any newly formed MWBs and so these clusters are constantly forming, then destroying, then forming etc. MWBs (cf. Moeckel & Clarke 2011).

In Scenario N4 (cyan dotted line in Figure 4.1), there are five stars with masses greater than 10 $M_\odot$ and a range of lower-mass stars. The situation is almost exactly the same as in scenario N3 with a constantly forming and then destroyed population of MWBs.

In scenarios N2-N4, it is possible to have two MWBs present (two pairs of the 5-20 available stars above 5 $M_\odot$), but this is rare and short-lived.

In summary, if no MWB is present at the start of a simulation then in dense environments then *one* MWB is likely to form. In low-density environments it is very unlikely

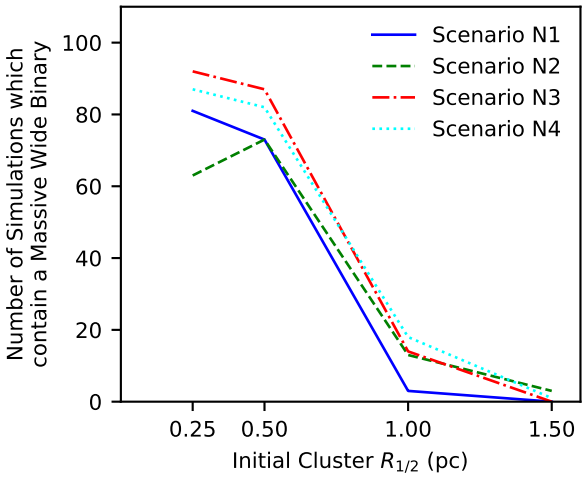

Figure 4.1: Number, out of 100, of clusters with no primordial MWB which contain at least one MWB after 10 Myr, as a function of the initial cluster half-mass radius, $R_{0.5}$, for Scenarios N1 (blue solid line), N2 (green dashed line), N3 (red dot-dashed line), and N4 (cyan dotted line).

Scenario	Number of Simulations in which the Original Massive, Wide Binary Survived to $t = 10$ Myr			
	$R_{0.5} = 0.25$ pc	0.50 pc	1.00 pc	1.50 pc
B1	100	100	100	100
B2	68	72	92	97
B3	11	22	72	89
B4	7	18	52	74

Table 4.3: Number of primordial WMBs which survived for 10 Myr, in clusters with different initial half-mass radii $R_{0.5}$, for each of Scenarios B1-B4.

that a MWB will form.

4.3.2 The Destruction and Formation of MWBs

In Scenarios B1 to B4 all clusters have a primordial MWB. But as we have seen MWBs can form dynamically, and so in scenarios B3 and B4 it is quite possible to have a MWB that is comprised of different stars to the primordial MWB. Therefore we distinguish between the survival of the primordial MWB, and the presence of *any* MWB after 10 Myr (this may be the primordial MWB, or may be a 'new' MWB).

Table 4.3 gives the numbers (out-of-100) of surviving *primordial* MWBs for scenarios B1-B4 for each density, this is illustrated in Figure 4.2.

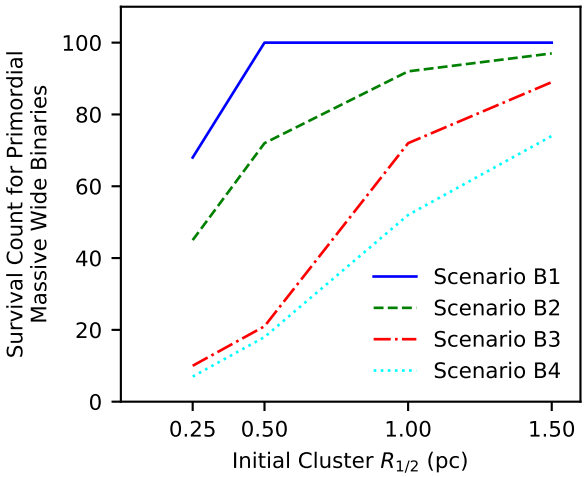

Figure 4.2: Number, out of 100, of clusters with a primordial MWB in which the primordial MWB survives for 10 Myr, as a function of the initial cluster half-mass radius $R_{0.5}$, for Scenarios B1 (blue solid line), B2 (green dashed line), B3 (red dot-dashed line), and B4 (cyan dotted line).

In Scenario B1 (blue solid line in Figure 4.2) there are two massive stars in a MWB, and all of the cluster stars are 1 $M_\odot$. Here *all* of the primordial MWBs survive regardless of density as the low-mass stars do not have enough energy to disrupt the massive wide binary, but encounters do harden around a quarter of the MWBs in the densest clusters ($R_{0.5} = 0.25$) below our nominal MWB limit, hence the MWB fraction declines.

In Scenario B2 (green dashed line), the primordial MWB is surrounded by other low-to-intermediate-mass stars. At high densities ($R_{0.5} = 0.25$ and 0.5 pc) encounters can again harden a binary below our MWB definition. To add a further complication, it is possible to destroy the primordial MWB, and then it reforms (cf. Scenario N2), and then it can be hardened below our MWB limit.

Therefore in around a third of systems with a primordial MWB one is not present after 10 Myr, although this does depend on our (somewhat arbitrary) definition of a MWB.

Scenarios B3 and B4 both have a primordial MWB, plus one or three (single) higher-mass stars. At high densities ($R_{0.5} = 0.25$ and 0.5 pc) the primordial MWB is very unlikely to survive. In most cases this is not because it is hardened below our definition, but rather that it is destroyed by an encounter. At lower densities ($R_{0.5} = 1$ and 1.5 pc) the survival of the primordial MWB is a matter of 'luck' as to whether it encounters the/one of the other massive stars in the cluster or not, but 50–80/100 of the primordial

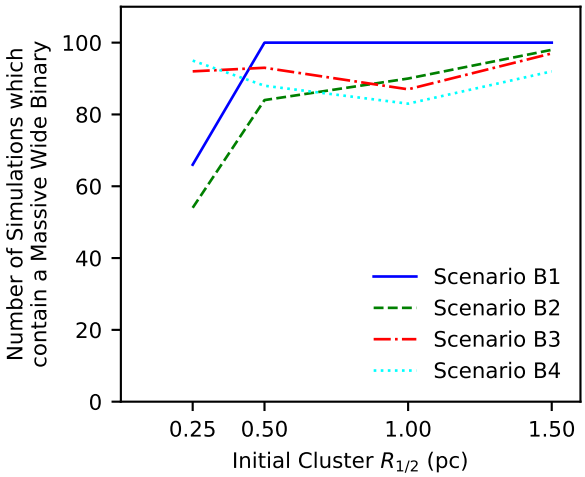

Figure 4.3: Number, out of 100, of clusters which contained a primordial MWB which have at least one MWB at 10 Myr, as a function of the initial cluster half-mass radius $R_{0.5}$, for Scenarios B1 (blue solid line), B2 (green dashed line), B3 (red dot-dashed line), and B4 (cyan dotted line).

MWBs are able to survive for 10 Myr (see the red and cyan lines).

In Figure 4.2 we saw the fraction of primordial MWBs that survived. However, as we saw in section 3.1, MWBs can be formed as well as destroyed.

In Figure 4.3 we show the number of simulations which contain *any* MWB at 10 Myr, as a function of the initial cluster half-mass radius $R_{0.5}$.

In scenario B1 (blue solid line), any MWB must be the primordial MWB (as there are only two stars capable of making-up a MWB), and so for B1 figs. 4.2 and 4.3 are identical. The reason that they are not 100% at all densities is because some of the surviving MWBs have been hardened below our nominal limit for a WMB, as explained above.

This hardening effect also occurs in scenario B2 (green dashed line) where hardening is slightly more effective due to the presence of some stars $> 1M_{\odot}$). The number of clusters with any MWB (Figure 4.3) is slightly higher than the numbers of primordial MWBs because other $\sim 5M_{\odot}$ stars are present in the masses drawn from the IMF that can swap into the MWB, but this is a minor effect.

In scenarios B3 and B4 (red and cyan lines) there are one or three other massive stars, and some (typically about 8) $\sim 5M_{\odot}$ stars are present in the masses drawn from the IMF. Any of these other stars could pair to form a MWB. In Figure 4.2 we see that the primordial MWB rarely survives at higher densities ($R_{0.5} = 0.25$ and 0.5 pc), but

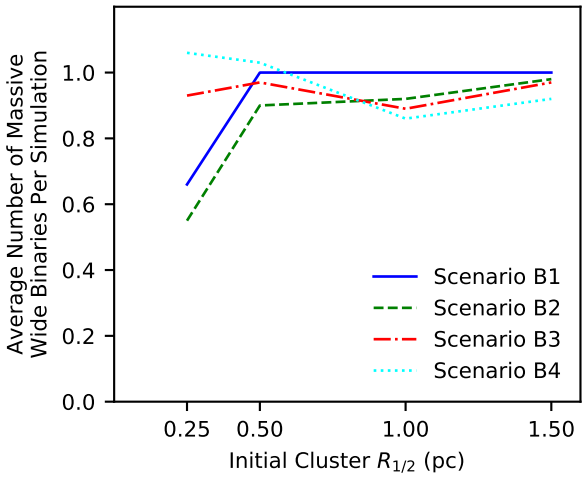

Figure 4.4: Mean number of MWBs in each cluster that contained a primordial MWB after 10 Myr, as a function of the initial cluster half-mass radius $R_{0.5}$. Error bars are $\pm 1\sigma$ over the ensembles of 100 simulations. For Scenarios B1 (blue solid line), B2 (green dashed line), B3 (red dot-dashed line), and B4 (cyan dotted line).

Figure 4.3 shows that the vast majority of these clusters do contain a MWB at these densities: this is a 'new' MWB formed dynamically (as seen in Figure 4.1 where there are no primordial MWBs).

In scenarios B2, B3 and B4 it is possible to have two MWBs present; this is rare, but does sometimes happen. Figure 4.4 shows the *mean* number of massive wide binaries found in each simulation at $t = 10$ Myr, as a function of the initial cluster half-mass radius, for each scenario B1-B4 (i.e. for each different mass distribution).

Figure 4.4 shows that the expected number of MWBs in each cluster, given that each cluster initially contains one primordial MWB, is close to unity. The only times the number of MWBs is not about unity is Scenarios B1 and B2 at very high density ($R_{0.5} = 0.25$ pc), when binary hardening decreases the number of MWBs to an average of ~ 0.6 per cluster.

In Scenarios B2, B3 and B4 there are usually about 10 stars that could potentially pair to make a MWB. However, due to the disruption of MWBs by other high-mass stars, only the most massive of MWBs will be stable for a significant time.

To help understand the survival of the MWBs, Figure 4.5 shows the critical velocity for destruction, as defined by Equation 1.15, for each of the MWBs that were present at the *end* of each simulation for all of our scenarios (N1–4 and B1–4) assuming a perturber mass of $m_{\rm pert} = 1$ M$_\odot$. The dotted line shows the critical velocity for the

lowest possible mass MWB (5+5$M_\odot$), and the dashed line for the highest possible MWB mass (50+50$M_\odot$), for separations between 10^2 and 10^4 AU.

In Figure 4.5 all of the MWBs marked by coloured points (different colours for different scenarios) lie above the lower dotted line which is the critical velocity a 1 $M_\odot$ star must have to destroy the lowest-possible mass MWB (5+5$M_\odot$). This is exactly as expected as all simulations contain significant numbers of 1 $M_\odot$ stars and so should be hard enough to avoid destruction by these stars (although a soft binary could exist for a short time before being destroyed, see Moeckel & Clarke, 2011).

At any particular separation in Figure 4.5 increasing critical velocities for destruction mean increasing system masses (if a is the same, then m_p and/or m_s must be greater for v_c to be larger).

In Figure 4.5 the critical destruction velocities for MWBs in scenarios N1/B1 (blue points) lie in a fairly tight band as they are all $m_\mathrm{p} = 20$ $M_\odot$ and $m_\mathrm{s} = 10$–20 $M_\odot$ MWBs. These MWBs are all well above the typical velocities of the 1 $M_\odot$ stars making-up the rest of the cluster and so they survive (although can be hardened below 100 AU).

The critical destruction velocities for MWBs in scenarios N2/B2 (orange points) are more widely spread and to lower critical velocities than scenarios N1/B1 as some MWBs can form with a 5 $M_\odot$ companion from the cluster.

In scenarios N3/B3 (green points) almost all binaries are the 20 $M_\odot$ primary from the primordial MWB in a new MWB with the 30–35 $M_\odot$ 'other' massive star leading to almost the same critical velocities at each separation. The shift between the blue N1/B1 points and the green N3/B3 points thus shows the difference in the masses of the two most massive stars that will pair up as a MWB.

Scenarios N4/B4 (red points) have five massive stars (possibly as high a mass as 50 $M_\odot$) and the spread represents whatever the two highest masses happen to be.

Hence the 'hardness' of a system is much more representative of the masses available to combine into a MWB than the destructiveness of the environment. The two most massive stars will pair into a wide binary which will almost certainly be hard enough to avoid destruction.

4.3.3 Summary

To quickly summarise the results we refer to $R_{0.5} = 0.25$ and 0.5 pc as 'high-density' and $R_{0.5} = 1$ and 1.5 pc as 'low-density'.
A) If no MWBs are present in a cluster they will very often form dynamically at high-density, but not at low-density (see Figure 4.1).

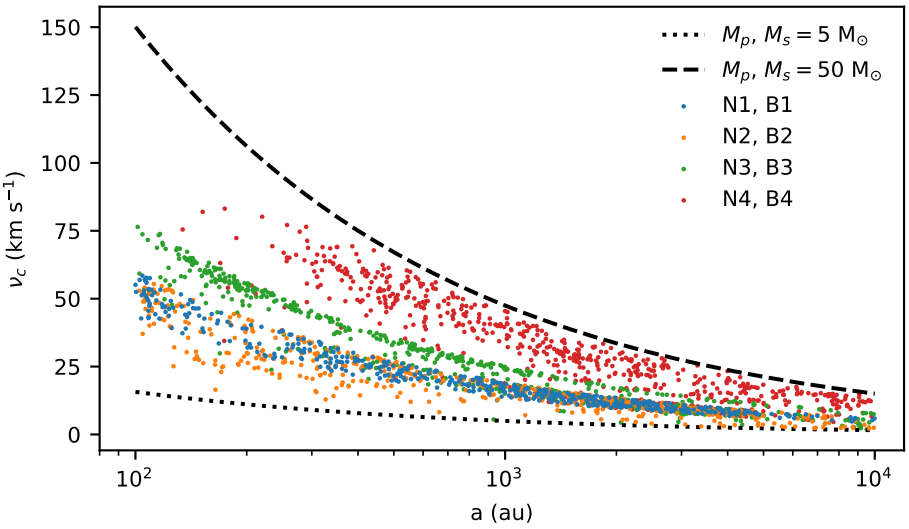

Figure 4.5: The critical velocity, as defined in Equation 1.15, for each of the MWBs that were present at the end of each simulation for scenarios N1, B1 to N4, B4 assuming a perturber of mass $m_{\rm pert} = 1$ M$_\odot$. The dotted line represents primary and secondary masses of 5 M$_\odot$ and the dashed line represents primary and secondary masses of 50 M$_\odot$.

B) Primordial MWBs will usually survive at low-density, and only be destroyed at high-density if other massive stars are present (see Figure 4.2).
C) When primordial MWBs are destroyed at high-density they are usually 'replaced' by a new MWB (because of (A), see Figure 4.3).
D) On average, one MWB will be found in each dense region (see Figure 4.4).

The only environment we simulate in which we do not usually see just a single MWB present at 10 Myr are low-density clusters that did not have a primordial MWB.

4.4 Discussion

In most environments we simulated, almost always a *single* MWB is present at 10 Myr. The only environments in which MWBs are rare are low-density environments which never had a MWB. This is because of two competing effects:

1. MWBs are 'hard' to lower-mass stars (which do not carry enough energy to disrupt the MWB), but 'soft' or 'intermediate' to other massive stars (which do carry enough energy). Therefore they are destroyed when other massive stars are present in an environment dense enough to allow encounters.

2. MWBs readily form in dense environments due to the $m^5 n^3$ dependence of the

binary formation rate shown in Equation 1.12 (The massive star density in dense clusters is also enhanced by rapid dynamical mass segregation increasing n^3 significantly).

An important point is that if a MWB is present there is almost always only a single MWB. MWBs are soft/intermediate in the presence of other massive stars which means they are constantly being destroyed and formed when other massive stars are present (Moeckel & Clarke, 2011). The balance between the formation and destruction of MWBs in dense environments means that they are a probe of the past density history of a region as we show below for Cyg OB2.

4.4.1 The past history of Cyg OB2

Cyg OB2 is a $2-10$ Myr old, $\sim 10^5 M_\odot$ unbound association with a current size of ~ 20 pc, with a 3-dimensional velocity dispersion of ~ 18 km s^{-1} Cyg OB2 is unbound (Wright et al. 2016 and references therein). That Cyg OB2 is *currently* unbound makes determining its past dynamical history difficult. It is possible that it was one, or several, initially bound (sub)clusters that have each become unbound (due to gas expulsion?), or that it was always globally unbound. We argue that the MWB population is a useful tracer of the past density history.

Very usefully observationally, that a MWB has two massive (ie. bright), widely-separated, components means that they should be observable in fairly distant regions (at least a few kpc) where the low-mass population is much more difficult to observe. Caballero-Nieves et al. (in prep., hereafter CNip) have observed a sample of 74 O-star primaries in Cyg OB2 to search for wide 100–10000 AU companions (it is somewhat more subtle than this as detection depends on separation and magnitude difference). CNip are able to detect more distant companions to a mass of (very roughly) $4 M_\odot$ at wider separations (hence our adoption of 5 $M_\odot$ as a 'massive' star).

What is important for our discussion here is that CNip find a wide, massive companion for 38 of the 74 primaries (~ 51 per cent MWB fraction). Note that it may well be that one or both components of each MWB are themselves close binaries – this makes no difference to our argument.

There are three ways in which we can explain the large number of MWBs in Cyg OB2:

1. Firstly, that many massive stars in Cyg OB2 formed in low-density environments in primordial MWBs. Therefore what we observe are a large number of primordial MWBs.

2. Secondly, that massive stars formed in *many* small, dense groups (either in primordial MWBs or not), and each group formed (on average) about one MWB. Therefore what we observe are a large number (at least 40) of dynamically formed MWBs, roughly one per sub-region.

3. Thirdly, some mixture of the first and second possibilities, with the observed population being a mix of primordial and dynamically-formed MWBs.

Whichever of the three possibilities is correct it means that *massive star formation in Cyg OB2 was widely distributed*. It was either almost completely isolated, or in many small, dense groups (or some mix of these): but it could not have been as a single (or even a few) dense 'clusters'. This is in agreement with Wright et al. (2014) and Wright et al. (2016) who argue from the distribution and kinematics of Cyg OB2 that it has always been widely distributed and unbound.

Cyg OB2 has a standard IMF, i.e. has the number of massive stars expected for a region of $10^5 M_\odot$ (Wright et al. 2015). The number of MWBs very strongly suggests that there were many sites of massive star formation that did not know about each other (they never interacted dynamically, otherwise we would not see so many MWBs). Therefore, whatever mechanism forms massive stars must be able to 'randomly sample' the IMF, e.g. it can form very massive stars (up-to $100 M_\odot$ in Cyg OB2) without 'knowing' that the total mass of the region is very large. This suggests the cluster mass-maximum stellar mass relationship is statistical rather than fundamental (Weidner & Kroupa 2004; Parker & Goodwin 2007).

4.4.2 How to use the numbers of MWBs

More generally, in any region one can think of four possibilities in terms of the numbers of MWBs that are present:

1. Currently high-density with very few or no MWBs: No information on the primordial MWB population as most/all would have been destroyed if they existed. The region could have been lower density in the past and collapsed, or always high density.

2. Currently low-density with very few or no MWBs. If the region was denser in the past that would have destroyed most/all primordial MWBs, if it was always low-density then there were few/no primordial MWBs.

3. Currently high-density with many MWBs. This is unexpected: it must have spent only a little time at a high-density otherwise we would expect all but one (or two) primordial MWBs to have been destroyed, and no more than one (or two) to possibly have formed.

4. Currently low-density with many MWBs (e.g. Cyg OB2). Either the region was always low-density with many primordial MWBs, or it contained many small 'sub-clusters' that could each form a MWB.

Our wording has been rather woolly here in terms of 'high-density/low-density' or 'number of MWBs'. How many MWBs are significant depends on the number of massive stars that are present to pair into MWBs, and the masses of those stars relative to those around it. It is difficult to say much from only two massive stars either being in a MWB or not. However, apparently half of the large population of massive stars in Cyg OB2 being in MWBs is clearly significant ('many'). The point at which 'many' becomes 'few' is less clear, and is a judgement call based on the details of any particular region that is being examined.

4.5 Conclusion

We define Massive Wide Binaries (MWBs) as binary systems containing two stars of mass $> 5M_{\odot}$ with separations between 10^2 and 10^4 AU (ie. bright, visual binaries in the high-mass tail of the IMF).

We examine the interplay between the destruction and formation of MWBs in (virialised Plummer sphere) clusters of total mass $\sim 600M_{\odot}$ (~ 400 stellar members) using N-body simulations.

Our clusters always either have a 'primordial' MWB or just two single massive stars. The rest of the stars in the cluster are: (a) all Solar-mass; (b) an IMF with no other stars more massive than $10M_{\odot}$; (c) an IMF with one other (more) massive star; or (d) an IMF with three other (more) massive stars. For each mass range we run ensembles of 100 simulations for 10 Myr with half-mass cluster radii of 0.25, 0.5, 1 and 1.5 pc.

Our main results can be summarised as follows:

1. Primordial MWBs almost always survive in low-density environments, or any environment with no other massive stars.

2. Primordial MWBs are usually destroyed in high-density environments when other massive stars are present.

3. A single MWB very often forms dynamically in high-density environments.

4. MWBs rarely form dynamically in low-density environments.

The combination of these results means that the only (local) environment in which no MWB will be present is a low-density cluster which contained no primordial MWB. In all other (local) environments either a single primordial MWB will survive, or (almost always) a single MWBs can be formed dynamically.

Therefore, any region containing many MWBs must either be (or have been) many high-density sub-clusters (which form one MWB each), many primordial MWBs which never encountered another massive star, or some mixture of both. What it could not have been is a single, dense cluster (or fewer dense [sub-]clusters than there are MWBs).

The low-density association Cyg OB2 has approximately 40 MWBs (with a MWB fraction of roughly a half). This is further evidence that Cyg OB2 has always been globally diffuse, and must have contained either many (at least about 40) small high-density regions in which to either dynamically form MWBs, or contained many primordial MWBs that have always been in low-density environments.

Chapter 5

The Formation of Very Wide Binaries in a Supervirial Association

5.1 Introduction

The investigations in Chapter 4 show that wide binary systems do not survive in dense environments, unless they are the most massive objects in their proximity. Furthermore, they show that the chance of a wide binary forming in the field is so low as to be negligible. This chapter focuses on a mechanism for the formation of wide binary systems that may account for the presence of some of the wide binaries observed in the Galaxy.

The typical binary separation a lies between 10 and 10000 AU (Sterzik et al., 2003). However, binaries have been observed with separations as wide as 0.1 pc (in the Galactic disk) and 1 pc (in the halo) (Close et al., 1990; Chaname & Gould, 2003; Dhital et al., 2015). Approximately 5% of field G-dwarfs are a member a binary system which has a binary separation $a > 10000$ AU (Duquennoy & Mayor, 1991). In this chapter, we define any binary which has a binary separation $a > 10000$ AU as a 'very wide binary' (VWB).

As shown in Section 1.2.3, a binary will be destroyed by a perturbing star if the velocity of the perturber is greater than the critical velocity v_c given by Equation 1.15. As $v_c \propto a^{-1}$, the critical velocity for a binary with $a = 10000$ AU is a hundred times lower than a binary with the typical separation (~ 100 AU), making it likely that the binary will be destroyed in any encounter with a third perturbing star.

In fact, VWBs are not only easily destroyed in an encounter with another star. Their low v_c means that they are slowly pulled apart by weak tidal forces. The fact that VWBs are destroyed in this way means that they are useful as diagnostics. Observations of VWBs can be used for mapping the mass structure of the Galaxy, including constraining

estimates of the mass distribution of Massive Compact Halo Objects (MACHOs) in the Galactic halo (Carr et al., 2016).

Although approximately 5% of stars are members of a VWB, the properties of VWBs make it difficult to determine how they are formed. Section 1.2.1 explains how binaries with a smaller separation are formed primordially from the fragmentation of a core of molecular gas. However, Ward-Thompson et al. (2007) show that the typical size of a star-forming core is approximately 10000 AU, which means that binaries with 10000 AU $< a <$ 1 pc are unlikely to have formed primordially. In Chapter 4 and in Griffiths et al. (2018) it is shown that wide binaries do not typically survive in stellar clusters and associations, where most young stars are found, unless they are composed of two of the most massive stars in the region.

The mystery of the formation of VWBs is compounded by their short lifetimes. The constant tidal force applied by the Galactic mass distribution means that the majority of VWBs will dissipate within 1.5 Gyr (Oelkers et al., 2016). This short lifetime means that the population of VWBs must be continually replenished to yield the observed VWB population.

If VWBs do not form primordially, then the other option is that they form dynamically. However, it has already been shown in Section 1.2.2 that wide binary systems can almost never form in the field (see Equation 1.12) and that any VWBs that form dynamically in denser regions will be destroyed almost immediately (Moeckel & Clarke, 2011; Griffiths et al., 2018).

Reipurth & Mikkola (2012) raise the possibility that at least a subset of the observed VWB population is comprised not of binaries, but triples instead - a tight inner binary with a more distant third companion. The triple would have formed as a more compact system. Over time, the interactions between the three stars cause a transfer of energy, between two of the stars (whose separation decreases) and the third companion (whose separation from the others increases). The result is a triple system consisting of a compact, tightly bound pair and a much more distant third star. Since observations of the compact pair will generally be unresolved, this system will be observed as a VWB when in reality it is a triple with a very wide outer companion.

Because the unfolding process takes time, there should be no VWBs in a very young stellar region, and the number of VWBs in a region should increase over time. However, very young regions are observed to have VWBs and the fraction of VWBs decreases over time (Tokovinin, 2017).

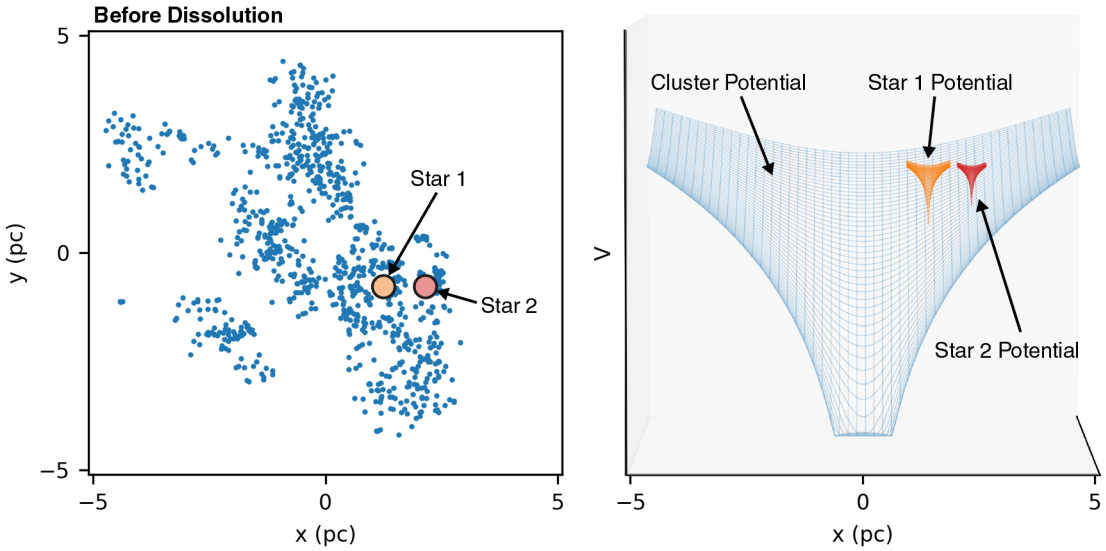

Figure 5.1: The significance of the aggregate gravitational influence of all of the stars in a dense environment compared to that of two stars which are in close proximity to one another. The diagram on the left shows the x-y positions (in pc) of an expanding, unbound region ~ 5 pc across, with two stars ('Star 1' and 'Star 2') which may become a VWB in the future. The diagram on the right shows a representation of the gravitational potential wells of Star 1, Star 2 and of the region as a whole.

5.1.1 Soft Capture

A further way of forming VWBs is via the 'soft capture' mechanism during the dissolution of a star cluster (Kouwenhoven et al., 2010; Moeckel & Clarke, 2011).

In the soft capture scenario, the prospective members of a VWB start out as single stars in a dense region. While the region is dense, the strength of the gravitational interactions between the prospective VWB members is dwarfed by the aggregate gravitational influence of all of the other stars in the region. This influence prevents the prospective VWB members from forming a long-lived binary system.

This scenario is illustrated in Figure 5.1. The diagram on the left shows the supervirial young stellar region with two stars ('Star 1' and 'Star 2') highlighted. These stars may eventually form a VWB when the region expands. However, the diagram on the right shows a representation of the gravitational potential wells of Star 1, Star 2 and of

the region as a whole. The gravitational influence of the two stars on one another is dwarfed by the aggregate influence of the region background potential, and hence the two stars remain unbound.

In Section 1.3.7 it is explained that, due to either gas expulsion or due to the dynamical state of a dense young stellar region, that region can lose enough mass to become supervirial, i.e. $Q_{\rm vir} > 1$. If a dense region is supervirial, then its size will increase and its density will decrease over time. This increases the distance between stars, thereby decreasing the strength of the gravitational influence of stars situated on different sides of the region on one another. At a certain critical point, the strength of the gravitational interactions between neighbouring stars becomes more significant than the influence of the rest of the stars in the region. If the dynamical properties (relative positions, velocities etc.) of the two prospective VWB members allow for the formation of a binary, and if the background gravitational potential of the region continues to wane, then the prospective VWB members will become gravitationally bound and therefore 'locked into' a binary. The initial wide separations of the stars in these binaries mean that any binaries which form will have a large separation, permitting the potential formation of a population of VWBs.

Figure 5.2 shows the same scenario as Figure 5.1, after the region has evolved for 25 Myr. The diagram on the left shows the x-y positions (in pc) the same regions as Figure 5.1 which is now ~ 100 pc across, with the stars ('Star 1' and 'Star 2') which are now members of a VWB. The diagram on the right shows the sizes of the gravitational potential wells of Star 1 and Star 2 relative to that of the region. From comparing Figure 5.2 with Figure 5.1, it is possible to see that the gravitational potential well of the association as a whole has become shallower and wider as the association has expanded. The diagram on the right shows that, after 25 Myr, the gravitational potential well of the association as a whole is negligible compared to that of the two red stars, which allows them to become gravitationally bound and 'locked into' a VWB system.

The formation of VWBs during the dissolution of a centrally-concentrated star cluster has been investigated by Moeckel & Clarke (2011) and Kouwenhoven et al. (2010), but it was not a sufficiently efficient method to account for the number of observed VWBs. This chapter focuses on the number of VWBs which can form as a result of the expansion of more diffuse and clumpy stellar associations. This is for two reasons:

1. Firstly, more young (OB) stars are observed in less dense associations than in dense clusters (e.g. Ward & Kruijssen, 2018).

2. Secondly, Wright et al. (2014, 2016) and Chapter 4 showed that young star forming

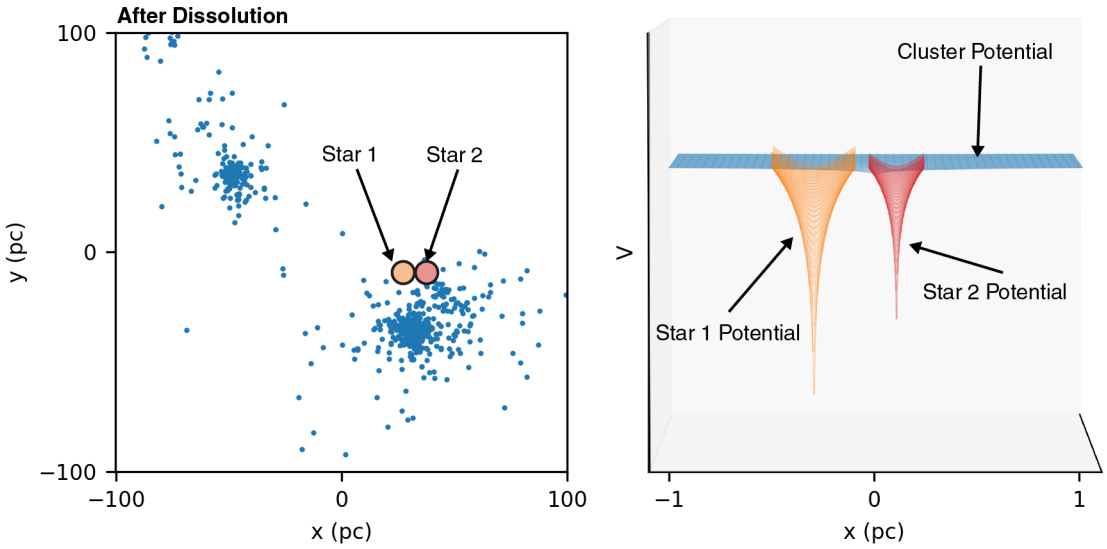

Figure 5.2: The significance of the gravitational influence of two stars in a VWB compared to that of an association which has expanded for 25 Myr. The diagram on the left shows the x-y positions (in pc) the same regions as Figure 5.1 which is now $\sim$ 100 pc across, with the stars ('Star 1' and 'Star 2') which are now members of a VWB. The diagram on the right shows the change from Figure 5.1 of the relative sizes of the gravitational potential wells of Star 1, Star 2 and of the region as a whole.

regions do not necessarily have to evolve from a much more dense region, i.e. the dense clusters previously studied may not be as significant a mode of star formation as once thought.

The investigations in this chapter attempt to answer the question, 'how many very wide binaries can form via soft capture in an expanding stellar association?', using N-body simulations to model simulated associations and varying the initial properties of those models. Section 5.2 below describes how the initial conditions for these simulations are generated. Section 5.3 shows the results of the simulations (with different sets of initial conditions), before Section 5.4 discusses the consequences of those results and their significance to our knowledge of VWB formation. The chapter conclusions are outlined in Section 5.5.

5.2 Method and Initial Conditions

The aim of the investigations in this chapter is to determine the rate of VWB formation during the dissolution of globally unbound stellar associations, and to determine whether that rate is affected by varying the initial properties of the associations. The initial conditions are constructed to be similar to what might be expected of moderately massive associations with total number of stars $N = 500$ and $N = 5000$.

The N-body simulations were performed with the KIRA fourth-order Hermite integrator (see Chapter 2) from the Starlab package (Portegies Zwart et al., 2001).

5.2.1 Mass Distribution

The masses of the individual stars in the simulation are allocated by randomly sampling the Maschberger (2013) initial mass function from Section 2.7.3. The minimum star mass is set to 0.1 $M_\odot$, in order to limit the waste of computational resources on brown dwarf-sized objects. The maximum star mass was set to 10 $M_\odot$. Although stars with $M > 10$ $M_\odot$ are observed in OB associations, it is assumed that, due to their short lifetimes, they have undergone supernova, causing gas expulsion in the region which has caused it to become globally gravitationally unbound.

5.2.2 Global Virial Ratio

As explained above, the simulated associations are globally gravitationally unbound. In other words, they have an initial virial ratio $Q_{\rm vir} > 1$. The virial ratio is the ratio of

total kinetic energy to total gravitational potential energy - the higher the value of $Q_{\rm vir}$, the faster the stars are moving apart and the faster the association expands. The size of this time frame in which the association expands out into the field may be significant, because a longer time frame means that the gravitational influence of the association is significant for longer, but also gives a longer time in which neighbouring stars will stay close enough to become gravitationally bound. It is therefore reasonable to change this time frame by changing the initial virial ratio of the associations, to see what effect this has on the formation of VWBs.

Five values of $Q_{\rm vir}$ were chosen ($Q_{\rm vir}$ =1.05, 1.15, 1.25, 1.35 and 1.50). Although the global value of $Q_{\rm vir}$ is greater than unity, clumpy associations may have subregions which are more or less strongly gravitationally bound, and may disperse over a longer or shorter timescale than the region as a whole.

5.2.3 Initial Density

The initial density of the simulated associations is set to approximately 80 stars pc^{-3}, because this density is similar to known unbound Galactic associations (Portegies Zwart et al., 2001). This yields an initial size of ~ 1.8 pc across for $N = 500$ stars, and ~ 4.0 pc across for $N = 5000$ stars.

5.2.4 Fractal Dimension

As explained in Chapter 1, Galactic associations contain spatial and velocity substructure. To simulate this structure, the stars are allocated 3D positions and velocities using the box fractal method introduced in Goodwin & Whitworth (2004) and explained in Section 2.7.5. One parameter needed for the application of this method is the fractal dimension $F_{\rm dim}$, which is a measure of the amount of substructure in a region.

As the initial amount of substructure within an association affects the difference in position and velocity of the stars therein, varying the value of $F_{\rm dim}$ may vary the number of stars which remain in close proximity to their neighbours as the association expands. As the soft capture mechanism depends partly on the prospective VWB members' proximity to one another, the initial fractal dimension may affect the formation rate of VWBs via soft capture. To measure the potential effect of the initial clumpiness of a supervirial association on the formation of VWBs, the initial value of $F_{\rm dim}$ is varied between four values: 1.6, 2.0, 2.6 and 3.0. These values are chosen so that $2^{F_{\rm dim}}$ (equal to the mean number of children - see Section 2.7.5) is approximately an integer, which

Variable	Values
N	500, 5000
$F_{\rm dim}$	1.6, 2.0, 2.6, 3.0
$Q_{\rm vir}$	1.05, 1.15, 1.25, 1.35, 1.50

Table 5.1: A summary of the initial conditions used for simulating the formation of VWB systems during the dispersal of a supervirial stellar association.

prevents divergences (due to randomness) of the star distribution from the chosen fractal dimension.

5.2.5 Multiplicity

Unlike real associations (Duchêne & Kraus, 2013), the simulated regions contain no binary or multiple systems - all stars are single-star systems. This was in order to reduce the chance for other potential VWB-forming mechanisms to have an effect. For example, softening of intermediate binaries (Parker & Goodwin, 2012), or the unfolding of a triple system to create the appearance of a VWB (Reipurth & Mikkola, 2012). This paper focuses specifically on the VWBs that may form via soft capture, at the expense of other potential mechanisms.

5.2.6 Summary

The variation of $Q_{\rm vir}$ ($Q_{\rm vir}$ = 1.05, ,1.15, 1.25, 1.35 and 1.5), $F_{\rm dim}$ ($F_{\rm dim}$ = 1.6, 2.0, 2.6 and 3.0) and N (N =500 and 5000) produces 40 unique sets of initial conditions. 10 simulations are performed for each of these 40 sets, with the stellar masses, positions and velocities initialised using a different random seed, reducing the effect of stochasticity. Each simulated region is evolved for 25 Myr to give each association the chance to fully disperse. Table 5.1 summarises the different sets of initial conditions used for the simulations in this chapter.

5.3 Results

5.3.1 500-Star Associations

All Binary Systems

Figure 5.3 shows the mean (from 10 simulations) percentage of stars which are in a binary at the end of the simulation (t = 25 Myr), as a function of the initial virial ratio

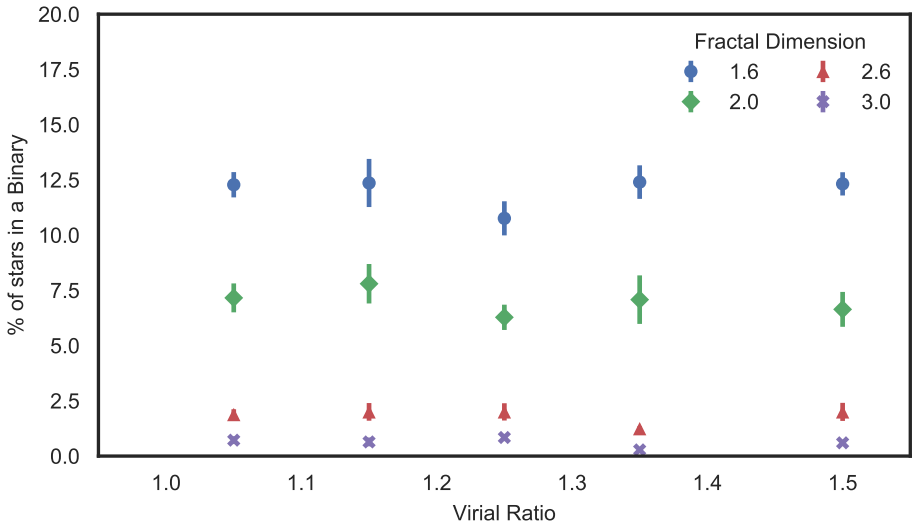

Figure 5.3: The mean (from 10 simulations) percentage of the total number of stars in a dispersing stellar association (stellar number $N = 500$) which are in a binary system at $t = 25$ Myr, as a function of the initial virial ratio of the association.

of the dissolved stellar association. This is shown for each of the associations with initial stellar number $N = 500$ stars.

We define 'binary' as two stars for which the binding energy (Equation 1.13) is negative, which are not bound to any other stars and which have a separation $a < \bar{a}/4$ where $\bar{a}$ is the average local distance between stars (see Parker et al., 2009 for more details).

The set of initial conditions in Figure 5.3 which results in creation of the most binary systems is $Q_{\rm vir} = 1.15$ and $F_{\rm dim} = 1.6$, which yields a percentage of the total number of stars which are in a binary at $t = 25$ Myr as $12.4\% \pm 0.8\%$. The set of initial conditions which results in the fewest binary systems is $Q_{\rm vir} = 1.35$ and $F_{\rm dim} = 3.0$, which yields a percentage of $0.3\% \pm 0.1\%$. However, Figure 5.3 shows that this variation is not significantly affected by varying the virial ratio of the association - the percentage of stars in a binary is constant (within uncertainties) as a function of the association's initial virial ratio $Q_{\rm vir}$.

This may be because, at the beginning of the simulation, most of the stars which will eventually form a binary already have the required relative positions and velocities in order to form a binary, but are only prevented by the interactions with other stars in close proximity. Once the association is dispersed, these outside influence are removed which allows the binary to form. Therefore, as long as the time is long enough to allow

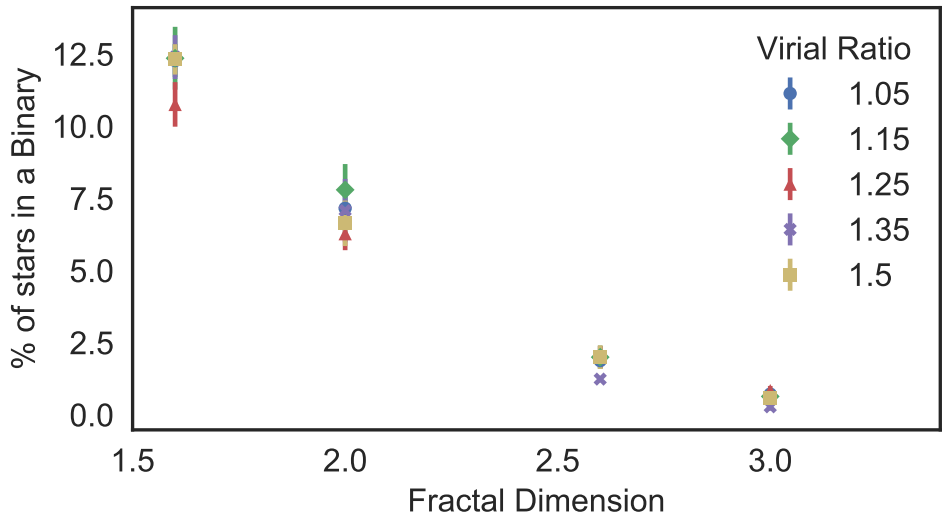

Figure 5.4: The mean (from 10 simulations) percentage of the total number of stars in a dispersing stellar association (stellar number $N = 500$) which are in a binary system at $t = 25$ Myr, as a function of the initial fractal dimension of the association.

the association to disperse, time after that becomes a relatively unimportant factor. This is further discussed in Section 5.4. The upshot is that the virial ratio of a region has no effect on the number of binaries which form during the dissolution of that region, so that any effect is solely due to the changing of the fractal dimension.

Figure 5.4 shows the mean (from 10 simulations) percentage of stars which are in a binary at the end of the simulation ($t = 25$ Myr), as a function of the initial fractal dimension of the dissolved stellar association. This is shown for each of the associations with stellar number $N = 500$ stars.

The percentage of stars which are in a binary at $t = 25$ Myr decreases as a function of the initial fractal dimension $F_{\rm dim}$, from 10.8–12.4% for $F_{\rm dim} = 1.6$ to 0.3–0.8% for $F_{\rm dim} = 3.0$. A smaller initial fractal dimension appears to be more efficient at producing binary systems than a larger initial fractal dimension. This implies that a dispersing association with significant substructure will yield a greater percentage of binaries than an association in which the substructure has been erased. Intuitively, a smaller fractal dimension produces a 'clumpier' distribution of positions and velocities, which increase the chance for two stars to have the necessary relative positions and velocities in order to eventually become a binary.

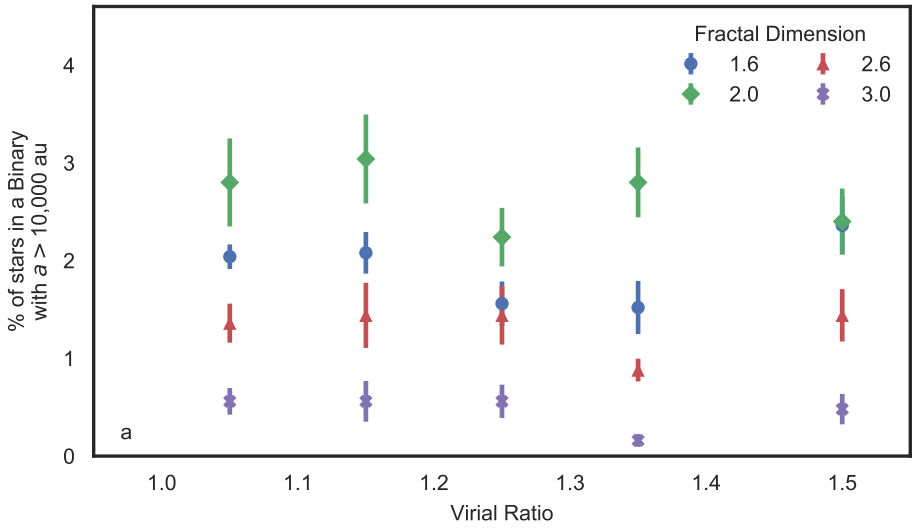

Figure 5.5: The mean (from 10 simulations) percentage of the total number of stars in a dispersing stellar association (stellar number $N = 500$) which are in a very wide binary ($a > 10000$ AU) at $t = 25$ Myr, as a function of the initial virial ratio of the association.

Very Wide Binaries

Out of the 2682 binaries which were formed in total (i.e. for all values of $F_{\rm dim}$ and $Q_{\rm vir}$), 29.6% are in VWBs, which are the main focus of this chapter.

Figure 5.5 shows the mean (from 10 simulations) percentage of stars which are in a VWB ($a > 10000$ AU) at the end of the simulation ($t = 25$ Myr), as a function of the initial virial ratio of the dissolved stellar association, for all associations with stellar number $N = 500$.

In contrast with Figure 5.3 above, the set of initial conditions in Figure 5.5 which results in creation of the most VWBs systems is $Q_{\rm vir} = 1.15$ and $F_{\rm dim} = 2.0$, which yields a percentage of the total number of stars which are in a VWB at $t = 25$ Myr as $3.0\% \pm 0.5\%$. The set of initial conditions which results in the fewest binary systems is $Q_{\rm vir} = 1.35$ and $F_{\rm dim} = 3.0$, which yields a percentage of $0.16\% \pm 0.07\%$. As with the binary systems in Figure 5.3, the percentage of stars in a VWB is constant (within uncertainties) as a function of the association's initial virial ratio $Q_{\rm vir}$, showing that there is no significant effect of varying $Q_{\rm vir}$ on the formation of VWBs.

Figure 5.6 shows the mean (from 10 simulations) percentage of stars which are in a VWB ($a > 10000$ AU) at the end of the simulation ($t = 25$ Myr), as a function of the initial fractal dimensions of the same associations as Figure 5.5.

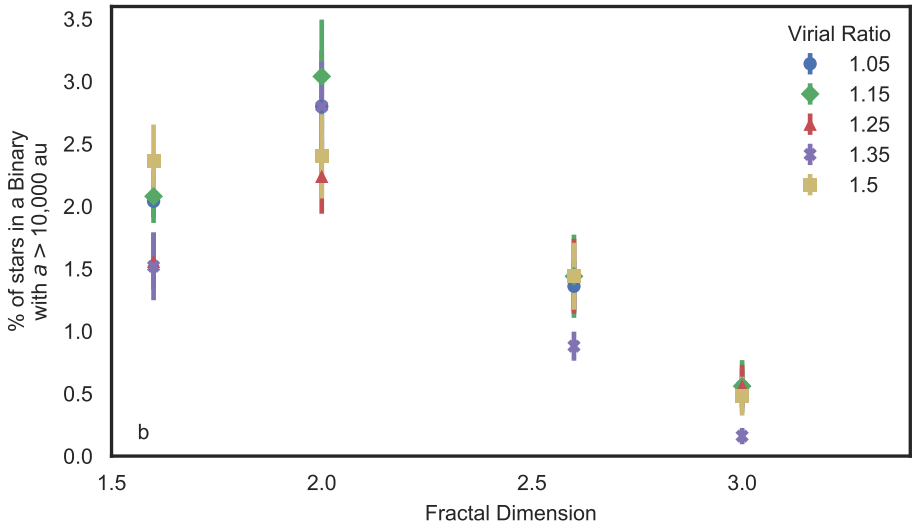

Figure 5.6: The mean (from 10 simulations) percentage of the total number of stars in a dispersing stellar association (stellar number $N = 500$) which are in a very wide binary ($a > 10000$ AU) at $t = 25$ Myr, as a function of the initial fractal dimension of the association.

Contrary to the binary systems in Figure 5.3, the percentage of stars in a VWB is largest for the initial fractal dimension $F_{\rm dim} = 2.0$ at 2.2–3.0%, rather than for $F_{\rm dim} = 1.6$. Therefore, it is not necessarily true that a higher amount of substructure will yield a greater fraction of VWBs in the dispersal of a stellar association - there appears to be a point, closest to $F_{\rm dim} \sim 2.0$, after which the efficiency of formation of VWBs drops off. At a lower value of $F_{\rm dim}$, higher degree of substructure appears to hinder the formation of VWBs.

The left-hand of Figure 5.7 shows the cumulative distribution of semi-major axes for each binary formed in all simulated dispersing stellar associations with total stellar number $N = 500$ and fractal dimension $F_{\rm dim} = 1.6$, 2.0, 2.6 and 3.0. The right-hand of Figure 5.7 shows these cumulative distributions normalised by the total number of binaries in the associations. It shows that, although more binary systems form in associations with a low fractal dimension, VWBs will make up a larger fraction of the binary population of associations with a large fractal dimension.

Figure 5.8 shows the cumulative distribution of the binary eccentricities (5.8A) and mass ratios (5.8B) for binaries with separations $a < 10000$ AU (green line) and binaries with separations $a > 10000$ AU (blue line).

Both eccentricity distributions are consistent with a thermal eccentricity distribution ($f(e) = 2e$, Heggie, 1975) which occurs when stars are randomly paired into binary

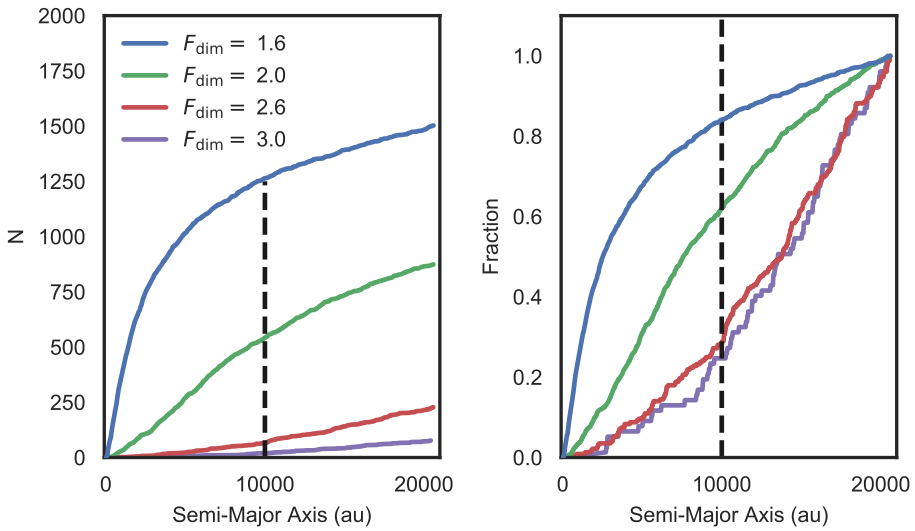

Figure 5.7: The cumulative distribution of semi-major axes for each binary formed in simulated dispersing stellar associations with total stellar number $N = 500$ and fractal dimension $F_{\rm dim} = 1.6$, 2.0, 2.6 and 3.0. The right-hand plot shows the total number and the right-hand plot shows the normalised distribution. The dashed black line shows the lower limit ($a = 10000$ AU) for the semi-major axes of very wide binary systems.

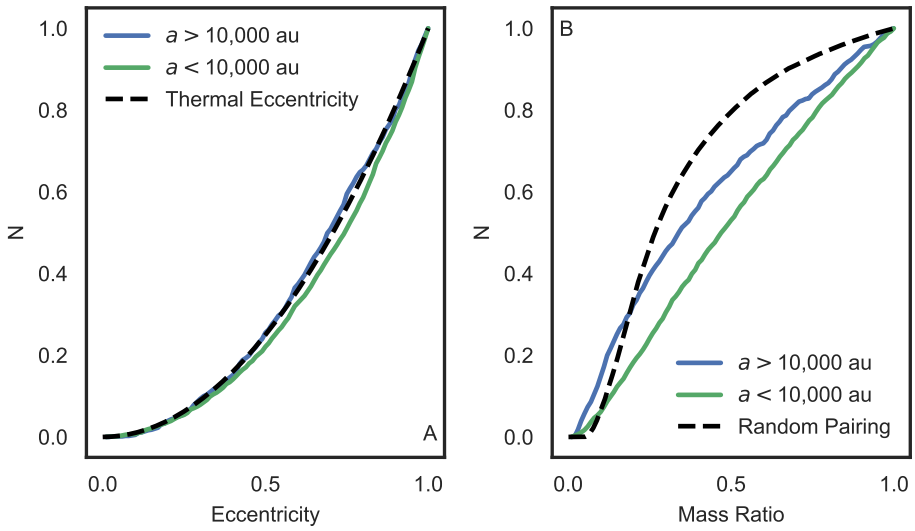

Figure 5.8: The cumulative distribution of the eccentricities (Figure 5.8A) and mass ratios (Figure 5.8B) for the binaries formed during the dissolution of a 500-star association. Distribution for very wide binaries are shown in blue and distributions for binaries with semi-major axes $a < 10000$ are shown in green. The dashed black line shows the theoretical expectations.

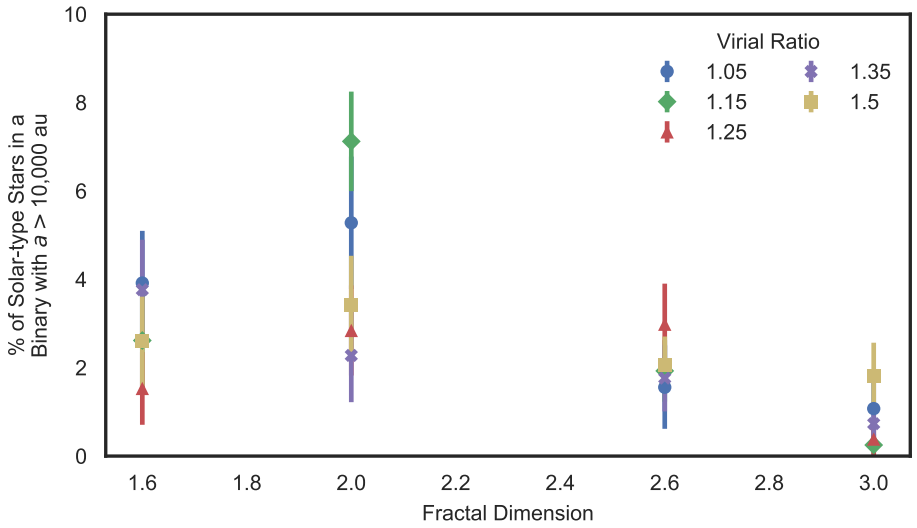

Figure 5.9: The mean (from 10 simulations) percentage of the number of *solar-type* stars (0.8-1.2 $M_{\odot}$) in a dispersing stellar association (stellar number $N = 500$) which are in a very wide binary ($a > 10000$ AU) at $t = 25$ Myr, as a function of the initial fractal dimension of the association.

systems, which is what is expected from binaries which result due to the 'soft capture' mechanism .

However, the mass ratio distributions for the separations $a < 10000$ and $a > 10000$ show some differences. The distribution of mass ratios for binaries with a separation $a < 10000$ is flat, whereas the mass ratio distribution for binaries with a separation $a > 10000$ is skewed towards lower mass ratios. This is due to gravitational focusing by higher-mass stars making it more likely that they will have a companion, coupled with the larger number of low-mass stars, making it more likely that the companion will be low mass.

Figure 5.9 shows the mean (from 10 simulations) percentage of solar-type (0.8-1.2 $M_{\odot}$) stars which are in a binary at the end of the simulation ($t = 25$ Myr), as a function of the the initial fractal dimension of the stellar association, for all simulated associations with stellar number $N = 500$.

For solar-type stars, the most 'efficient' initial conditions (i.e. $Q_{\rm vir} = 1.15$; $F_{\rm dim} = 2.0$ allow for a percentage of the total number of solar-type stars which are in a binary at $t = 25$ to be as high as $7.1\% \pm 1.1\%$.

As around 5% of stars are members of a VWB (Duquennoy & Mayor, 1991), the value of $7.1\% \pm 1.1\%$ would lead to the conclusion that VWB formation during the dissolution of supervirial associations could contribute a significant fraction of the VWB population.

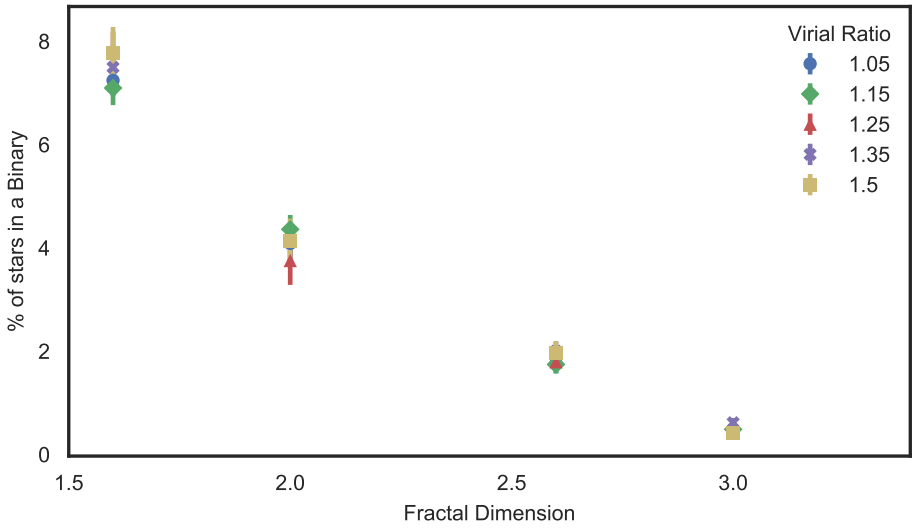

Figure 5.10: The mean (from 10 simulations) percentage of the total number of stars in a dispersing stellar association (stellar number $N = 5000$) which are in a binary system at $t = 25$ Myr, as a function of the initial fractal dimension of the association.

However, when taking into account the destruction of VWBs, the value is still too small to account for VWB formation on its own. Furthermore, this value represents the best of all possible initial conditions and varies significantly depending on the initial virial ratio $Q_{\rm vir}$, from $7.1\% \pm 1.1\%$ for $Q_{\rm vir} = 1.15$ to $2.5\% \pm 1.4\%$ for $Q_{\rm vir} = 1.35$, raising the possibility that stochasticity can have a large effect on how many VWBs form.

5.3.2 5000-Star Associations

As well as associations with 500 stars, simulations of associations with total stellar number $N = 5000$ were performed, for each of the same sets of initial conditions.

All Binary Systems

Figure 5.10 shows the mean (from 10 simulations) percentage of stars which are in a binary at the end of the simulation ($t = 25$ Myr), as a function of the initial fractal dimension of the dissolved stellar association, for all simulated associations with total stellar number $N = 5000$.

The percentage of the total number of stars which are in a binary at $t = 25$ Myr spans between $7.8\% \pm 0.4\%$ for the initial conditions most likely to form a binary, to $0.42\% \pm 0.06\%$ for the initial conditions which are least likely. Comparison with Figure

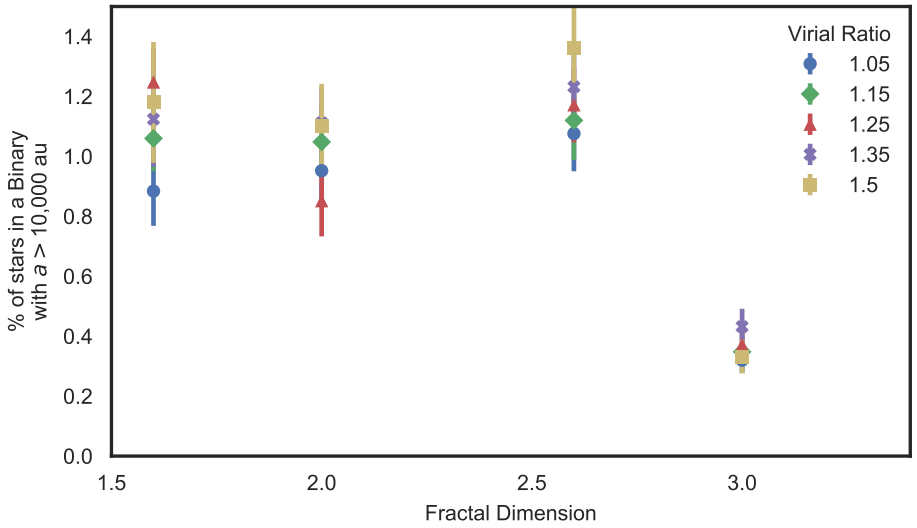

Figure 5.11: The mean (from 10 simulations) percentage of the total number of stars in a dispersing stellar association (stellar number $N = 5000$) which are in a very wide binary ($a > 10000$ AU) at $t = 25$ Myr, as a function of the initial fractal dimension of the association.

5.4 shows a significant decrease in the percentage of the total number of stars which will form a binary system, from $12.4\% \pm 0.8\%$ to $7.8\% \pm 0.4\%$. This implies that the total stellar number N of an association affects the number of binary systems that will form via soft capture, even though the stellar number density n remains constant. This is discussed further in Section 5.4.2.

Very Wide Binaries

Figure 5.11 shows the mean (from 10 simulations) percentage of stars which are in a VWB ($a > 10000$ AU) at the end of the simulation ($t = 25$ Myr), as a function of the initial fractal dimension of the dissolved stellar association, for all simulated associations with total stellar number $N = 5000$. The most efficient possible initial conditions result in $1.36\% \pm 0.14\%$ of stars being a member of a VWB after the dissolution of the simulated associations at $t = 25$ Myr.

Comparison with Figure 5.6 for $N = 500$, the value of $F_{\rm dim}$ most likely to form VWBs is $F_{\rm dim} = 2.6$, although the the percentage of stars in a VWB changes little for lower $F_{\rm dim}$. One way of thinking about this is that the point at which the formation of VWBs drops off has moved from $F_{\rm dim} = 2.0$ for $N = 500$ to $F_{\rm dim} = 2.6$ for $N = 5000$.

Figure 5.12 shows the mean (from 10 simulations) percentage of solar-type (0.8-1.2

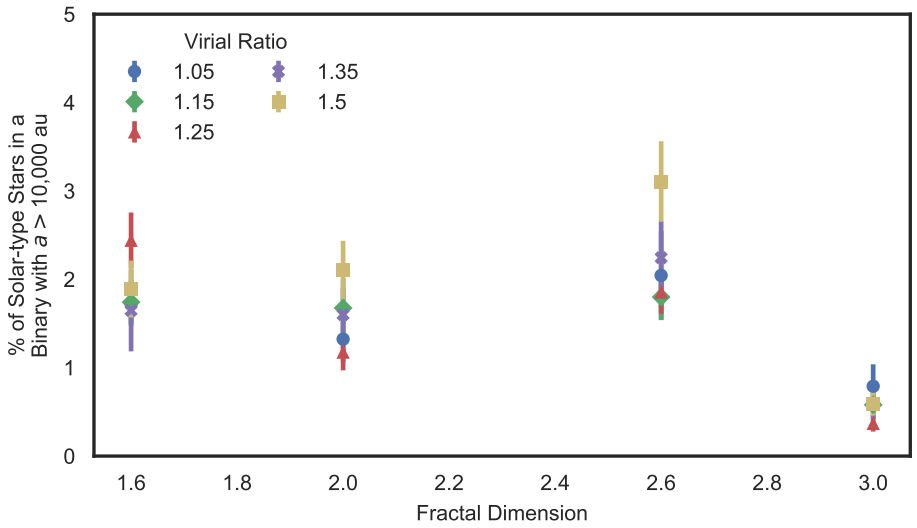

Figure 5.12: The mean (from 10 simulations) percentage of the number of *solar-type* stars (0.8-1.2 $M_\odot$) in a dispersing stellar association (stellar number $N = 5000$) which are in a very wide binary ($a > 10000$ AU) at $t = 25$ Myr, as a function of the initial fractal dimension of the association.

$M_\odot$) stars which are in a binary at the end of the simulation ($t = 25$ Myr), as a function of the the initial fractal dimension of the stellar association, for associations with $N = 5000$.

For solar-type stars, the most efficient initial conditions allow for $3.1\% \pm 0.5\%$ to form VWBs during the dissolution of a stellar region, fewer than the amount produced when $N = 500$.

The left-hand of Figure 5.13 shows the cumulative distribution of semi-major axes for each binary formed in all simulated dispersing stellar associations with total stellar number $N = 5000$ and fractal dimension $F_{\rm dim} = 1.6$, 2.0, 2.6 and 3.0. The right-hand of Figure 5.7 shows these cumulative distributions normalised by the total number of binaries in the associations. As with Figure 5.7, Figure 5.13 shows that the total number of binaries decreases as $F_{\rm dim}$ increases, yet the fraction of binaries which are VWBs increases.

5.3.3 Summary of Results

The main results, summarized from sections 5.3.1 and 5.3.2 are as follows:

1. 400 stellar associations are simulated, with $Q_{\rm vir} = 1.05$, ,1.15, 1.25, 1.35 and 1.5, $F_{\rm dim} = 1.6$, 2.0, 2.6 and 3.0 and N =500 and 5000.

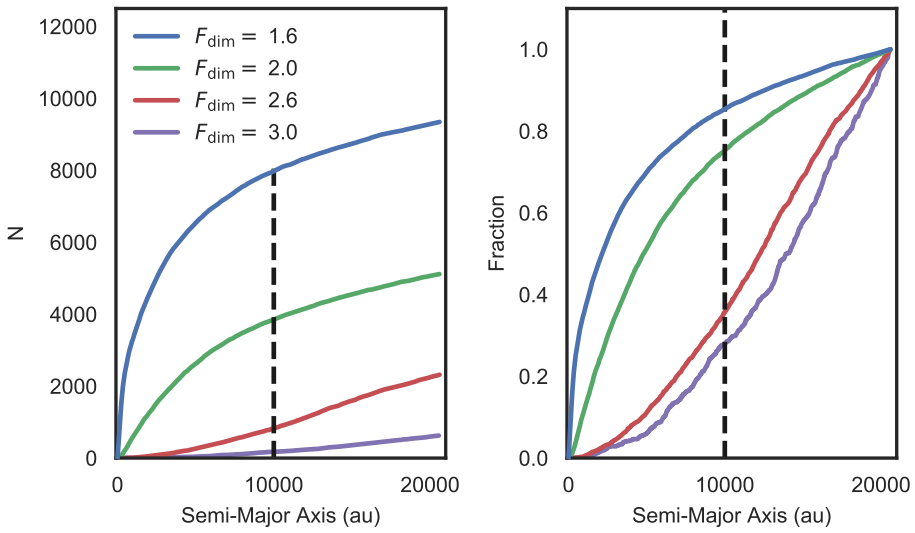

Figure 5.13: The cumulative distribution of semi-major axes for each binary formed in simulated dispersing stellar associations with total stellar number $N = 5000$ and fractal dimension $F_{\rm dim} = 1.6$, 2.0, 2.6 and 3.0. The right-hand plot shows the total number and the right-hand plot shows the normalised distribution. The dashed black line shows the lower limit ($a = 10000$ AU) for the semi-major axes of very wide binary systems.

2. For all simulations, the initial virial ratio $Q_{\rm vir}$ has a negligible effect on the percentage of stars which form binaries during the dispersal of the association.

3. The initial fractal dimension $F_{\rm dim}$ has a significant effect on the resultant percentage of stars in binary systems, with the percentage of stars in a binary decreasing as $F_{\rm dim}$ increases (Figures 5.4 and 5.10).

4. The total number of stars N also has a significant effect on the resultant percentage of stars in binary systems, with the percentage of stars in a binary decreasing as the N increases.

5. However, Figures 5.6 and 5.11 show that the percentage of stars in a VWB at $t = 25$ Myr does not simply decrease linearly with $F_{\rm dim}$, but instead there is a point at $F_{\rm dim} \sim 2.0$ for $N = 500$ after which the the percentage of stars in a VWB drop off. For $N = 5000$, this point has changed to $F_{\rm dim} \sim 2.6$.

6. Figures 5.7 and 5.13 show that, as $F_{\rm dim}$ increases, the total number of binaries decreases, but the proportion of these binaries which are VWBs increases.

7. Given the most accommodating initial conditions, the percentage of stars which

form a VWB during the dissolution of a stellar association is $3.0\% \pm 0.5\%$.

8. Given the most accommodating initial conditions, the percentage of *solar-type* stars which form a VWB during the dissolution of a stellar association is $7.8\% \pm 0.4\%$.

5.4 Discussion of Results

5.4.1 Fractal Dimension

The results of Sections 5.3.1 and 5.3.2 suggest that varying the initial fractal dimension $F_{\rm dim}$ affects the number of binaries which are present when the association has dispersed into the field, i.e. that the number of binaries decreases as $F_{\rm dim}$ increases. As $F_{\rm dim}$ is a way of quantifying the 'clumpiness' or degree of substructure in a region, and a lower value of $F_{\rm dim}$ signifies more substructure, the results therefore suggest that clumpier initial conditions in an association are more efficient at producing binaries than more diffuse initial conditions.

However, the relationship between $F_{\rm dim}$ and the number of stars in a VWB at $t = 25$ Myr is not so straightforward. For $N = 500$, there is a point at $F_{\rm dim} \sim 2.0$, after which the number of VWBs drop off significantly. For $N = 5000$, the position of this point is closer to $F_{\rm dim} \sim 2.6$. At values of $F_{\rm dim}$ lower than this point, the association is no more efficient at producing VWBs.

In addition, Figures 5.7 and 5.13 show that, as $F_{\rm dim}$ increases, the total number of binaries decreases, but the fraction of binaries which are VWBs increases.

One possible explanation for this is as follows: *more* clumpy initial conditions means that there are larger empty regions in the association on a macro level, but also a higher chance of close proximity to neighbours at the individual star level. This starting proximity to neighbours allows for a greater chance for binaries to form once the association has dispersed, and the smaller average separations between stars in each 'clump' will favour the formation of binaries with smaller separations.

Less clumpy initial conditions mean that the average separation between stars is greater, decreasing the number of binaries which form but increasing the average separation of the binaries which do form.

However, the degree of substructure in a region does not only affect binary formation, but it affects binary destruction as well. The encounter rate $f_{\rm enc}$ between systems in an association is proportion to the number of systems N, the number density n and the

velocity dispersion σ as:

$$f_{\rm enc} \propto Nn\sigma(1+\Theta) \tag{5.1}$$

where $\Theta \propto 1/\sigma^2$ is the Safronov gravitational focusing term (Binney & Tremaine, 1987). This shows that the chance of a VWB experiencing an encounter depends on both the number N and the number density n. While all associations began with the same initial *global* density, the initial fractal dimension will have an effect on the *local* density of different regions, affecting both formation and destruction of VWBs.

Chapter 1 showed that the likelihood that a binary will survive an encounter with a third star is proportional to its binary separation. A VWB has a wide separation and is therefore likely to be destroyed in any encounter with a third star. Hence there is a point in the degree of substructure, at which the number of VWBs can form, minus the number of VWBs which are destroyed, is greatest. After this point, more binaries form, but the VWBs are more likely to be destroyed in encounters and the binaries with smaller separations are more likely to survive. Before this point, fewer VWBs are destroyed in encounters but a smaller total number of binaries form.

5.4.2 Number of Stars

The results show that the total number of stars N can have a significant effect on the fraction of stars which are in a VWB after an association has dispersed into the Galactic field. Even though both $N = 500$ and $N = 5000$ associations had the same stellar number density ($n \approx 80$ stars pc^{-3}, the $N = 500$ associations were markedly more efficient at forming binaries, VWBs and VWBs with members with masses $0.8 < M_\star < 1.2$ M$_\odot$. Intuitively, one might expect regions with similar number densities to have a similar efficiency at producing VWBs, rather than a more numerous association being markedly less efficient. Equation 5.1 provides an explanation for why regions with larger N appear to contain fewer VWBs. Whether or not regions with larger N are more or less efficient in the production of VWBs, Equation 5.1 shows that encounters are more likely in regions with larger N. Because VWBs are so easily destroyed, any increase in the encounter rate $f_{\rm enc}$ translates in a decrease in the number of VWBs which will survive as the association disperses. Therefore it is likely that many more VWBs formed in the initial stages of the dispersal of the association, but were subsequently destroyed before they had the chance to escape into the Galactic field.

5.4.3 Virial Ratio

Intuitively, varying the virial ratio $Q_{\rm vir}$ of an association could have an effect on the formation of VWBs because it changes the timescale in which the association disperses. This would in turn change the timescale for which it is possible for two stars to interact *after* the region has dispersed enough for soft capture to occur, but *before* the stars are all separated to the point at which they only interact very weakly. In practice, Figure 5.3 shows that altering $Q_{\rm vir}$ has a negligible effect on the formation of VWBs. This gives rise to the possible conclusion that the initial virial ratio of the dispersing association is simply unimportant - two prospective VWB members that have the required dynamical properties will always form a VWB once the gravitational influence of the surrounding association is sufficiently negligible. Taking Equation 5.1 into account may help to explain why $Q_{\rm vir}$ appears to have no effect on the efficiency of binary formation in these simulations. The velocity dispersion σ is proportional to the virial ratio $Q_{\rm vir}$ as $\sigma \propto Q_{\rm vir}^{0.5}$ which means, as $Q_{\rm vir}$ increases, so does σ. The Safronov term Θ is proportional to σ^2 and so becomes negligible at large $Q_{\rm vir}$. But because the rate of encounters $f_{\rm enc}$ is also proportional to σ, the increased virial ratio should in turn increase the rate of encounters. Counteracting this is the fact that an increase in σ will cause the stellar number density n to decrease more rapidly.

5.5 Conclusion

Very wide binaries (VWBs) are defined as any binary system with a binary separation $a > 10000$ AU. Because of the size of their separation, it is currently unclear how VWBs could have formed primordially via fragmentation of a star forming core - the established method for forming binaries with much smaller separations. Because of their low binding energy, VWBs are easily destroyed in encounters with other stars and with the background Galactic mass distribution, meaning that their numbers must be continually replenished.

One possible mechanism for forming VWBs is the 'soft capture' mechanism. This chapter performs N-body simulations to investigate whether VWBs can be formed via the soft capture mechanism during the dissolution of clumpy, gravitationally unbound expanding stellar associations. The initial properties of the associations were varied - virial ratio $Q_{\rm vir}$ ($Q_{\rm vir} = 1.05$, 1.15, 1.25, 1.35 and 1.5), the fractal dimension $F_{\rm dim}$ ($F_{\rm dim} =$ 1.6, 2.0, 2.6 and 3.0) and the total stellar number N ($N =$500 and 5000) to produce 40 unique sets of initial conditions. 10 simulations were performed for each set of initial

conditions.

The results of the simulations show that the initial virial ratio $Q_{\rm vir}$ of the association has a negligible effect on the production of binaries or VWBs.

They show that the total number of binaries which form decreases as the initial fractal dimension $F_{\rm dim}$ increases, but that the number of VWBs as a function of $F_{\rm dim}$ peaks at $F_{\rm dim} \sim 2.0$ for $N = 500$ and $F_{\rm dim} \sim 2.6$ for $N = 5000$. This is explained as being due to the increased likelihood of encounters in low-$F_{\rm dim}$ regions which disrupt the weakly-bound VWBs while having a smaller effect on the number of binaries with smaller separations.

The results show that increasing the total number of stars N has a detrimental effect on the fraction of stars which are in a binary or a VWB, which is again explained by the increased encounter rate.

Future work may include finding a diagnostic which can help to pick apart the complex relationship between $F_{\rm dim}$, the formation of VWBs and the destruction of VWBs, possibly by running simulations with a large number of time snapshots and tracking the number, properties and lifetimes of binary systems over time - do more VWBs form for lower $F_{\rm dim}$ but most are destroyed? Do the lifetimes of the VWBs which form increase as a function of $F_{\rm dim}$?

5% of Galactic field G-dwarfs are members of a VWB. Since the *best* case scenario presented in this chapter results in $\sim 8\%$ of G-dwarfs becoming members of a VWB due to soft capture and the typical lifetime of a VWB field is less than 2 Gyr, this suggests that a *much* more efficient mechanism is needed to produce the required number of VWBs.

Chapter 6

The Uncoupling of the Dynamical Evolution of Stars and Gas in a Dense Cluster

6.1 Introduction

The investigations in Chapters 4 and 5 focus solely on young stellar regions which contain only stars and no gas. It is assumed in these investigations that the gas, which would normally account for a significant fraction of the total mass of a region, has been depleted via gas expulsion (see Section 1.3.7) and therefore the mass of the remaining gas is too small to have an impact on that region's evolution.

However, to gain a more comprehensive understanding of the dynamical evolution of young stellar regions, the impact of the gas component of the total mass must be taken into account. Therefore it is sometimes necessary to perform mixed simulations containing both stars and gas together to explore how a region behaves and evolves in totality.

Gas expulsion occurs due ionisation and due to the feedback of massive stars, in the form of supernovae and strong stellar winds. Section 1.3.7 and Hills (1980); Goodwin (1997); Kroupa et al. (2001) show that the effect of this loss of the cluster's gas component on the cluster's survival depends on the star formation efficiency (SFE) $\epsilon_{\rm sf}$ given by Equation 1.30.

However, Section 1.3.7 and Goodwin (2009) also show that the evolution of the cluster after gas expulsion is not just dependent on the SFE of a region, but is instead dependent on the *effective* SFE $\epsilon_{\rm esf}$, which takes into account the positions and velocities of the stars

and gas immediately prior to gas expulsion. Therefore, if the dynamical state of the stars and gas in a cluster varies prior to gas expulsion, then this can have an effect on the likelihood that the cluster will survive or disperse after gas expulsion.

One way that the dynamical state of a cluster can change over time is described by Aarseth et al. (1974). Let $R_{0.1}$, $R_{0.5}$ and $R_{0.9}$ be the 10%, 50% and 90% Lagrangian radii of the cluster respectively ($R_{0.5}$ is the cluster's half-mass radius). As a Plummer distribution of stars (no gas) evolves, the values of $R_{0.1}$ and $R_{0.9}$ diverge - $R_{0.1}$ increases and $R_{0.9}$ decreases while $R_{0.5}$ remains approximately constant (Aarseth et al., 1974). This is because the centre of the distribution evolves towards infinite density due to two-body relaxation, which transfers energy from the core to the outer regions - the core contracts and the outer regions expand.

However, a bound system which contains both stars and adiabatic gas will behave differently to a system which contains no gas. As with the no-gas example, two-body relaxation causes energy transfer from the centre of the cluster to its outer regions. This leads to the contraction of the core which heats up. This increase in thermal energy should cause the adiabatic gas in the core to expand. This in turn may lead to a core in which the gas mass is significantly depleted, without the need for gas expulsion. The effect of this purely dynamical gas depletion in the cluster core is to increase the value of $\epsilon_{\rm sf}$ even though the actual rate of star formation is much lower than this value of $\epsilon_{\rm sf}$ would indicate.

Hubber et al. (2013) showed that the half-mass radii of star and gas components of a cluster may diverge as a function of time, but did not investigate this further. This chapter investigates in more detail how the star and gas components of a dense cluster interact due to gravity, and the differences in the dynamical evolution of the stars and gas. This is studied with simulations containing both N-body and SPH particles to simulate the stars and gas, with dense clusters whose initial properties are varied in order to study their effect on the interplay of stars and gas. Section 6.2 focuses on the initial conditions of the simulations which need to be generated to model regions with varied initial properties. Section 6.3 shows the results of the simulations performed, which are then discussed in Section 6.4, before conclusions are drawn in Section 6.5.

6.2 Method and Initial Conditions

The simulations in this chapter investigate the interplay between the dynamical evolution of the stellar component of a dense cluster and the dynamical evolution of the gas

SPH Parameter	Implementation
Time integrator	Leapfrog KDK
Smoothing kernel	m4 cubic spline
Artificial viscosity	Monaghan (1997)
Viscosity constants	$\alpha = 1.0$; $\beta = 2.0$
Equation of state	Energy equation
Ratio of specific heats	$\gamma = 5/3$
Tree algorithm	Barnes-Hut (Barnes & Hut, 1986)

Table 6.1: The SPH parameters used for integration of the gas in the simulation of the dynamical evolution of dense, gas-rich clusters.

component. The simulations intend to illustrate the 'decoupling' of the evolution of the stars and the evolution of the gas due to the contraction of a cluster core, and show how the cluster's apparent core star formation efficiency can lead to inaccurate conclusions regarding how much star formation has occurred and the likelihood of survival after gas expulsion.

To achieve these goals, numerical simulations of clusters with both stars and gas were performed, using the hybrid N-body/SPH code GANDALF (Hubber et al., 2013). Each simulated cluster consists of 50% (by mass) 'N-body' particles and 50% SPH particles (we call the star particles 'N-body' particles for simplicity, yet they can also be described as SPH particles which have been modified to behave closer to N-body particles - see Section 3.4.5). The method for performing hybrid N-body/SPH simulations is described in Section 3.4.5. The integration scheme used for the N-body particles is the familiar fourth-order Hermite scheme used in Chapters 4 and 5, and the second-order leapfrog KDK scheme from Section 3.4.1 is used to integrate the SPH particles, for which the M4 cubic spline smoothing kernel (Monaghan & Lattanzio, 1985) is used, with artificial viscosity given by Monaghan (1997). The SPH integration scheme used is the *grad-h* SPH method from Price & Monaghan (2007) and described in Section 3.3. The SPH parameters used are summarised in Table 6.1.

All of the simulated clusters are allocated an initial total mass 1000 $M_\odot$, with 500 $M_\odot$ consisting of stars and 500 $M_\odot$ consisting of adiabatic gas. This gives a value of the initial star formation efficiency as $\epsilon_{\rm sf} = 0.5$. All of the simulated clusters were given an initial virial ratio $Q_{\rm vir} = 0.5$, so that they begin in virial equilibrium.

6.2.1 Positions and Velocities

The positions and velocities of the N-body particles are allocated by randomly sampling the Plummer distribution and then scaling the velocities according to the virial ratio, using the method described in Section 2.7.4.

Similar to the N-body particles, the positions of the SPH particles are allocated by randomly sampling the Plummer distribution. The velocities, however, are set to zero. The gas is modelled as an $n = 5$ polytrope and and the particles are instead allocated an internal thermal energy given by $u(r)$ using the method described in Section 3.4.4.

6.2.2 Half-mass Radius

The initial half-mas radius $R_{i,0.5}$ of the cluster is either $R_{i,0.5} = 0.25$ pc or $R_{i,0.5} = 0.50$ pc. A Plummer distribution has a density profile given by Equation 2.25. Therefore, increasing the half-mass radius decreases the mass density and the stellar number density of the cluster. Decreasing the density in turn increases the cluster's crossing time $t_{\rm cr}$ - using Equation 1.24 gives a value of $t_{\rm cr}$ for $R_{i,0.5} = 0.50$ pc ~ 3 times larger than that for $R_{i,0.5} = 0.25$ pc. Hence it is necessary to vary the initial half-mass radius to measure its effect on the dynamical evolution of the cluster.

6.2.3 Number of Particles

The number of N-body particles (denoted $N_\star$) is varied from $N_\star = 100$ to $N_\star = 200$. Doubling the number of stars in the region doubles the region's stellar number density, increasing the likelihood of encounters between stars. As the total stellar mass remains at $M_\star = 500$ M$_\odot$, the masses of the individual stars are decreased from $m_\star = 5$ M$_\odot$ to $m_\star = 2.5$ M$_\odot$, meaning that the strength of any individual interaction is decreased.

The number of SPH particles (denoted N_g) is also varied. When $N_\star = 100$, N_g is varied from $N_g = 1000$ to $N_g = 10000$. When $N_\star = 200$, N_g is varied from $N_g = 2000$ to $N_g = 20000$. This means that the ratio of the number of SPH particles to the number of N-body particles varies from $N_g/N_\star = 10$ to $N_g/N_\star = 100$. In a hybrid SPH/N-body simulation, it is necessary that the number of SPH particles is appreciably larger than the number of N-body particles to minimise unphysical collisions between N-body and SPH particles. Varying the ratio of $N_g/N_\star$ can give us insight into the extent of these numerical effects.

Varying the numbers of N-body particles also affects the cluster's two-body relaxation timescale $t_{\rm r}$ (see Section 1.3.2). Equation 1.26 shows that a cluster of stars with $N_\star = 200$

will have a value of $t_{\rm r}$ which is ~ 1.7 times the value of $t_{\rm r}$ for a cluster with $N_\star = 100$. Hence changing the values of $N_\star$ and N_g may allows us to study how these parameters affect the cluster's dynamical evolution.

6.2.4 Mass Function

The distribution of stellar masses in a region will affect the region's dynamical evolution (e.g. mass segregation - see Section 1.3.4) Therefore the mass function of the N-body particles is varied. Firstly, a flat mass function is used with the N-body particles having equal masses $m_\star = M_\star/N_\star$. When $N_\star = 100$, $m_\star = 5$ M$_\odot$ and, when $N_\star = 200$, $m_\star = 2.5$ M$_\odot$.

The flat mass function is replaced by an IMF from Maschberger (2013) by allocating a mass to each star using the method outlined in Section 2.7.3. In addition to the fact that observations of clusters shown that they have an IMF, adding stars with non-equal masses will affect the dynamical evolution of the cluster and may lead to dynamical mass segregation, increased rate of stellar evaporation or the formation of a massive binary. Contrary to the mass function for the N-body particles, the mass function for the SPH particles is kept flat, as is typically the case for SPH simulations.

6.2.5 Summary of Initial Conditions

Table 6.2 summarises all of the different sets of initial conditions. 16 sets of initial conditions were used to set up the simulations, by altering the initial values of $N_\star$, N_g, $R_{0.5}$ and by changing between a flat mass distribution and a distribution using the Maschberger IMF. For ease of reference, each set of initial conditions is allocated a name, from Investigation 1.1 to Investigation 4.4. The results of these simulations are presented in the next section.

Investigation	$N_\star$	N_g	$R_{0.5}$ (pc)	Mass Function	$t_{\rm cr}$ (Myr)
1.1	100	1000	0.25	Flat	0.08
1.2	100	10000	0.25	Flat	0.08
1.3	100	1000	0.50	Flat	0.22
1.4	100	10000	0.50	Flat	0.22
2.1	100	1000	0.25	Maschberger	0.08
2.2	100	10000	0.25	Maschberger	0.08
2.3	100	1000	0.50	Maschberger	0.22
2.4	100	10000	0.50	Maschberger	0.22
3.1	200	2000	0.25	Flat	0.08
3.2	200	20000	0.25	Flat	0.08
3.3	200	2000	0.50	Flat	0.22
3.4	200	20000	0.50	Flat	0.22
4.1	200	2000	0.25	Maschberger	0.08
4.2	200	20000	0.25	Maschberger	0.08
4.3	200	2000	0.50	Maschberger	0.22
4.4	200	20000	0.50	Maschberger	0.22

Table 6.2: Showing the different sets of initial conditions for the hybrid N-body/SPH simulations of cluster containing both stars and gas. The different sets are each given a name for ease of reference, from Investigation 1.1 to Investigation 4.4.

6.3 Results

Although ensembles of simulations with randomised parameters would allow us to account for stochasticity, due to computation constraints we perform 16 hybrid N-body/SPH simulations; one simulation for each of the sets of initial conditions shown in Table 6.2.

6.3.1 Investigation 1.1

Investigation 1.1 simulated a small ($N_\star = 100$, $N_g = 1000$), dense ($R_{0.5} = 0.25$ pc) cluster containing equal-mass ($m_\star = 5$ M$_\odot$) stars, for 5 Myr. The Lagrangian radii ($R_{0.1}$, $R_{0.5}$ and $R_{0.9}$) were calculated separately for the star particles and the gas particles as a function of time. For clarity, the Lagrangian radii for the stars are denoted $R_{\star,0.1}$, $R_{\star,0.5}$ and $R_{\star,0.9}$ and the Lagrangian radii for the gas are denoted $R_{g,0.1}$, $R_{g,0.5}$ and $R_{g,0.9}$.

Figure 6.1 shows $R_{0.1}$, $R_{0.5}$ and $R_{0.9}$ for the stars (blue) and the gas (orange) as a function of time for Investigation 1.1. The inner Lagrangian radii of the stellar component have decreased over time - $R_{\star,0.1}$ has decreased from 0.13 pc to 0.06 pc and $R_{\star,0.5}$ has decreased from 0.25 pc to 0.17 pc, a reduction to 46% and 68% of their initial values respectively - while $R_{\star,0.9}$ has increased slightly from 0.33 pc to 0.36 pc. Within the same

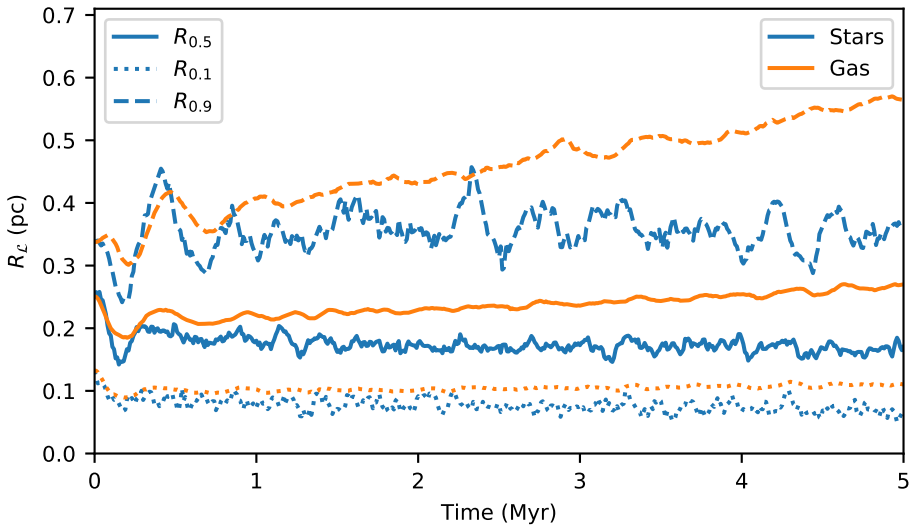

Figure 6.1: The Lagrangian radii $R_{0.1}$, $R_{0.5}$ and $R_{0.9}$ for the stars (blue) and gas (orange) in a dense cluster, as a function of time for Investigation 1.1. The Lagrangian radii of the stars and gas diverge over time.

time-frame, the value of $R_{g,0.1}$ for the gas component has also decreased only slightly, from 0.13 pc to 0.11 pc, while the $R_{g,0.5}$ and $R_{g,0.9}$ values have increased, the $R_{0.9}$ value by 167% of its initial value.

In order to examine the difference in the final distributions of stars and gas in the cluster, it is useful to define the ratio $\mathcal{R}_\alpha$:

$$\mathcal{R}_\alpha = \frac{R_{\star,\alpha}}{R_{g,\alpha}} \tag{6.1}$$

where $\alpha = 0.1$, 0.5 and 0.9 and the Lagrangian radii for the stars and the gas are evaluated at $t = 5$ Myr. Calculating these ratios for Investigation 1.1 gives the values $\mathcal{R}_{0.1} = 0.56$, $\mathcal{R}_{0.5} = 0.63$ and $\mathcal{R}_{0.9} = 0.64$ (see Table 6.3). This shows that that the final stellar Lagrangian radii have diverged significantly from the final gas Lagrangian radii. In other words, half of the cluster's stellar mass at 5 Myr is within a radius which is only 63% of the final half-mass radius of the gas.

The divergence between the Lagrangian radii of the stellar component and that of the gas component implies that energy has transferred from the stars to the gas, causing the gas to heat up and expand. Figure 6.2 shows the total energy $E = \Omega + T$ for the stellar and gas components of the cluster as a function of time. It shows that the total energy of the stars $E_\star$ has decreased by the same amount that the total energy of the

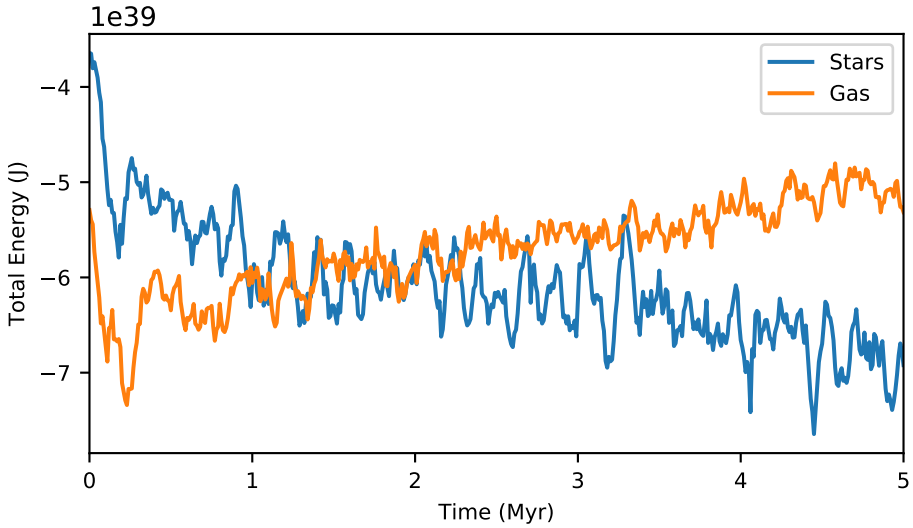

Figure 6.2: The total energy $E = \Omega + T$ for the stellar and gas components of the cluster as a function of time.

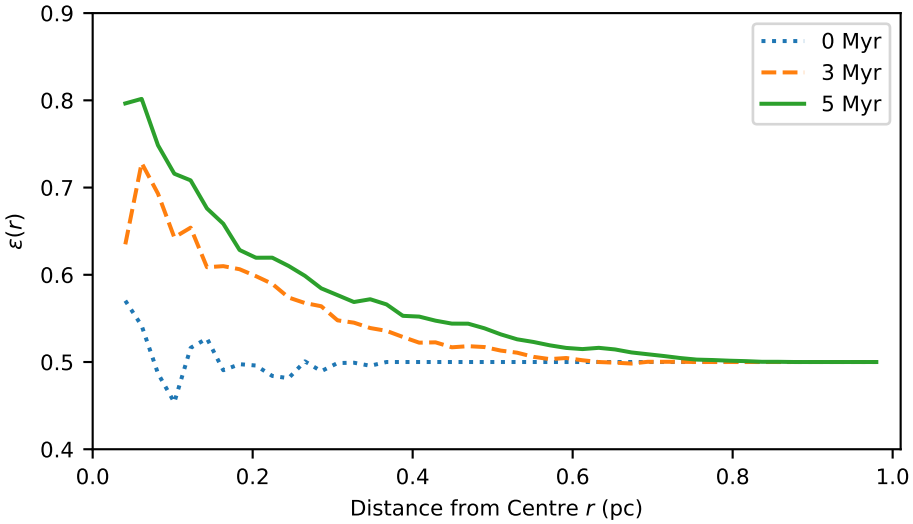

Figure 6.3: The effective star formation efficiency $\epsilon_{\rm sf}(r)$ given by Equation 1.30 as a function of the distance r from the cluster centre of mass, at times $t = 0$ Myr, 3 Myr and 5 Myr.

gas E_g has increased. While this is not surprising due to conservation of energy, it also clearly shows the transfer of energy from the stars in the cluster to the gas at the same time as the stellar component of the cluster core contracts.

Figure 6.3 shows the star formation efficiency $\epsilon_{\rm sf}(r)$ given by Equation 1.30 as a function of the distance r from the cluster centre of mass, at times $t = 0$ Myr, 3 Myr and 5 Myr. Figure 6.3 clearly shows that $\epsilon_{\rm sf}(r)$ increases over time, and that the increase is larger towards the centre of the cluster (when r is small), relative to the outskirts of the cluster (when r is large). This appears to support the conclusion that the transfer of energy from the stars to the gas has caused the gas to deplete in the core of the cluster. As no stellar feedback or accretion was modelled in any of these simulations, the phenomenon of core gas depletion is solely due to gravitational interactions between the stars. This also shows that the likelihood of the cluster being destroyed by gas expulsion from stellar winds or supernovae has decreased over time as the effective SFE has increased, i.e. the mass of gas in the cluster centre is no longer so significant that its rapid removal will cause the cluster to become gravitationally unbound.

6.3.2 Investigations 1.2, 1.3 and 1.4

The impact of the cluster's initial properties on the effect shown in Investigation 1.1 was studied in Investigations 1.2, 1.3 and 1.4, by performing simulations with different initial conditions. The number of gas particles was changed from $N_g = 1000$ to $N_g = 10000$ for Investigations 1.2 and 1.4, and the initial cluster half-mass radius was changed from $R_{\rm i,0.5} = 0.25$ pc to $R_{\rm i,0.5} = 0.50$ pc for Investigations 1.3 and 1.4.

Figure 6.4 shows $R_{0.1}$, $R_{0.5}$ and $R_{0.9}$ for the stars (blue) and the gas (orange) as a function of time for Investigations 1.1, 1.2, 1.3 and 1.4. The top-right of Figure 6.4 shows the results for Investigation 1.2 ($R_{i,0.5} = 0.25$ pc; $N_g = 10000$). The chance in the stellar Lagrangian radii is similar to that found in Investigation 1.1. However, the value of $R_{g,0.9}$ for the gas component has increased by ~ 3 times its initial value - twice the increase shown in Investigation 1.1. Investigation 1.2 gives values for the ratios $\mathcal{R}_{0.1}$, $\mathcal{R}_{0.5}$ and $\mathcal{R}_{0.9}$ as 0.66, 0.57 and 0.39 respectively.

The reason for the increase in the final value of $R_{g,0.9}$ for $N_g = 10000$ is an effect of increasing the gas resolution and the fact that the cluster is in a vacuum. The SPH particles in the simulation cause an outward pressure into the vacuum which is not counteracted by any inward pressure form the vacuum. This outward pressure increases as the interactions between gas particles increases (and therefore as N_g increases), causing the gas to expand into the vacuum.

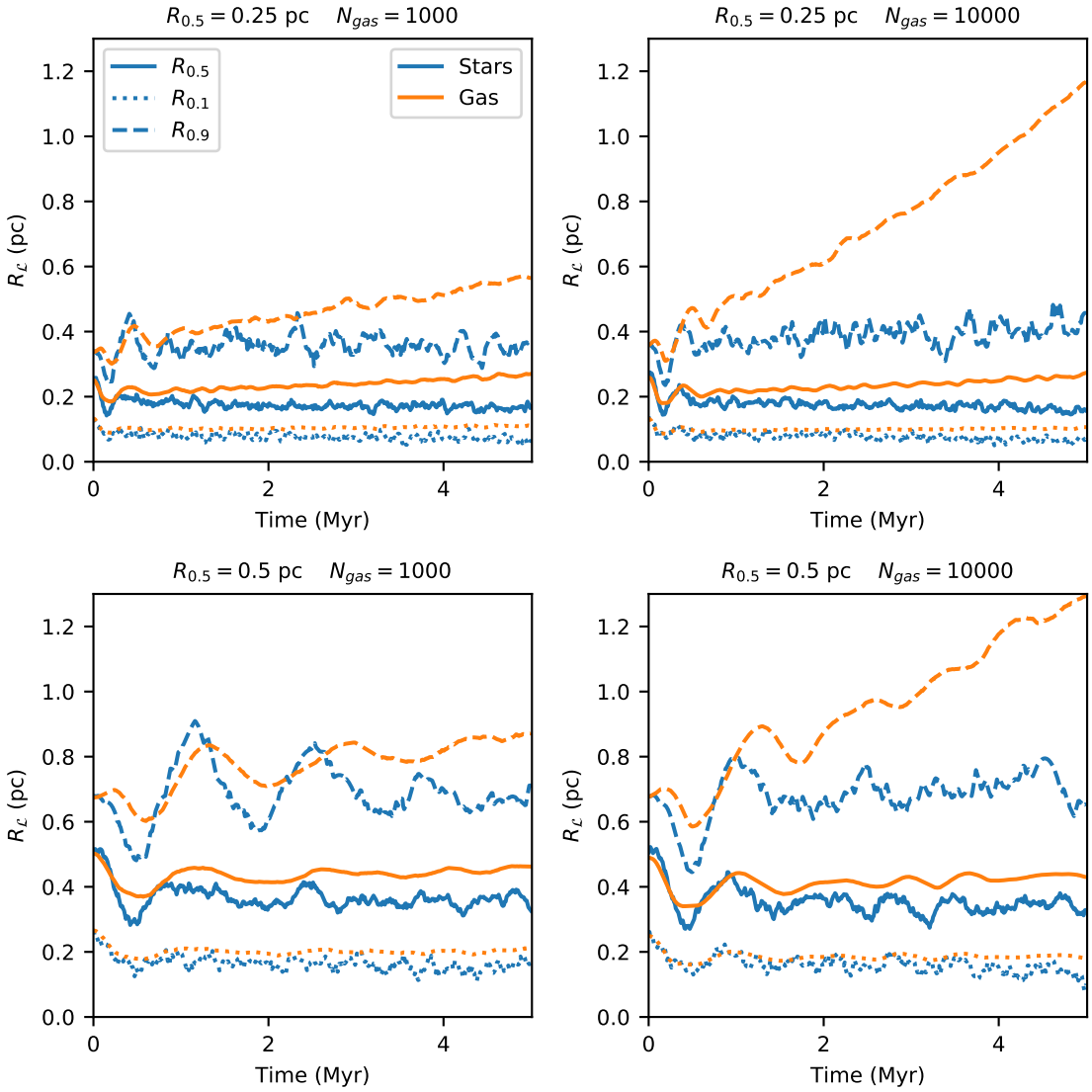

Figure 6.4: The $R_{0.1}$, $R_{0.5}$ and $R_{0.9}$ for the stars (blue) and the gas (orange) as a function of time for Investigation 1.1 (top-left), 1.2 (top-right), 1.3 (bottom-left) and 1.4 (bottom-right).

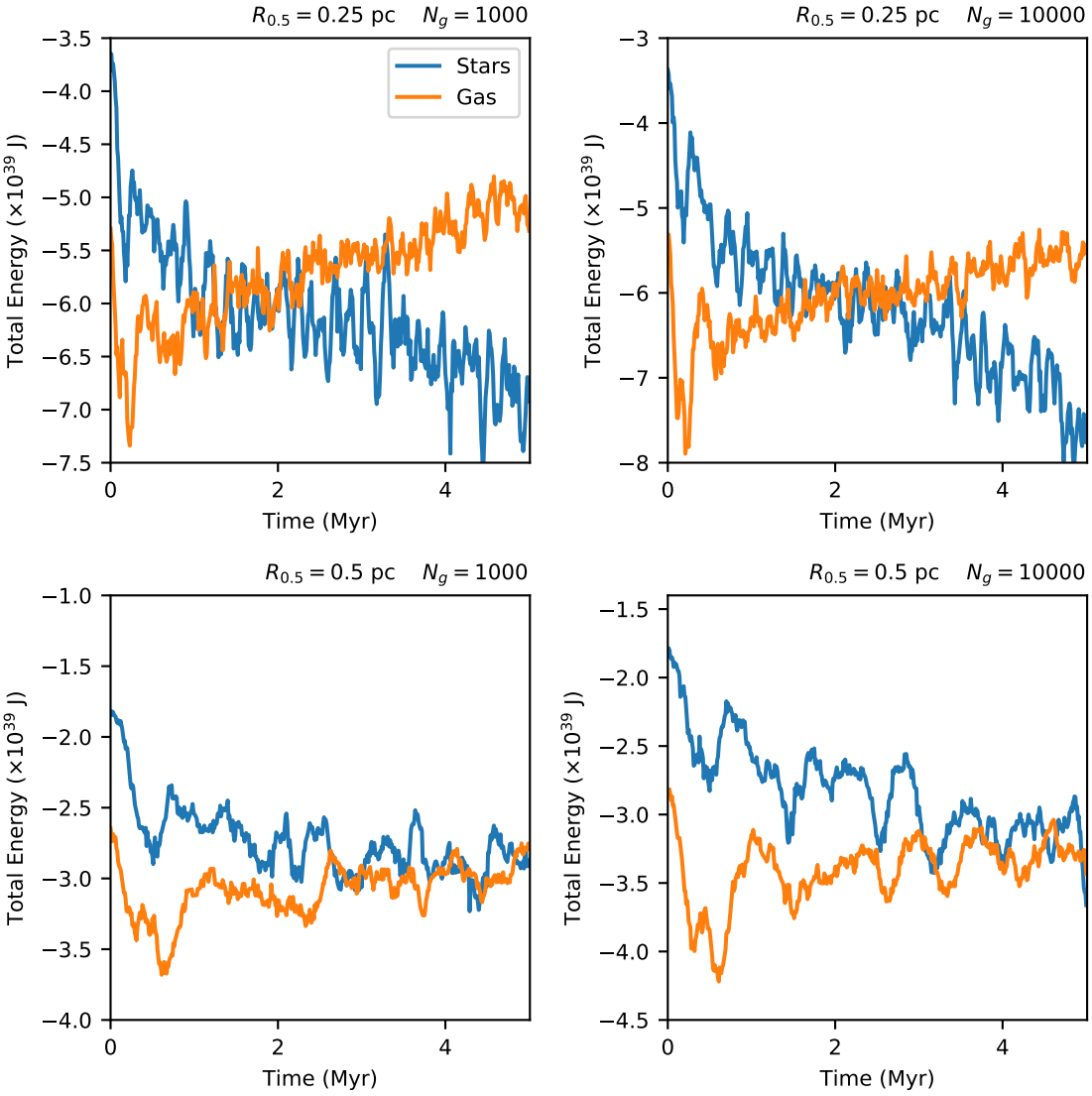

Figure 6.5: The total energy $E = \Omega + T$ for stars and gas as a function of time for Investigations 1.1 (top-left), 1.2 (top-right), 1.3 (bottom-left) and 1.4 (bottom-right).

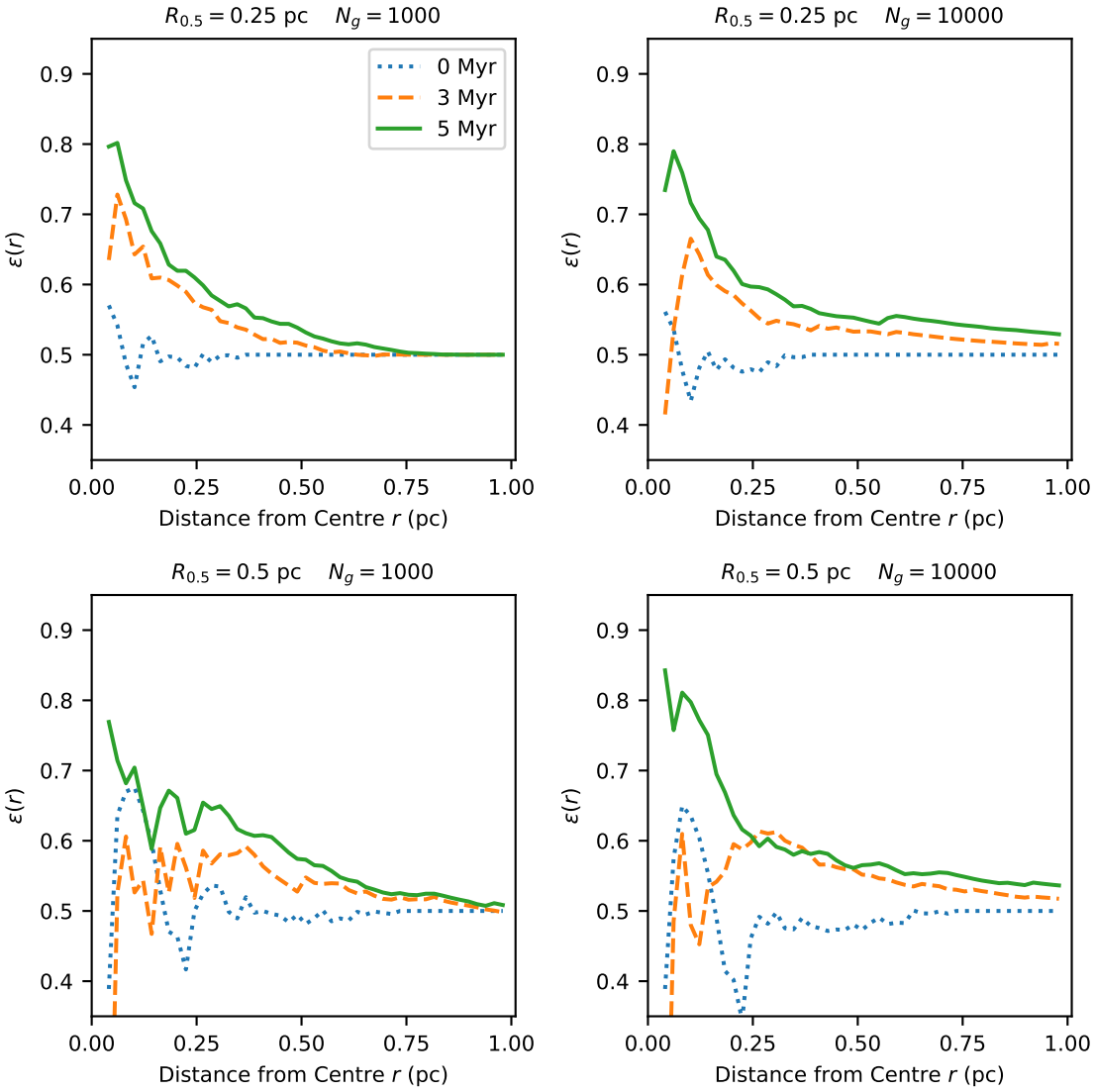

Figure 6.6: The star formation efficiency $\epsilon_{\rm sf}(r)$ given by Equation 1.30 as a function of the distance r from the cluster centre of mass, at times $t = 0$ Myr, 3 Myr and 5 Myr, for Investigations 1.1 (top-left), 1.2 (top-right), 1.3 (bottom-left) and 1.4 (bottom-right).

Bottom-left of Figure 6.4 shows the results of Investigation 1.3 ($R_{i,0.5} = 0.50$ pc; $N_g = 1000$) and bottom-right shows the results of Investigation 1.4 ($R_{i,0.5} = 0.50$ pc; $N_g = 10000$). For Investigation 1.3, the resultant values of $\mathcal{R}$ are $\mathcal{R}_{0.1} = 0.82$, $\mathcal{R}_{0.5} = 0.71$ and $\mathcal{R}_{0.9} = 0.81$, results which are similar to the results of Investigation 1.1, but the size of the effect has decreased. For Investigation 1.4, the resultant $\mathcal{R}$ values are $\mathcal{R}_{0.1} = 0.57$, $\mathcal{R}_{0.5} = 0.76$ and $\mathcal{R}_{0.9} = 0.50$, results that are similar to the results of Investigation 1.2 in that the increased resolution of the gas particles has caused the value of $\mathcal{R}_{0.9}$ to expand but again, the size of the effect has decreased compared to Investigation 1.1. This implies that increasing the initial cluster half-mass radius still produces the expected effect of decreasing the amount of gas found in the cluster's core, but it increases the time-frame in which this effect occurs. This can be seen more clearly in Figure 6.5, which shows the total energy $E = \Omega + T$ for stars and gas as a function of time for each of the four Investigations 1.1 to 1.4.

When the initial half-mass radius $R_{i,0.5} = 0.25$ pc (top-left and top-right of Figure 6.5), the rate of energy transfer from the stellar component to the gas component appears to be at least double the rate when $R_{i,0.5} = 0.50$ pc (bottom-left and bottom-right). This can be understood in the context of the crossing time $t_{\rm cr}$ being increased as the density is decreased - the value of $t_{\rm cr}$ has more than doubled from ~ 0.08 Myr to ~ 0.22 Myr (see Table 6.2), resulting in a subsequently longer time-frame for the dynamical evolution of the cluster, while not changing the *path* of that evolution.

Figure 6.6 shows the star formation efficiency $\epsilon_{\rm sf}(r)$ given by Equation 1.30 as a function of the distance r from the cluster centre of mass, at times $t = 0$ Myr, 3 Myr and 5 Myr, for each of the Investigations 1.1 to 1.4. In each investigation, $\epsilon_{\rm sf}(r)$ increases over time as the core contracts, in keeping with the results from Investigation 1.1. For Investigations 1.2 (bottom-left) and 1.4 (bottom-right), the value for $\epsilon_{\rm sf}(r)$ within the central 0.2 pc at 0 Myr overlaps with that at 3 Myr. This is likely an artefact of the initial conditions in which the core star and gas distributions are not precisely overlapping, but this discrepancy is quickly erased due to dynamical processing.

Figure 6.6 shows the primary conclusion to draw from Investigations 1.1 to 1.4 - dynamical interactions between the stars and gas in a dense cluster has removed the core gas component without the need for feedback-driven gas expulsion. This has produced an artificially inflated apparent core star formation efficiency which has no connection to how efficiently the core can really form stars, and will change the likelihood that the cluster will survive following gas expulsion.

6.3.3 Investigation 2

The sets of initial conditions used to simulate the clusters in Investigation 2 differ from those in Investigation 1 by the introduction of a Maschberger IMF in place of the flat, 5 $M_\odot$ stellar mass distribution used previously.

Figure 6.7 shows $R_{0.1}$, $R_{0.5}$ and $R_{0.9}$ for the stars (blue) and the gas (orange) as a function of time for Investigations 2.1, 2.2, 2.3 and 2.4. The results of Investigations 2.2 (top-right), 2.3 (bottom-left) and 2.4 (bottom-right) appear to agree with the results of Investigations 1.1 to 1.4 - the final values of the Lagrangian radii for the gas component are appreciably larger than those for the stellar component, although they vary in the size of the effect. The ratios of the final stellar half-mass radii to the final gas half-mass radii $\mathcal{R}_{0.5}$ for Investigations 2.2, 2.3 and 2.4 are 0.66, 0.56 and 0.60 which are similar to the values 0.70, 0.57 and 0.76 for Investigations 1.2, 1.3 and 1.4. This seems to show that changing the initial mass distribution has a negligible effect on the result, while also showing that the phenomenon does not disappear when a more 'realistic' mass function (i.e. a mass function which is closer to that which is observed in clusters) is used.

Plotting the results for Investigation 2.1 (top-left) shows an unusual feature not observed in Investigation 1 - a kink in the cluster's Lagrangian radii at ~ 4 Myr. Moreover, this is observed for both the stellar and gas components. This effect is shown more clearly in Figure 6.8, which shows the star formation efficiency $\epsilon_{\rm sf}(r)$ given by Equation 1.30 as a function of the distance r from the cluster centre of mass, at times $t = 0$ Myr, 3 Myr and 5 Myr, for each of the Investigations 2.1 to 2.4. At 5 Myr for Investigation 2.1 (top-right), the $\epsilon_{\rm sf}(r)$ values for the central ~ 0.4 pc of the cluster has declined significantly. This behaviour is unique to Investigation 2.1, and appears to be caused by an event occurring at ~ 4 Myr.

The introduction of a Maschberger IMF means that there can be high-mass stars which can affect the evolution of the cluster through their dynamical interactions with other stars. One process that can occur is the formation of a binary system consisting of two high-mass stars. This effect has been observed by Allison et al. (2010). A binary with a high-mass primary and secondary can have a binding energy which is comparable to the total gravitational potential energy of the whole of the cluster. When two massive stars come together to form a binary, this drastically decreases the effective magnitude of the gravitational potential energy of the rest of the cluster, causing it to expand rapidly. Therefore, the formation of a massive binary at ~ 4 Myr would help to explain the unique behaviour observed in Investigation 2.1.

Figure 6.9 shows the separation in AU as a function of time between two massive

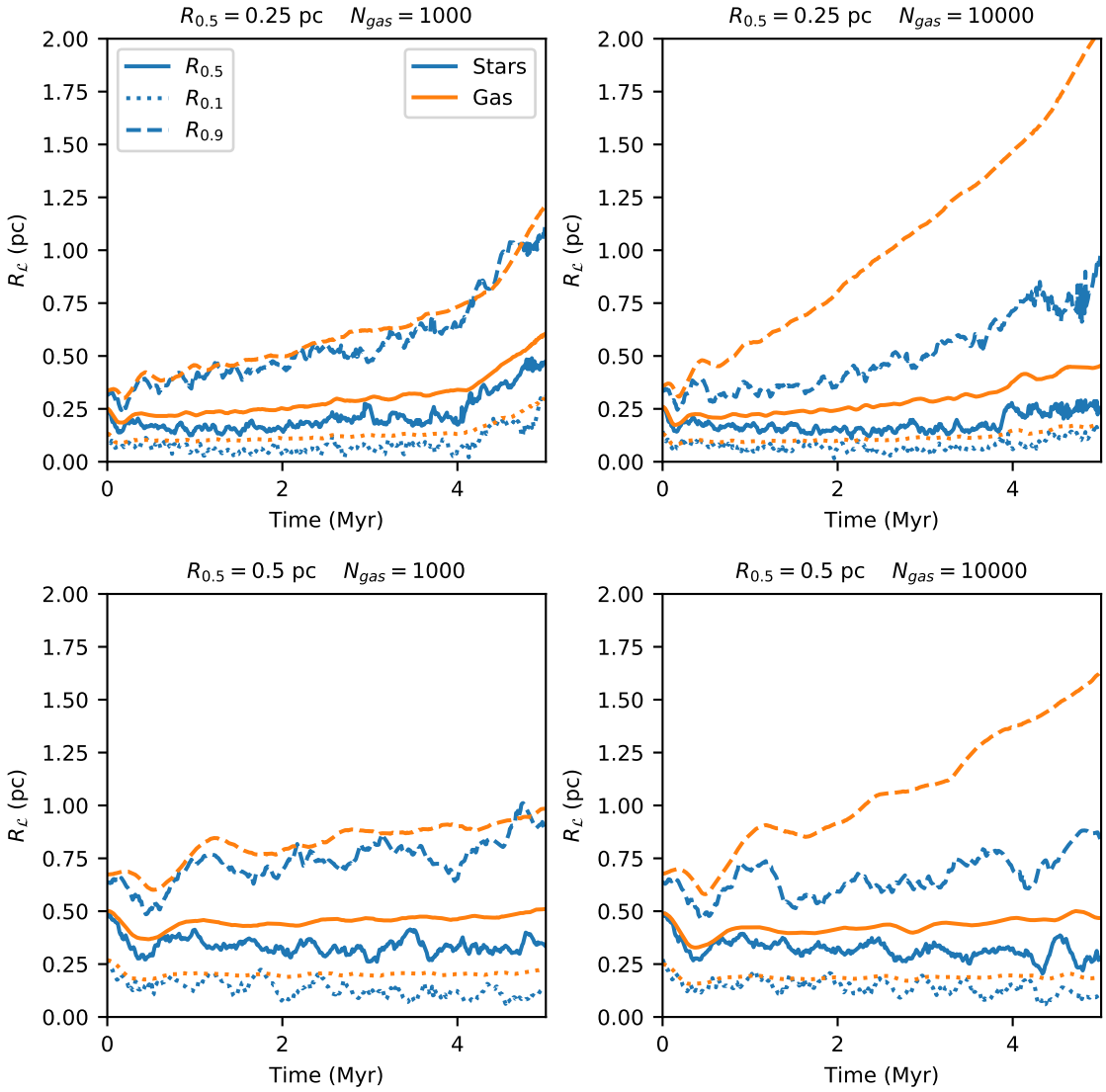

Figure 6.7: The $R_{0.1}$, $R_{0.5}$ and $R_{0.9}$ for the stars (blue) and the gas (orange) as a function of time for Investigation 2.1 (top-left), 2.2 (top-right), 2.3 (bottom-left) and 2.4 (bottom-right).

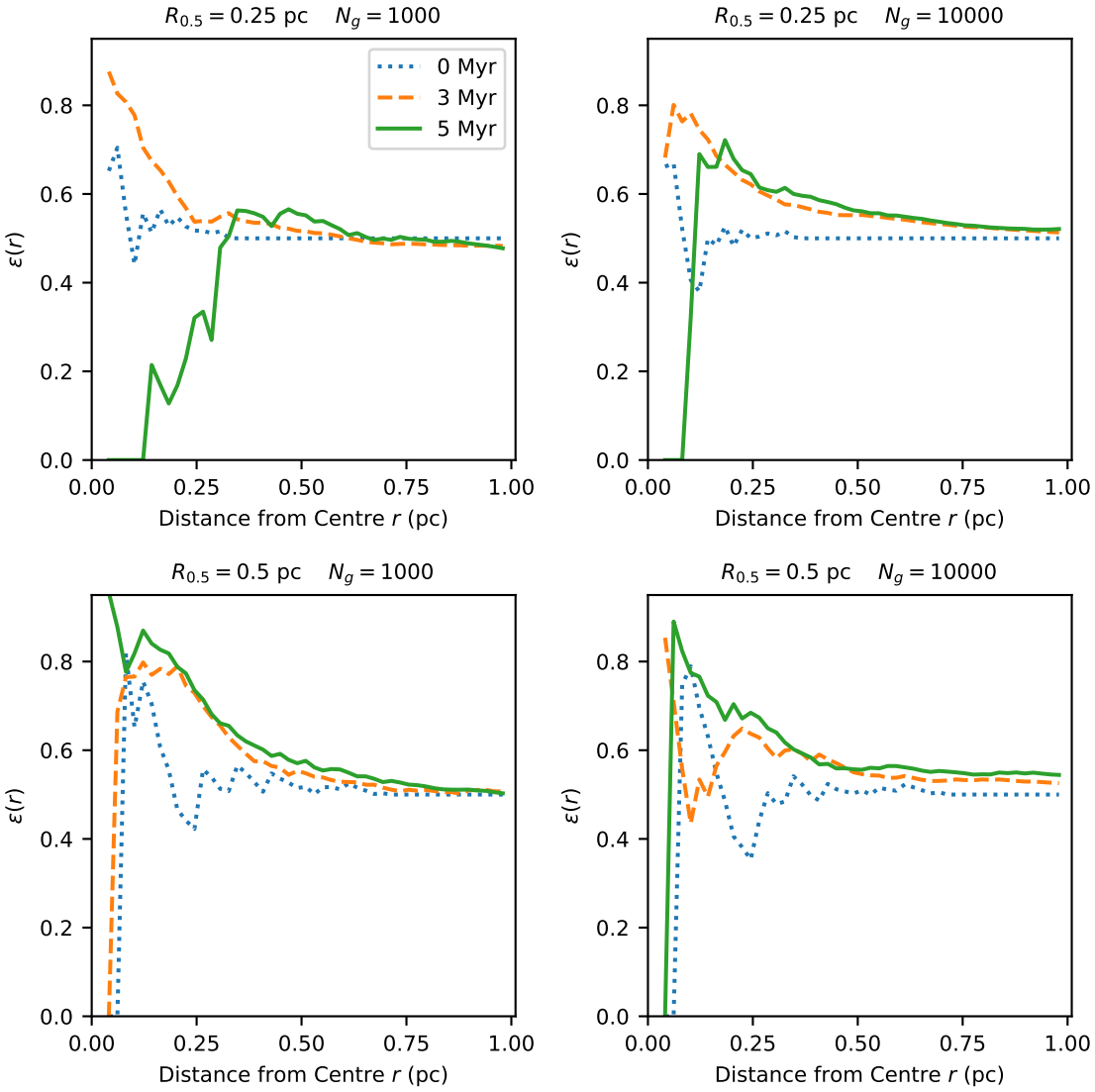

Figure 6.8: The star formation efficiency $\epsilon_{\rm sf}(r)$ given by Equation 1.30 as a function of the distance r from the cluster centre of mass, at times $t = 0$ Myr, 3 Myr and 5 Myr, for Investigations 2.1 (top-left), 2.2 (top-right), 2.3 (bottom-left) and 2.4 (bottom-right).

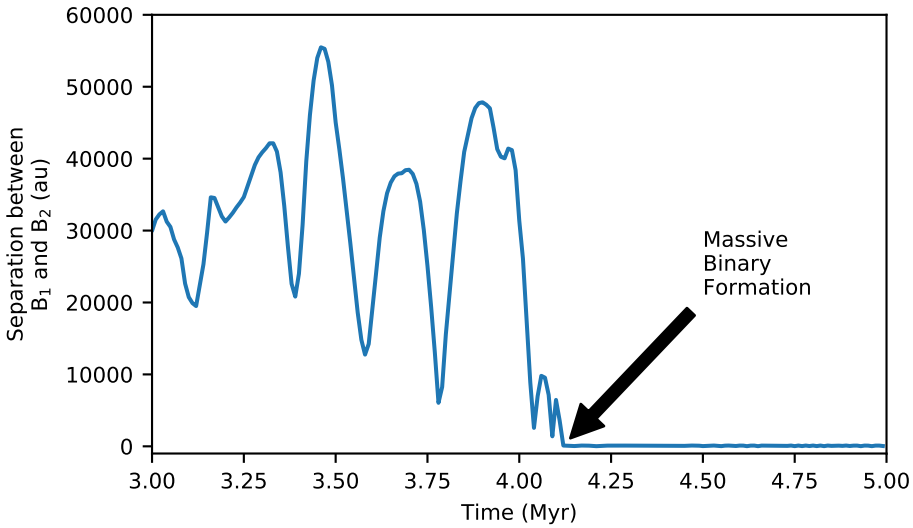

Figure 6.9: The separation between two high-mass stars (labelled B_1 and B_2) with masses of 22.6 $M_\odot$ and 19.3 $M_\odot$ respectively, showing their formation of a binary system at time $t \sim 4.12$ Myr.

stars in the cluster, denoted B_1 and B_2. From Figure 6.9 it is possible to see that the separation between B_1 and B_2 rapidly decreases to ~ 64 AU, where it remains stable for the duration of the simulation. B_1 has a mass of 22.6 $M_\odot$, making it the most massive star in the cluster. B_2 has a mass of 19.3 $M_\odot$, making it the second most massive star in the cluster. When these two stars dynamically form a massive, hard binary system, the magnitude of their binding energy is of the order $\sim 10^{39}$ J, which is of the order of the total energy of the rest of the cluster. Hence, when the binary forms, it acts like an energy sink, causing the magnitude of the energy of the cluster as a whole to decrease and thereby causing the cluster to become globally gravitationally unbound and to expand dramatically, thus causing the phenomenon seen in Figures 6.7 and 6.8.

Another effect seen in Figure 6.8 is the large fluctuations in the value of $\epsilon_{\rm sf}(r)$ at low r. The addition of a mass function does not just cause the potential formation of a massive binary as observed in Investigation 2.1, but also causes mass segregation and evaporation.

The $\Lambda_{\rm MST}$ parameter which attempts to quantify the amount of mass segregation in a cluster (see Section 1.3.4 for more details) for Investigations 1 and 2 is shown in Table 6.3. Because Investigation 1 only contains equal-mass stars, the $\Lambda_{\rm MST}$ parameter is equal to unity. For Investigation 2, the $\Lambda_{\rm MST}$ is close to unity at $t = 0$ Myr, but has increased to $\sim 1.3 - 1.5$ by $t = 5$ Myr. This shows that the massive stars are in closer proximity

Investigation	$\mathcal{R}_{0.1}$	$\mathcal{R}_{0.5}$	$\mathcal{R}_{0.9}$	$\Lambda_{\rm MST}$
1.1	0.56	0.63	0.64	1.0
1.2	0.66	0.57	0.39	1.0
1.3	0.83	0.71	0.81	1.0
1.4	0.57	0.76	0.50	1.0
2.1	1.05	0.78	0.92	1.33 ± 0.01
2.2	0.80	0.56	0.48	1.45 ± 0.01
2.3	0.55	0.66	0.90	1.39 ± 0.01
2.4	0.48	0.60	0.52	1.52 ± 0.01

Table 6.3: Table showing the $\mathcal{R}_{0.1}$, $\mathcal{R}_{0.5}$ and $\mathcal{R}_{0.9}$ values, where $\mathcal{R}_{\alpha}$ is given by Equation 6.1, and the $\Lambda_{\rm MST}$ (i.e. mass segregation) parameter, for Investigations 1.1 to 2.4.

compared to the typical distance between stars, i.e. they have become dynamically mass segregated. This mass segregation should increase the effect of dynamical gas depletion as the massive stars collapse towards the core. This, in turn, causes the evaporation of stars, meaning that there are fewer stars in the core. These effects mean that the shape of $\epsilon_{\rm sf}(r)$ at low r in Figure 6.8 is highly dependent on the relative positions of the small number massive stars in the core, causing large fluctuations in its value.

6.3.4 Summary of Results from Investigations 1 and 2

Clusters with Plummer distributions comprised of 50% stars and 50% gas are simulated for 5 Myr. This was done to observe how the interplay between the stellar component and the gas component cause their Lagrangian radii to evolve in opposite ways, and to show how this affects cluster's apparent star formation efficiency $\epsilon_{\rm sf}(r)$. In order to see the effect of the cluster's initial properties on this phenomenon, the cluster's initial half-mass radius, number of SPH particles and initial mass distribution were varied.

With the exception of Investigation 2.1, the cluster's apparent star formation efficiency $\epsilon_{\rm sf}(r)$ increased over time. This is shown most clearly by Figures 6.6 and 6.8.

Table 6.3 shows that, again with the exception of Investigation 2.1, the final Lagrangian radii of the stars at 5 Myr was lower than the final Lagrangian radii of the gas. The magnitude of this difference varied for different sets of initial conditions and for the three different Lagrangian radii. For example, $\mathcal{R}_{0.9}$ appears smaller for Investigations 1.3, 1.4, 2.3 and 2.4, when the initial half-mass radius was increased to 0.5 pc.

When the stellar mass distribution is changed to a Maschberger IMF for Investigations 2.1 to 2.4, core gas depletion still occurs. The exception is Investigation 2.1, due to the effect of the formation of a massive, hard binary system which gravitationally

unbinds the cluster.

Dynamical mass segregation in the cores of the clusters in Investigation 2 causes the value of $\epsilon_{\rm sf}(r)$ to fluctuate. Simulations of clusters with higher values of $N_\star$ may help to mitigate this effect.

6.3.5 Investigation 3

For investigation 3, the number of star particles is increased from $N_\star = 100$ to $N_\star = 200$. The corresponding number of gas particles is varied between $N_g = 2000$ and $N_g = 20000$. Otherwise, Investigation 3 is similar to Investigation 1 and different to Investigation 2, in that it has a flat mass function instead of a Maschberger IMF (see Table 6.2).

Figure 6.10 shows the values of $R_{0.1}$, $R_{0.5}$ and $R_{0.9}$ for the stars (blue) and the gas (orange) as a function of time for Investigations 3.1 ($R_{i,0.5} = 0.25$ pc; $N_g = 2000$), 3.2 ($R_{i,0.5} = 0.25$ pc; $N_g = 20000$), 3.3 ($R_{i,0.5} = 0.50$ pc; $N_g = 2000$) and 3.4 ($R_{i,0.5} = 0.50$ pc; $N_g = 20000$).

Comparing Figure 6.10 for Investigation 3 to Figure 6.1 for Investigation 1 shows that the differences between the final star and gas Lagrangian radii are smaller for $N_\star = 200$ than those seen previously for $N_\star = 100$, for equal-mass stars.

This can also be seen in Figure 6.11, which shows the star formation efficiency $\epsilon_{\rm sf}(r)$ given by Equation 1.30 as a function of the distance r from the cluster centre of mass, at times $t = 0$ Myr, 3 Myr and 5 Myr, for each of the Investigations 3.1 to 3.4. Contrary to Investigations 1 and 2, the shapes of $\epsilon_{\rm sf}(r)$ at $t = 3$ Myr and $t = 5$ Myr are almost the same, indicating a less dramatic evolution of $\epsilon_{\rm sf}(r)$ within these times.

This decrease in the dynamical evolution of the cluster is explained as being due to the increase in its relaxation time $t_{\rm r}$, given by Equation 1.26. As $t_{\rm r} \propto N/\ln N$, increasing $N_\star$ from 100 to 200 results in a value for $t_{\rm r}$ which is 1.74 times greater, i.e. the rate of increase of $\epsilon_{\rm sf}(r)$ as a function of time is ~ 0.57 times slower.

6.3.6 Investigation 4

Similar to Investigation 3, in investigation 4 the number of star particles $N_\star = 200$ and the corresponding number of gas particles is varied between $N_g = 2000$ and $N_g = 20000$. Otherwise, Investigation 4 is similar to Investigation 2 in that the mass function is given by the Maschberger IMF (see Table 6.2).

Figure 6.12 shows the values of $R_{0.1}$, $R_{0.5}$ and $R_{0.9}$ for the stars (blue) and the gas (orange) as a function of time for Investigations 4.1 ($R_{i,0.5} = 0.25$ pc; $N_g = 2000$), 4.2

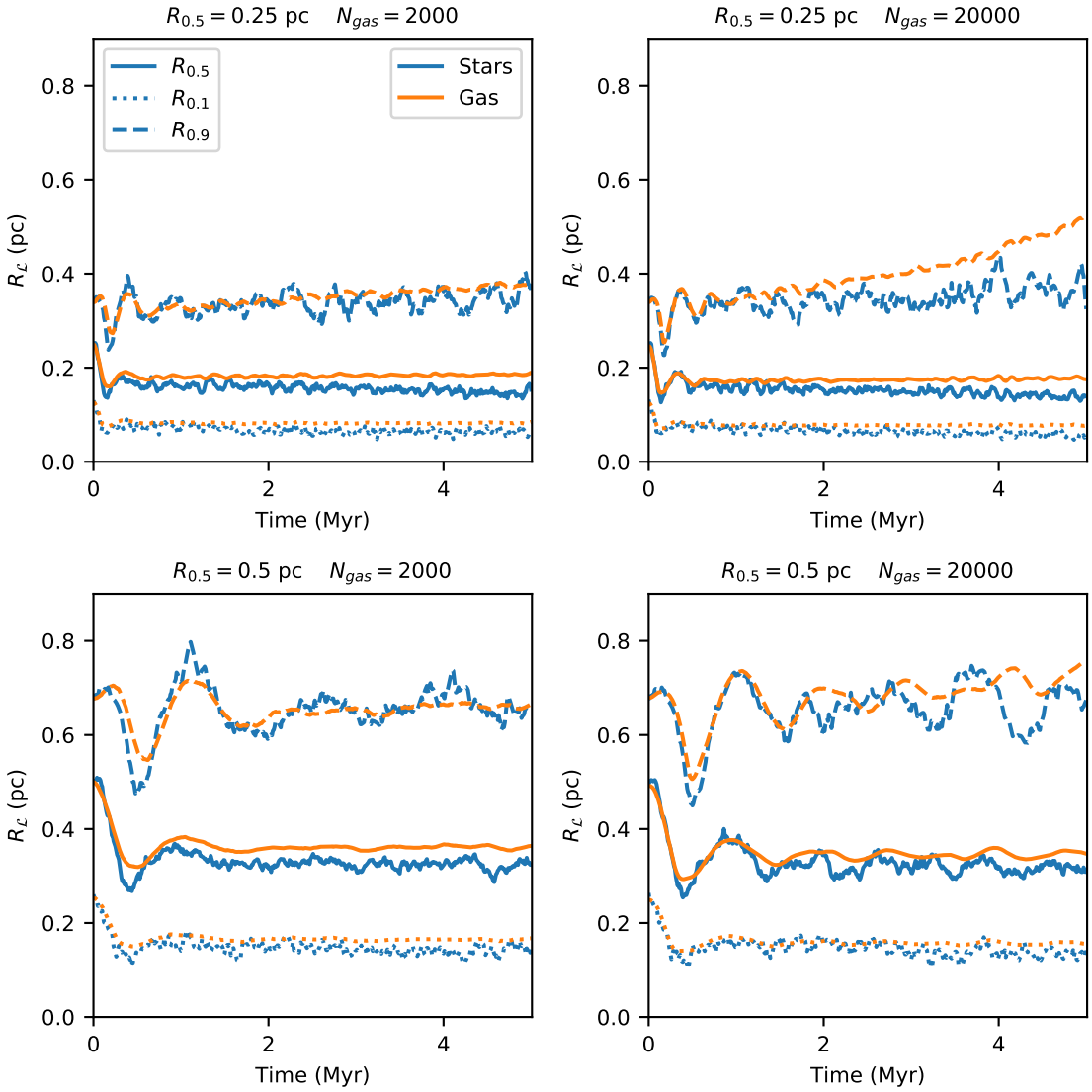

Figure 6.10: The $R_{0.1}$, $R_{0.5}$ and $R_{0.9}$ for the stars (blue) and the gas (orange) as a function of time for Investigation 3.1 (top-left), 3.2 (top-right), 3.3 (bottom-left) and 3.4 (bottom-right).

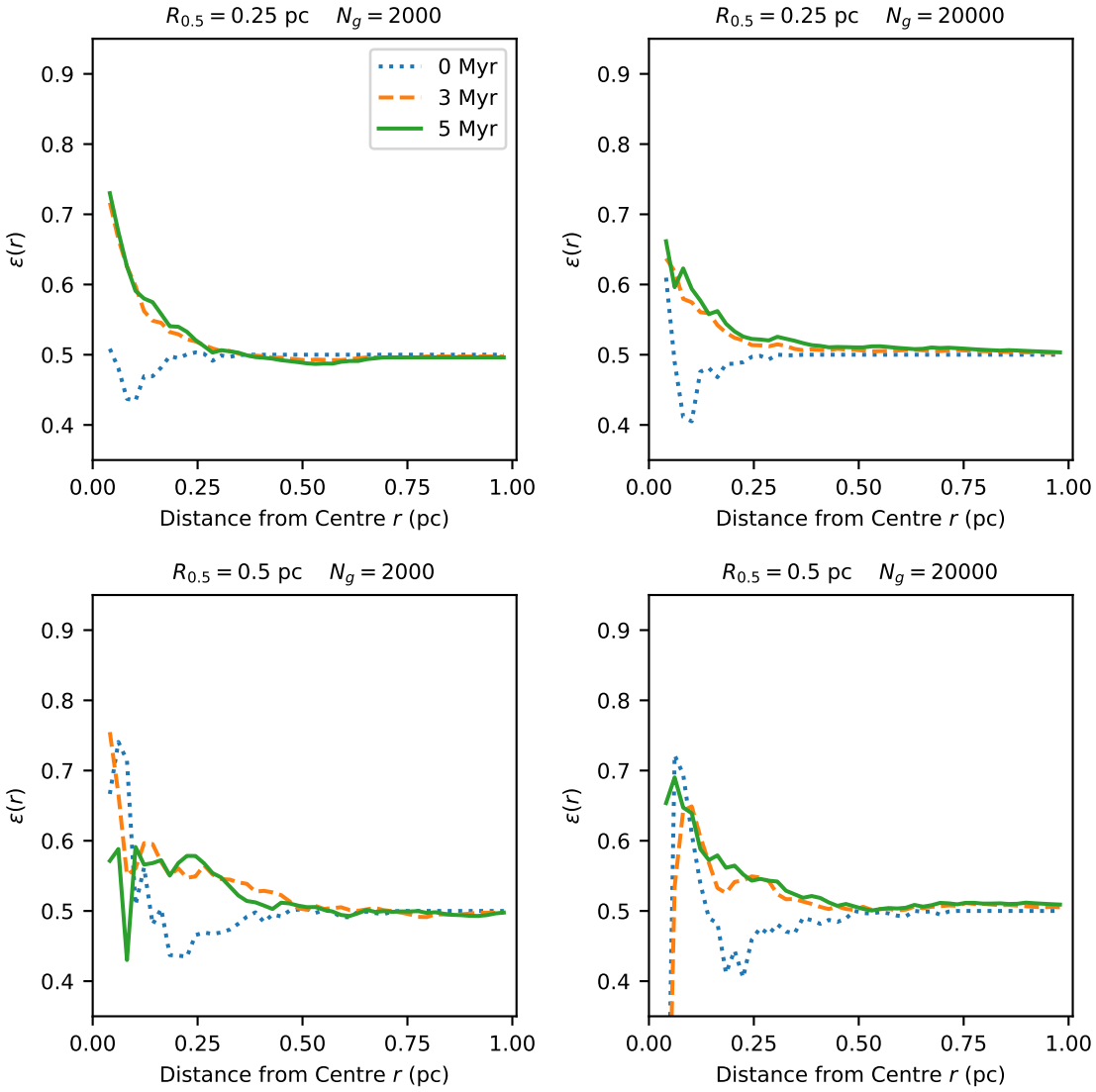

Figure 6.11: The star formation efficiency $\epsilon_{\rm sf}(r)$ given by Equation 1.30 as a function of the distance r from the cluster centre of mass, at times $t = 0$ Myr, 3 Myr and 5 Myr, for Investigations 3.1 (top-left), 3.2 (top-right), 3.3 (bottom-left) and 3.4 (bottom-right).

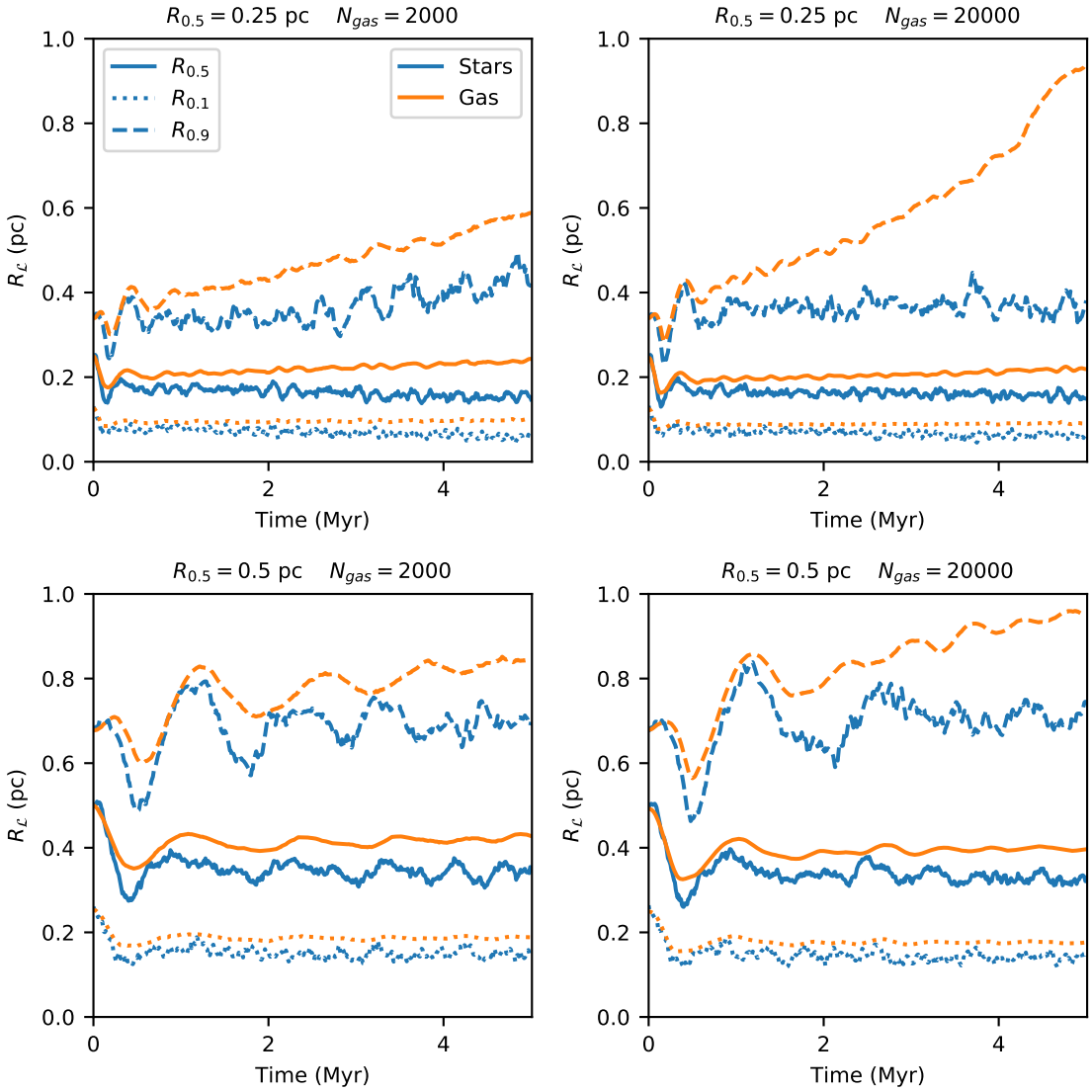

Figure 6.12: The $R_{0.1}$, $R_{0.5}$ and $R_{0.9}$ for the stars (blue) and the gas (orange) as a function of time for Investigation 4.1 (top-left), 4.2 (top-right), 4.3 (bottom-left) and 4.4 (bottom-right).

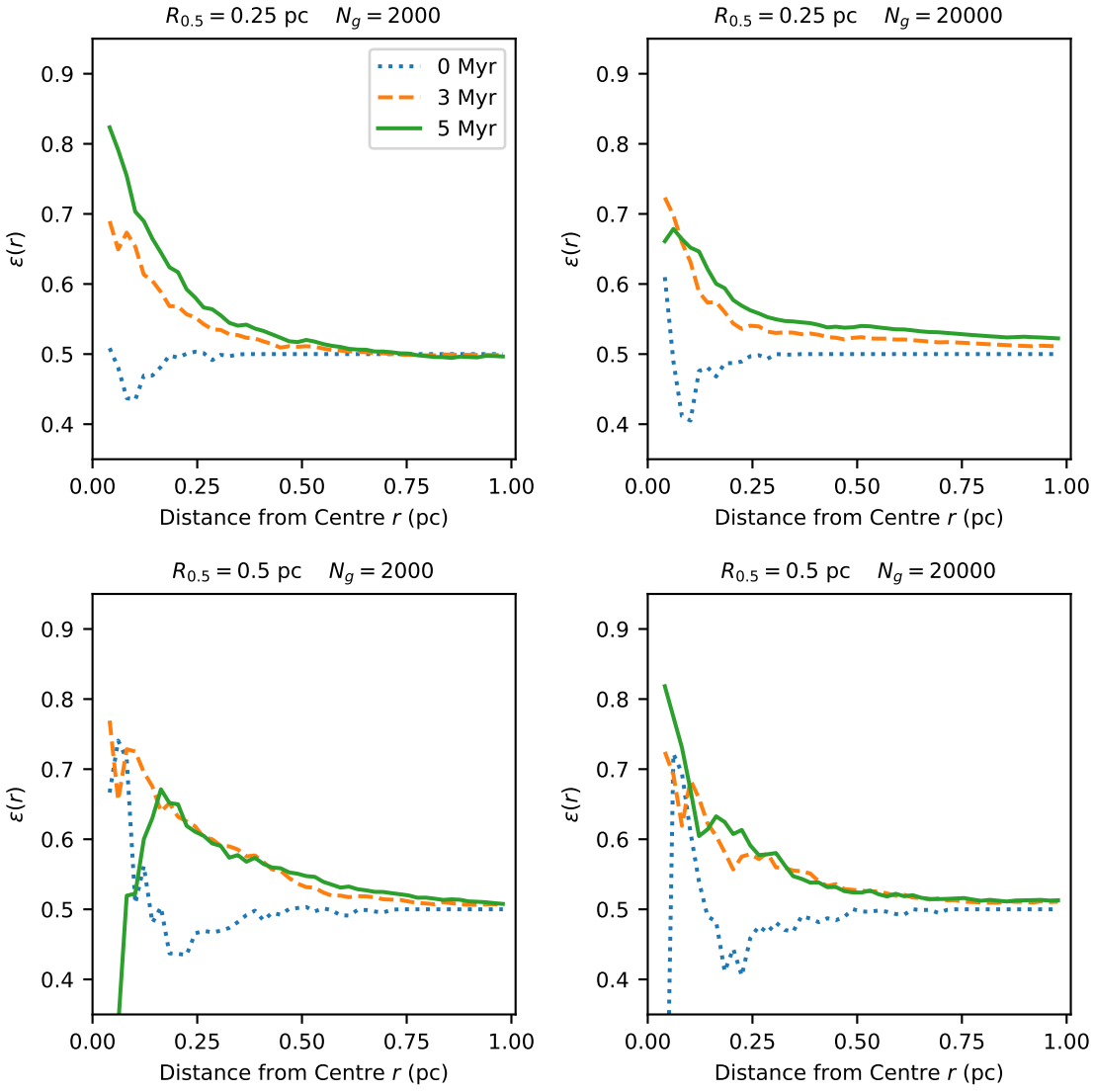

Figure 6.13: The star formation efficiency $\epsilon_{\rm sf}(r)$ given by Equation 1.30 as a function of the distance r from the cluster centre of mass, at times $t = 0$ Myr, 3 Myr and 5 Myr, for Investigations 4.1 (top-left), 4.2 (top-right), 4.3 (bottom-left) and 4.4 (bottom-right).

Investigation	$\mathcal{R}_{0.1}$	$\mathcal{R}_{0.5}$	$\mathcal{R}_{0.9}$	$\Lambda_{\rm MST}$
3.1	0.69	0.81	0.97	1.0
3.2	0.72	0.80	0.62	1.0
3.3	0.87	0.89	1.00	1.0
3.4	0.85	0.89	0.89	1.0
4.1	0.50	0.61	0.71	1.49 ± 0.01
4.2	0.72	0.68	0.41	1.41 ± 0.01
4.3	0.81	0.83	0.82	1.40 ± 0.01
4.4	0.81	0.81	0.78	1.39 ± 0.01

Table 6.4: Table showing the $\mathcal{R}_{0.1}$, $\mathcal{R}_{0.5}$ and $\mathcal{R}_{0.9}$ values, where $\mathcal{R}_{\alpha}$ is given by Equation 6.1, for Investigations 3.1 to 4.4.

($R_{i,0.5} = 0.25$ pc; $N_g = 20000$), 4.3 ($R_{i,0.5} = 0.50$ pc; $N_g = 2000$) and 4.4 ($R_{i,0.5} = 0.50$ pc; $N_g = 20000$), in which the stellar mass distribution is given by the Maschberger IMF.

Comparison of Figure 6.12 for Investigation 4 and Figure 6.10 for Investigation 3 shows that the addition of a mass function increases the effect of dynamical gas depletion in the cluster's core, counteracting the effect of increasing the value of $N_{\star}$.

As already seen with the results of Investigation 2, the addition of a mass function introduces new dynamical effects, such as the possibility of dynamical mass segregation and the creation of massive binaries. The $\Lambda_{\rm MST}$ parameter for Investigations 3 and 4 is shown in Table 6.4. Because Investigation 3 only contains equal-mass stars, the $\Lambda_{\rm MST}$ parameter is equal to unity. For Investigation 4, the $\Lambda_{\rm MST}$ is close to unity at $t = 0$ Myr, but has decreased to ~ 1.4 – 1.5 by $t = 5$ Myr. This shows that the massive stars are in closer proximity compared to the typical distance between stars, i.e. they have become dynamically mass segregated. Similar to Investigation 2, this mass segregation should increase the effect of dynamical gas depletion as the massive stars collapse towards the core.

6.3.7 Summary of Results for Investigation 3 and 4

Table 6.4 shows the values for $\mathcal{R}$ for Investigations 3 and 4. In all investigations, the interactions between the stars and the gas in the cluster cause the core star formation efficiency $\epsilon_{\rm sf}(r)$ to increase over time.

This increase is occurs over a longer time-frame in Investigation 3 compared to Investigation 1, due to the increase in $N_{\star}$ meaning an increased relaxation time $t_{\rm r}$.

The effect of the increased relaxation time is counterbalanced in Investigation 4 by the

addition of a mass spectrum. However, this mass spectrum also causes other dynamical effects such as mass segregation, which affect the dynamical state of the cluster in non-trivial ways.

6.4 Discussion of Results

We perform 16 numerical simulations, one for each of the initial conditions in Table 6.2. These simulations show the dynamical evolution of a cluster consisting of 50% stars and 50% gas for 5 Myr.

The primary conclusion drawn from the simulations show that the contraction of a cluster core due to two-body relaxation can dynamically deplete the gas in the cluster core without the need for stellar feedback in the form of winds or supernovae. This dynamical gas depletion means that the star formation efficiency of a cluster core as estimated by measurements of the core's stellar and gas contributions may be unrelated to the core's actual star formation efficiency.

Furthermore, this effect has consequences for the idea of cluster 'infant mortality' due to gas expulsion. In order for the rapid expulsion of gas (due to stellar feedback) to unbind a cluster and therefore make it disperse, the mass contribution of gas in that cluster's core must be significant. The effect of dynamical gas depletion is to lower the cluster's core gas mass, i.e. increasing its effective SFE (see Goodwin, 2009). This means that the ratio of stellar mass to gas mass in the centre of the cluster has decreased to the point where the gas mass no longer dominates, and the change in total mass due to the rapid removal of the gas (due to supernovae and stellar winds) is no longer large enough to cause the cluster to become gravitationally unbound. In other words, the cluster cannot be destroyed via the mechanism of gas expulsion.

Dynamical Timescales

The initial cluster half-mass radius $R_{\rm i,0.5}$ was varied, from $R_{\rm i,0.5} = 0.25$ pc to $R_{\rm i,0.5} = 0.50$ pc. Doing so did not prevent core gas depletion from occurring, however it did decrease the magnitude of the effect. Increasing $R_{\rm i,0.5} = 0.25$ pc to $R_{\rm i,0.5} = 0.50$ pc. increases the cluster's crossing time $t_{\rm cr}$ from $t_{\rm cr} \sim 0.08$ Myr to $t_{\rm cr} \sim 0.22$ Myr. Hence this increases the time-frame in which the dynamical gas depletion of the cluster core occurs.

The number of star particles $N_\star$ was varied, from $N_\star = 100$ to $N_\star = 200$. Doing so had the same effect as increasing $R_{\rm i,0.5}$ - the dynamical core gas depletion still occurred but on a longer timescale. Increasing $N_\star = 100$ to $N_\star = 200$ has results in a relaxation

time $t_{\rm r} \sim 1.74$ times greater, explaining the decrease in the change in $\epsilon_{\rm sf}(r)$ as a function of time.

Mass Segregation

The change in the initial conditions which produced the largest effect on the results of the simulation was the introduction of a mass function. The presence of stars with non-equal mass produces the potential for dynamical effects which do not occur in groups of equal-mass stars. Two of these effects - mass segregation and the formation of a massive binary - were apparent in the results of the simulations.

The effect of mass segregation was to increase the rate at which $\epsilon_{\rm sf}(r)$ increases as a function of time (see Investigations 2 and 4), but it also caused large fluctuations in the value of $\epsilon_{\rm sf}(r)$ at low r. Increasing the number of stars $N_\star$ from 100 in Investigation 2 to 200 in Investigation 4 has partly mitigated this effect, giving the hope that simulations of much larger $N_\star$ would decrease the fluctuations in $\epsilon_{\rm sf}(r)$ to negligible sizes.

Binary formation

The formation of a hard binary in Investigation 2.1 provides an additional potential mechanism for the rapid dispersal of a star cluster, without the need for gas expulsion via stellar feedback.

In investigation 2.1, the two most massive stars in the cluster have formed a hard binary system, which has a binding energy of the order $\sim 10^{39}$ J which is of the order of the binding energy of the cluster. Therefore, the formation of this binary system has caused it to become gravitationally unbound and therefore disperse into the field.

This phenomenon has been observed before in Allison et al. (2010). However, it has not been studied in detail. Therefore it is a mechanism that merits further study.

6.5 Conclusion

The dynamical depletion of gas in the core of a dense cluster due to core contraction was investigated by performing simulations using the hybrid N-body/SPH numerical integrator GANDALF (Hubber et al., 2013). We performed 16 simulations, varying the initial cluster half-mass radius, the number of star and gas particles, and the presence of a flat mass function or a Maschberger (2013) initial mass function.

Gas depletion in the cluster core was observed in all 16 simulations in varying degrees. The effect of this gas depletion was to increase the apparent core star formation efficiency

and decrease the likelihood that the cluster would be gravitationally unbound by gas expulsion due to stellar feedback.

Varying the initial properties of the cluster caused a multitude of different effects on the cluster's dynamical evolution, while still retaining the effect of core depletion in almost all circumstances. Increasing the initial half-mass radius and the number of stars in the cluster both increased the time-frame in which the effect occurs, while the introduction of a Maschberger IMF causes new dynamical effects to become significant, such as mass segregation, and the disruption of the cluster by the formation of a massive binary system.

This also shows that, when performing simulations of clusters containing a mixture of stars and gas, those clusters cannot be assumed to be stable - the spatial distribution of the stars and the gas will change over time as the stars relax.

The simulations in this chapter have assumed that the gas in the clusters is adiabatic. If the gas is not adiabatic and is *more* effective at cooling, then it will not be stable but will collapse towards the cluster's core. On the other hand, if the gas is *less* effective at cooling (which is expected due to heating from stars), then the effect of gas depletion should be more pronounced. Therefore, the effect of changing the equation of state of the gas and simulating the ffect of radiative feedback merits further study.

Chapter 7

Conclusion

7.1 Introduction

We have performed N-body and hybrid N-body/SPH simulations to investigate the dynamical evolution of young stellar regions, and to provide answers to outstanding questions in the field of star formation. In Section 1.4, we outlined three questions to which this thesis aimed to address:

1. How do young stellar regions evolve (and die)?
2. What diagnostics can we use to determine the past of a young stellar region?
3. If most stars form in clusters, how does this affect the properties of the Galactic field stellar population?

In this chapter, we revisit these questions in the context of the original research we have undertaken in Chapters 4, 5 and 6.

7.2 Massive, Wide Binaries as Tracers of Massive Star Formation

The properties of young stellar regions can transform dramatically over time due to the interactions of their resident stars with both each other and with the surrounding gas, and the interactions of a region with its environment. However, it is not always possible to use current observations of a region as an indication of its evolutionary history. Due to dynamical effects (such as core collapse, mass segregation and the erasure of substructure

- see Chapter 1), two regions which have very different dynamical histories may look similar today. Similarly, due to stochasticity, two young stellar regions which appear the same may evolve differently in the future.

As explained in Section 1.4, there are competing theories for how stellar regions evolve. If most (or all) stars form in dense clusters which eventually disperse into the field, then it follows that dense clusters are important objects of study and that theories of star and planet formation need to take the influence of dense clusters into consideration. On the other hand, if most stars form in relatively dispersed regions (some of which then expand, some of which collapse and some of which remain relatively static), then it follows that dense clusters are less important for theories of star and planet formation. One example already mentioned is competitive accretion, which describes the formation of massive stars as the result of clustered star formation with a shared gas reservoir, as opposed to monolithic collapse, which argues that massive stars can form in relative isolation. Another example is planet formation. If most stars form in dense clusters, then planets must form and survive in relatively crowded and violent environments. Therefore, finding diagnostics which allow us to provide the past history of a stellar region is crucial for the wider study of star and planet formation.

In Chapter 4 we tackle these two questions (i.e. how do young stellar regions evolve? What diagnostics can we find?) by proposing that the presence of massive wide binary (MWB) systems in a region gives an indication of how that region has evolved. We define MWBs as binary systems containing two stars, both with masses $m_\star > 5M_\odot$ and separations between 10^2 and 10^4 AU. These binaries have binding energies which cause them to be easily destroyed in an encounter with another star with a similar or greater mass. We propose that a region containing many MWBs could not have evolved from a much more dense region in the past, because those MWBs would have been destroyed in dynamical interactions with other stars. Therefore, the presence of MWBs can be used as a diagnostic to indicate the past density of a stellar region.

To test this hypothesis, we perform 3200 N-body simulations to investigate the formation and destruction of massive wide binaries (MWBs) in young stellar regions. We simulate clusters as Plummer spheres, each of which either contain one 'primordial' MWB or two massive, single stars. The rest of the stars in the cluster are: (a) all 1 $M_\odot$; (b) an IMF with $m_\star < 10$ $M_\odot$; (c) an IMF with one other (more) massive star; or (d) an IMF with three other (more) massive stars. The initial cluster half-mass radius was changed between 0.25, 0.5, 1.0 and 1.5 pc.

Our results are as follows:

- If the MWB contains the two most massive stars in the cluster, then the MWB will survive in a region which has any initial density. However, if the region is dense, then interactions with other stars may cause the MWB to harden to the point where it can no longer be considered 'wide'.
- If the MWB is in a dense region with other stars of greater mass, then it will typically not survive due to encounters with the more massive stars. However, since MWBs also form in high-density regions, any high-density region should contain, on average, one MWB which will typically contain the two most-massive stars in the region.
- If the MWB is in a region with low density, then that MWB will typically survive.

These results lead us to conclude that, if a region contains many MWBs, then it could not have evolved from a single, dense region in the past. This conclusion has consequences for theories of star formation. If the presence of MWBs in a region show that the region was never dense, then it follows that not all stars form in dense clusters, and dense clusters may not be central to understand where stars form.

This conclusion also has consequences for the search for diagnostics to probe the past properties of young stellar regions and the understanding of the evolutionary past of stellar associations such as Cyg OB2. Cyg OB2 contains stars with masses up to 100 $M_{\odot}$ and many MWBs. Using the presence of MWBs as a diagnostic allows us to determine that Cyg OB2 did not evolve from a much denser region but instead formed much closer to how it looks today. This conclusion is in agreement with other studies of the substructure and kinematics of Cyg OB2. Because MWBs are composed from two massive (i.e. bright) stars, we propose that observers search for the presence of MWBs in other nearby young stellar regions to allow us to probe their evolutionary history.

7.2.1 The Formation of Very Wide Binaries in a Supervirial Association

While dense clusters may or may not be central to star formation, most young stars are found in regions of higher density relative to the Galactic field (Lada & Lada, 2003), meaning that these young stars will eventually disperse to replenish the Galactic field population. Therefore, in order to determine the origin of the properties of the Galactic field stellar population, it is necessary to investigate how that population is seeded by the stars from young stellar regions.

For example, the origin of the population of very wide binary (VWB) systems in the Galactic field is not well understood. We define a VWB as a binary system with a separation greater than 10000 AU. Because of their wide separation, VWBs are very weakly gravitationally bound and are therefore easily destroyed, giving them a lifetime in the field of 2 Gyr. The observed field VWB population must therefore be continually replenished (e.g. 5% of solar-type stars are in VWBs). In Chapter 5, we investigate whether the population of VWBs in the Galactic field can be explained as due to a single mechanism: soft capture during the dissolution of supervirial stellar associations.

We perform 400 N-body simulations of unbound stellar associations. Our associations' initial properties were varied - the virial ratio $Q_{\rm vir}$ ($Q_{\rm vir}$ = 1.05, 1.15, 1.25, 1.35 and 1.5), the fractal dimension $F_{\rm dim}$ ($F_{\rm dim}$ = 1.6, 2.0, 2.6 and 3.0) and the total stellar number $N_\star$ ($N_\star$ =500 and 5000) - to produce 40 unique sets of initial conditions.

Our results were as follows:

- The initial virial ratio $Q_{\rm vir}$ has a negligible effect on the number of VWBs which form.
- The number of binaries which form decreases as the association's initial fractal dimension $F_{\rm dim}$ increases.
- For VWBs, the number which form as a function of $F_{\rm dim}$ is roughtly constant at low values of $F_{\rm dim}$ but drops off sharply as $F_{\rm dim}$ increases (at $F_{\rm dim} \sim 2.0$ for $N = 500$ and $F_{\rm dim} \sim 2.6$ for $N = 5000$). This is explained as being due to the increased encounter rate at high values of $F_{\rm dim}$, leading to higher rates of VWB destruction.
- Increasing the number of stars in an association N decreases the number of VWBs which survive.

However, our main result is that, while the soft-capture mechanism during the dissolution of a stellar association does produce VWBs, this mechanism alone is not sufficient to account for the observed number of field G-dwarfs in VWBs. Instead, it is possible that several mechanism (such as the unfolding of triple systems - see Reipurth et al., 2014) may contribute to the Galactic field VWB population. Therefore, while Chapter 5 succeeded in confirming that stellar associations are *a* source of very wide binary systems, the question of the origin of the Galactic field VWB population (i.e. Question 3 in Section 7.1 above) remains an open one.

7.2.2 The Uncoupling of the Dynamical Evolution of Stars and Gas in a Dense Cluster

How do young stellar regions die? Only 10% of star clusters survive longer than 10 Myr (so-called 'infant mortality', Lada & Lada, 2003). One proposed cause of the death of star clusters is gas expulsion. Molecular gas makes up a significant fraction of the total mass of a young stellar cluster. The rapid dispersal of this gas due to stellar winds and supernovae can cause a star cluster to become gravitationally unbound and disperse its stellar population into the field (see Section 1.3.7).

However, if the gas component of a star cluster has been depleted over time by another mechanism, then the effect of rapid gas dispersal due to stellar feedback may be less pronounced and the cluster may survive.

In Chapter 6 we propose that the gas in the core of a cluster can be depleted purely by dynamical effects, namely the dynamical core contraction first demonstrated by Aarseth et al. (1974). In order to test the hypothesis, we perform 16 hybrid N-body/SPH simulations to investigate the dynamical depletion of gas in the core of a dense cluster due to core contraction. The initial properties were varied - the initial half-mass radius $R_{\rm i,0.5}$ ($R_{\rm i,0.5} = 0.25$ pc and $R_{\rm i,0.5} = 0.50$ pc), the number of stars $N_\star$ ($N_\star = 100$ and $N_\star = 200$), the number of gas particles N_g ($N_g = 1000$, 2000, 10000 and 20000) and the stellar mass distribution (either a flat mass function or an IMF).

Gas depletion in the cluster core was observed in all 16 simulations in varying degrees. The effect of this gas depletion was to increase the apparent core star formation efficiency and decrease the likelihood that the cluster would be gravitationally unbound by gas expulsion due to stellar feedback. Varying the initial properties of the cluster caused a multitude of different effects on the cluster's dynamical evolution, while still retaining the effect of core depletion in almost all circumstances. Increasing the initial half-mass radius and the number of stars in the cluster both increased the time-frame in which the effect occurs, while the introduction of a Maschberger IMF causes new dynamical effects to become significant, such as mass segregation, and the disruption of the cluster by the formation of a massive binary system.

These results led us to conclude that, while gas dispersal may be an effective mechanism for unbinding a young star cluster in some scenarios, the death of 90% of star clusters before 10 Myr cannot be explained by gas dispersal alone, and other mechanisms are necessary. One such mechanism, the formation of a massive binary system, is identified in Chapter 6 as another potential avenue for the destruction of star clusters. Therefore, while the question of how star clusters die is still an open one, we hope that

our new results have contributed to the understanding of the mechanisms which can destroy young star clusters.

7.3 Future Work

The conclusions drawn in this thesis give rise to several potential avenues for future enquiry:

1. The work on the formation of very wide binaries (VWBs) during the dissolution of a stellar association in Chapter 5 is currently being assembled into a paper (in prep. as Goodwin & Griffiths, 2018a).

2. The work on the change in the effecting star formation efficiency due to the dynamical evolution of stars and gas in a dense cluster in Chapter 6 is also currently being assembled into a paper (in prep. as Goodwin & Griffiths, 2018b).

3. Chapter 4 showed that the presence of a large population of MWBs in a region points to that region having not evolved from a single dense cluster, using the observed presence of MWBs in Cyg OB2 as an example. Future observation of young associations can look specifically for the presence (or absence) of MWBs as a way to determine their past dynamical evolution.

4. Chapter 5 concluded that the soft capture mechanism, on its won, is not sufficiently efficient at producing VWBs to account for the field G-dwarf VWB population. Future simulations could add primordial binaries and multiples, to investigate how soft capture, combined with other mechanisms such as 'unfolding' of triple systems and the unstable decay of higher-order multiples, affects the number of VWBs which can form.

5. Chapter 6 showed that adiabatic gas will be depleted in the core of a dense cluster due to the relaxation of the stars in the cluster. Future work will focus on changing the equation of state of the gas and adding radiative feedback from stars, to investigate whether these changes will increase or decrease the effect of core gas depletion.

6. Chapter 6 also showed how the formation of a hard, massive binary can disrupt a cluster. Future work would entail a large number of N-body simulations to determine the likelihood of this event occurring in clusters with different initial properties.

Bibliography

Aarseth S. J., 1985, in Brackbill J. U., Cohen B. I., eds, , Multiple Time Scales. Elsevier, Chapt. Direct Met, pp 377–418

Aarseth S., 2003, Gravitational N-Body Simulations: Tools and Algorithms. Cambridge University Press, Cambridge

Aarseth S. J., Hills J. G., 1972, Astronomy & Astrophysics, 21, 255

Aarseth S. J., Henon M., Wielen R., 1974, Astronomy & Astrophysics, 37, 183

Adams F. C., Myers P. C., 2001, The Astrophysical Journal, 553, 744

Adams F. C., Lada C. J., Shu F. H., 1987, The Astrophysical Journal, 312, 788

Allison R. J., Goodwin S. P., 2011, Monthly Notices of the Royal Astronomical Society, 415, 1967

Allison R. J., Goodwin S. P., Parker R. J., Portegies Zwart S. F., de Grijs R., Kouwenhoven M. B. N., 2009a, Monthly Notices of the Royal Astronomical Society, 395, 1449

Allison R. J., Goodwin S. P., Parker R. J., de Grijs R., Portegies Zwart S. F., Kouwenhoven M. B. N., 2009b, The Astrophysical Journal, 700, L99

Allison R. J., Goodwin S. P., Parker R. J., Portegies Zwart S. F., De Grijs R., 2010, Monthly Notices of the Royal Astronomical Society, 407, 1098

Alves J., Lombardi M., Lada C. J., 2007, Astronomy and Astrophysics, 462, L17

André P., Ward-Thompson D., Barsony M., 1993, The Astrophysical Journal, 406, 122

André P., Ward-Thompson D., Barsony M., 2000, Protostars and Planets IV, p. 37

André P., Di Francesco J., Ward-Thompson D., Inutsuka S.-I., Pudritz R. E., Pineda J., 2014, in Beuther H., Klessen R. S., Dullemond C. P., Henning T., eds, , Protostars and Planets VI. University of Arizona Press, Tucson, pp 27–51

Ballesteros-Paredes J.; Klessen R. S., Mac Low M.-M., Vazquez-Semadeni E., 2007, in Reipurth B., Jewitt D., Keil K., eds, , Protostars and Planets V. University of Arizona Press, pp 63–80

Balsara D. S., 1995, Journal of Computational Physics, 121, 357

Barnes J., Hut P., 1986, Nature, 324, 446

Bastian N., Covey K. R., Meyer M. R., 2010, Annual Review of Astronomy and Astrophysics, 48, 339

Bate M. R., 2009, Monthly Notices of the Royal Astronomical Society, 392, 590

Bate M. R., 2012, Monthly Notices of the Royal Astronomical Society, 419, 3115

Baumgardt H., Kroupa P., 2007, Monthly Notices of the Royal Astronomical Society, 380, 1589

Benz W., 1990, in Buchler J. R., ed., , The Numerical Modelling of Nonlinear Stellar Pulsations: Problems and Prospects. Springer Netherlands, Dordrecht, pp 269–288

Bergin E. A., Tafalla M., 2007, Annual Review of Astronomy and Astrophysics, 45, 339

Binney J., Tremaine S., 1987, Galactic Dynamics. Princeton University Press, Princeton, NJ

Blitz L., 1993, Protostars and Planets III, pp 125–161

Bok B. J., Reilly E. F., 1947, The Astrophysical Journal, 105, 255

Bonnell I. a., Bate M. R., 2006, Monthly Notices of the Royal Astronomical Society, 370, 488

Bonnell I., Davies M., 1998, Monthly Notices of the Royal . . . , 698, 691

Bonnell I. a., Bate M. R., Clarke C. J., Pringle J. E., 1997, Monthly Notices of the Royal Astronomical Society, 285, 201

Bonnell I. a., Bate M. R., Clarke C. J., Pringle J. E., 2001, Monthly Notices of the Royal Astronomical Society, 323, 785

Bonnell I. A., Vine S. G., Bate M. R., 2004, Monthly Notices of the Royal Astronomical Society, 349, 735

Boss A. P., Bodenheimer P., 1979, The Astrophysical Journal, 234, 289

Bressert E., et al., 2010, Monthly Notices of the Royal Astronomical Society: Letters, 409, L54

Bressert E., et al., 2012, Astronomy & Astrophysics, 542, A49

Burrows C. J., et al., 1996, The Astrophysical Journal, 473, 437

Cambresy L., 1999, Astronomy & Astrophysics, 345, 8

Carr B., Kühnel F., Sandstad M., 2016, Physical Review D, 94, 083504

Carruthers G. R., 1970, The Astrophysical Journal, 161, L81

Cartwright A., Whitworth A. P., 2004, Monthly Notices of the Royal Astronomical Society, 348, 589

Cartwright A., Whitworth A. P., 2009, Monthly Notices of the Royal Astronomical Society, 392, 341

Chabrier G., 2003, Publications of the Astronomical Society of the Pacific, 115, 763

Chaname J., Gould A., 2003, The Astrophysical Journal, 601, 56

Chen H., Myers P. C., Ladd E. F., Wood D. O. S., 1995, The Astrophysical Journal, 445, 377

Chen X., et al., 2013, Astrophysical Journal, 768

Close L. M., Richer H. B., Crabtree D. R., 1990, The Astronomical Journal, 100, 1968

Crutcher R. M., 1999, The Astrophysical Journal, 520, 706

Da Rio N., Tan J. C., Jaehnig K., 2014, The Astrophysical Journal, 795, 55

Da Rio N., et al., 2017, The Astrophysical Journal, 845, 105

Dhital S., West A. A., Stassun K. G., Schluns K. J., Massey A. P., 2015, The Astronomical Journal, 150, 57

Duchêne G., Kraus A., 2013, Annual Review of Astronomy and Astrophysics, 51, 269

Duchêne G., Bouvier J., Bontemps S., André P., Motte F., 2004, Astronomy & Astrophysics, 427, 651

Duchêne G., Delgado-Donate E., Haisch K., Loinard L., Rodriguez L., 2007, in Reipurth B., Jewitt D., Keil K., eds, , Protostars and Planets V. University of Arizona Press, Tucson, pp 379–394

Duchêne G., Lacour S., Moraux E., Goodwin S., Bouvier J., 2018, Monthly Notices of the Royal Astronomical Society, 478, 1825

Dunham M. M., et al., 2014, in , Vol. 1401, Protostars and Planets VI. University of Arizona Press, p. 1809

Duquennoy A., Mayor M., 1991, Astronomy and Astrophysics, 248, 485

Evans N. J., et al., 2009, Astrophysical Journal, Supplement Series, 181, 321

Federrath C., 2016, Journal of Physics: Conference Series, 719

Federrath C., Klessen R. S., 2012, Astrophysical Journal, 761

Figer D. F., Mclean I. S., Morris M. R., 1999, The Astrophysical Journal, 514, 202

Frank A., et al., 2014, in , Protostars and Planets VI. University of Arizona Press

Fujii M. S., Portegies Zwart S., 2011, Science, 334, 1380

Gennaro M., Goodwin S. P., Parker R. J., Allison R. J., Brandner W., 2017, Monthly Notices of the Royal Astronomical Society, 472, 1760

Gieles M., Portegies Zwart S. F., 2011, Monthly Notices of the Royal Astronomical Society: Letters, 410, L6

Gingold R. A., Monaghan J. J., 1977, Monthly Notices of the Royal Astronomical Society, 181, 375

Gingold R. A., Monaghan J. J., 1982, Journal of Computational Physics, 46, 429

Goodman J., Hut P., 1993, The Astrophysical Journal, 403, 271

Goodwin S. P., 1997, Monthly Notices of the Royal Astronomical Society, 284, 785

Goodwin S. P., 2009, Astrophysics and Space Science, 324, 259

Goodwin S. P., Bastian N., 2006, Monthly Notices of the Royal Astronomical Society, 373, 752

Goodwin S. P., Whitworth a. P., 2004, Astronomy and Astrophysics, 413, 929

Goodwin S. P., Kroupa P., Goodman A., Burkert A., 2007, in Reipurth B., Jewitt D., Keil K., eds, , Vol. 1, Protostars and Planets V. University of Arizona Press, Tucson, pp 133–147

Griffiths D. W., Goodwin S. P., Caballero-Nieves S. M., 2018, Monthly Notices of the Royal Astronomical Society, 476, 2493

Haisch, Jr. K. E., Greene T. P., Barsony M., Stahler S. W., 2004, The Astronomical Journal, 127, 1747

Heggie D. C., 1975, Monthly Notices of the Royal Astronomical Society, 173, 729

Hennebelle P., Chabrier G., 2008, The Astrophysical Journal, 684, 395

Henon M., 1971, Astrophysics and Space Science, 14, 151

Hernquist L., 1993, The Astrophysical Journal, 404, 717

Hernquist L., Katz N., 1989, The Astrophysical Journal Supplement Series, 70, 419

Hillenbrand L. a., Hartmann L. W., 1998, The Astrophysical Journal, 492, 540

Hills J. G., 1975, The Astronomical Journal, 80, 809

Hills J. G., 1980, The Astrophysical Journal, 235, 986

Hills J. G., 1990, The Astronomical Journal, 99, 979

Hubber D. A., Batty C. P., McLeod A., Whitworth A. P., 2011, Astronomy & Astrophysics, 529, A27

Hubber D. A., Allison R. J., Smith R., Goodwin S. P., 2013, Monthly Notices of the Royal Astronomical Society, 430, 1599

Jeans J. H., 1902, Philosophical Transactions of the Royal Society A: Mathematical, Physical and Engineering Sciences, 199, 1

Joy A. H., 1945, The Astrophysical Journal, 102, 168

Kauffmann J., Bertoldi F., Bourke T. L., Evans N. J., Lee C. W., 2008, Astronomy & Astrophysics, 487, 993

King R. R., Parker R. J., Patience J., Goodwin S. P., 2012, Monthly Notices of the Royal Astronomical Society, 421, 2025

Kokubo E., Yoshinaga K., Makino J., 1998, Monthly Notices of the Royal Astronomical Society, 297, 1067

Kolmogorov A., 1941, Doklady Akademiia Nauk SSSR, 30

Kouwenhoven M. B. N., Goodwin S. P., Parker R. J., Davies M. B., Malmberg D., Kroupa P., 2010, Monthly Notices of the Royal Astronomical Society, 14, 14

Kroupa P., 2001, Monthly Notices of the Royal Astronomical Society, 322, 231

Kroupa P., 2011, in Alfaro Navarro E. J., Gallego Calvente A. T., Zapatero Osorio M. R., eds, , Stellar Clusters & Associations: A RIA Workshop on Gaia. Proceedings. Granada, Chapt. 2, pp 17–27

Kroupa P., Aarseth S., Hurley J., 2001, Monthly Notices of the Royal Astronomical Society, 321, 699

Krumholz M. R., McKee C. F., Klein R. I., 2005, Nature, 438, 332

Krumholz M. R., Klein R. I., McKee C. F., 2007, The Astrophysical Journal, 656, 959

Krumholz M. R., Klein R. I., McKee C. F., Offner S. S. R., Cunningham A. J., 2009, Science, 323, 754

Lada C. J., 1987, Star forming regions; Proceedings of the Symposium, pp 1–17

Lada C. J., 2006, The Astrophysical Journal, 640, L63

Lada C. J., Lada E. a., 2003, Annual Review of Astronomy and Astrophysics, 41, 57

Lamb J. B., Oey M. S., Werk J. K., Ingleby L. D., 2010, The Astrophysical Journal, 725, 1886

Larson R. B., 1972, Monthly Notices of the Royal Astronomical Society, 156, 437

Larson R. B., 1981, Monthly Notices of the Royal Astronomical Society, 194, 809

Lomax O., Whitworth A. P., Hubber D. A., Stamatellos D., Walch S., 2015, Monthly Notices of the Royal Astronomical Society, 447, 1550

Low C., Lynden-Bell D., 1976, Monthly Notices of the Royal Astronomical Society, 176, 367

Lucy L. B., 1977, The Astronomical Journal, 82, 1013

Lynden-Bell D., 1967, Monthly Notices of the Royal Astronomical Society, 136, 101

Machida M. N., Matsumoto T., Hanawa T., Tomisaka K., 2005, Monthly Notices of the Royal Astronomical Society, 362, 382

Machida M. N., Tomisaka K., Matsumoto T., Inutsuka S., 2008, The Astrophysical Journal, 677, 327

Makino J., 1991, The Astrophysical Journal, 369, 200

Malmberg D., Angeli F. D., Davies M. B., Church R. P., Mackey D., Wilkinson M. I., 2007, Monthly Notices of the Royal Astronomical Society, 378, 1207

Mardones D., Myers P. C., Tafalla M., Wilner D. J., Bachiller R., Garay G., 1997, The Astrophysical Journal, 489, 719

Maschberger T., 2013, Monthly Notices of the Royal Astronomical Society, 429, 1725

Masunaga H., Inutsuka S., 2000a, The Astrophysical Journal, 531, 350

Masunaga H., Inutsuka S., 2000b, The Astrophysical Journal, 531, 350

Moeckel N., Bate M. R., 2010, Monthly Notices of the Royal Astronomical Society, 404, 721

Moeckel N., Clarke C. J., 2011, Monthly Notices of the Royal Astronomical Society, 415, 1179

Monaghan J. J., 1985, Computer Physics Reports, 3, 71

Monaghan J. J., 1992, Annual Review of Astronomy and Astrophysics, 30, 543

Monaghan J. J., 1997, Journal of Computational Physics, 136, 298

Monaghan J. J., 2005, Reports on Progress in Physics, 68, 1703

Monaghan J. J., Lattanzio J. C., 1985, Astronomy & Astrophysics, 149, 135

Motte F., et al., 2010, Astronomy & Astrophysics, 518, L77

Murillo N. M., Lai S.-P., Bruderer S., Harsono D., van Dishoeck E. F., 2013, Astronomy & Astrophysics, 560, A103

Murray N., 2011, The Astrophysical Journal, 729, 133

Myers A. T., McKee C. F., Cunningham A. J., Klein R. I., Krumholz M. R., 2013, The Astrophysical Journal, 766, 97

Nutter D., Ward-Thompson D., 2007, Monthly Notices of the Royal Astronomical Society, 374, 1413

Oelkers R. J., Stassun K. G., Dhital S., 2016, The Astronomical Journal, 153, 259

Oey M. S., Lamb J. B., Kushner C. T., Pellegrini E. W., Graus A. S., 2013, The Astrophysical Journal, 768, 66

Offner S. S. R., Klein R. I., McKee C. F., Krumholz M. R., 2009, Astrophysical Journal, 703, 131

Offner S. S., Kratter K. M., Matzner C. D., Krumholz M. R., Klein R. I., 2010, Astrophysical Journal, 725, 1485

Oh S., Kroupa P., Pflamm-Altenburg J., 2015, The Astrophysical Journal, 805, 92

Padoan P., Nordlund Å., 2002, The Astrophysical Journal, 576, 870

Parker R. J., 2014, Monthly Notices of the Royal Astronomical Society, 445, 4037

Parker R. J., Dale J. E., 2017, Monthly Notices of the Royal Astronomical Society, 470, 390

Parker R. J., Goodwin S. P., 2007, Monthly Notices of the Royal Astronomical Society, 380, 1271

Parker R. J., Goodwin S. P., 2012, Monthly Notices of the Royal Astronomical Society, 424, 272

Parker R. J., Goodwin S. P., Kroupa P., Kouwenhoven M. B. N., 2009, Monthly Notices of the Royal Astronomical Society, 397, 1577

Persson M. V., 2014, SEDs of the different protostellar evolutionary stages, doi:10.6084/m9.figshare.1121574.v2, https://figshare.com/articles/SEDs{_}of{_}the{_}different{_}protostellar{_}evolutionary{_}stages/1121574/2

Plummer H. C., 1911, Monthly Notices of the Royal Astronomical Society, 71, 460

Portegies Zwart S. F., McMillan S. L. W., Hut P., Makino J., 2001, Monthly Notices of the Royal Astronomical Society, 321, 199

Portegies Zwart S. F., McMillan S. L. W., Gieles M., 2010, Annual Review of Astronomy and Astrophysics, 48, 431

Price D. J., Monaghan J. J., 2007, Monthly Notices of the Royal Astronomical Society, 374, 1347

Raghavan D., et al., 2010, Astrophysical Journal, Supplement Series, 190, 1

Rathborne J. M., Jackson J. M., Chambers E. T., Stojimirovic I., Simon R., Shipman R., Frieswijk W., 2010, Astrophysical Journal, 715, 310

Reipurth B., Mikkola S., 2012, Nature, 492, 221

Reipurth B., Zinnecker H., 1993, Astronomy & Astrophysics, 278, 81

Reipurth B., Mikkola S., Connelley M., Valtonen M., 2010, Astrophysical Journal Letters, 725, 56

Reipurth B., Clarke C. J., Boss A. P., Goodwin S. P., Rodriguez L. F., Stassun K. G., Tokovinin A. a., Zinnecker H., 2014, Protostars and Planets VI, pp 267–290

Romano D., Chiappini C., Matteucci F., Tosi M., 2005, Astronomy & Astrophysics, 430, 491

Salpeter E. E., 1955, The Astrophysical Journal, 121, 161

Smith R., Fellhauer M., Goodwin S., Assmann P., 2011, Monthly Notices of the Royal Astronomical Society, 414, 3036

Spitzer L., 1958, The Astrophysical Journal, 127, 17

Spitzer L. S., 1987, Dynamical Evolution of Globular Clusters. Princeton University Press, Princeton

Springel V., 2010, Annual Review of Astronomy and Astrophysics, 48, 391

Springel V., Hernquist L., 2002, Monthly Notices of the Royal Astronomical Society, 333, 649

Sterzik M. F., Durisen R. H., Zinnecker H., 2003, Astronomy and Astrophysics, 411, 91

Tan J. C., Beltrán M. T., Caselli P., Fontani F., Fuente A., Krumholz M. R., McKee C. F., Stolte A., 2014, in Beuther H., Klessen R. S., Dullemond C. P., Henning T., eds, , Protostars and Planets VI. University of Arizona Press, Tucson, pp 149–172

Tobin J. J., et al., 2016, The Astrophysical Journal, 818, 73

Tokovinin A., 2017, Monthly Notices of the Royal Astronomical Society, 468, 3461

Ward J. L., Kruijssen J. M. D., 2018, Monthly Notices of the Royal Astronomical Society, 475, 5659

Ward-Thompson D., Andre P., Crutcher R., Johnstone D., Onishi T., Wilson C., 2007, in Reipurth B., Jewitt D., Keil K., eds, , Protostars and Planets V. University of Arizona Press, Tucson, pp 33–46

Weidner C., Kroupa P., 2004, Monthly Notices of the Royal Astronomical Society, 348, 187

Wilson R. W., Jefferts K. B., Penzias A. A., 1970, The Astrophysical Journal, 161, L43

Wright N. J., Parker R. J., Goodwin S. P., Drake J. J., 2014, Monthly Notices of the Royal Astronomical Society, 438, 639

Wright N. J., Drew J. E., Mohr-Smith M., 2015, Monthly Notices of the Royal Astronomical Society, 449, 741

Wright N. J., Bouy H., Drew J. E., Sarro L. M., Bertin E., Cuillandre J.-C., Barrado D., 2016, Monthly Notices of the Royal Astronomical Society, 460, 2593

Zinnecker H., Yorke H. W., 2007, Annual Review of Astronomy and Astrophysics, 45, 481